CRYSTAL PLASTICITY FINITE ELEMENT METHOD-BASED SIMULATION AND ANALYSIS OF SIZE EFFECTS IN MESO/MICRO-SCALED METAL-FORMING

TONG XU

PhD

The Hong Kong Polytechnic University

2025

The Hong Kong Polytechnic University

Department of Mechanical Engineering

Crystal Plasticity Finite Element Method-Based Simulation and Analysis of Size Effects in Meso/Micro-Scaled Metal-Forming

Tong Xu

A thesis submitted in partial fulfilment of
the requirements for the degree of
Doctor of Philosophy

March 2025

CERTIFICATE OF ORIGINALITY

I hereby declare that this thesis is my own work and that, to the best of my knowledge and belief, it reproduces no material previously published or written, nor material that has been accepted for the award of any other degree or diploma, except where due acknowledgment has been made in the text.

TONG Xu

Abstract

The manufacturing sector is experiencing a significant trend towards product miniaturization, particularly within industries such as automobile, medical instruments, and consumer electronics. To fulfil this demand, meso/microforming has emerged as a promising method for producing miniaturized parts and components. However, challenges related to product quality assurance and process control persist, largely due to the size effect (SE) that influences deformation mechanisms and behaviours in meso/microforming. In tandem with this, This PhD thesis is focused on studying the SE and its induced forming phenomena in micro/meso-scaled metal-forming of complex-shaped parts by Crystal Plasticity Finite Element Method (CPFEM) based simulations.

The study begins by validating the feasibility of CPFEM for simulating simple meso/microforming processes through the comparisons with experimental data. This ensures the accuracy of CPFEM simulation accuracy in predicting deformation behavior, load-stroke relationships, and microstructural changes. Subsequently, the application of CPFEM is extended to more complex forming processes, such as progressive microforming and multi-step forming operations. The research revealed that CPFEM's capability to predict deformation and failure mechanisms in these forming processes, addresses a significant gap in current knowledge.

Secondly, a comparative analysis of CPFEM with other common simulation methods is done in terms of the evaluation of their respective strengths and weaknesses, in terms of prediction accuracy, computational efficiency, and microstructural evolution. The integration of CPFEM with advanced experimental

techniques, such as the quasi-in-situ Electron Backscatter Diffraction (EBSD), provides a comprehensive approach to understanding deformation mechanisms and microstructural changes influenced by grain SEs.

The findings demonstrate CPFEM's effectiveness in capturing detailed material behaviours and deformation mechanisms. This work not only establishes a basis that CPFEM is a superior simulation tool to offer actionable insights for optimizing forming processes and selecting appropriate materials. Future research directions include enhancing computational efficiency, integrating multi-physics models, advancing fracture modelling, developing material databases, optimizing processes, and implementing in-situ and real-time monitoring.

In summary, this thesis significantly advances the application of CPFEM in meso/microforming processes. Through meticulous simulations, experiments, and result comparisons, it demonstrated the CPFEM's unparalleled ability to capture detailed material behaviours and deformation mechanisms influenced by SEs. The insights gained hold substantial promise for enhancing the accuracy, efficiency, and reliability of forming complex-shaped components at the meso/micro-scale, facilitating the way for future innovations in micro-manufacturing.

Publications arising from this research

International journal papers

[1] **Tong, X.**, Zheng, J. Y., Fu M. W. (2022). Numerical and experimental study of the size effect on deformation behaviour and quality of microembossed multi-channel structures. ***Journal of Manufacturing Processes,*** 78, 363-375.

[2] **Tong, X.**, Li, Y., Fu, M. W. (2024). Modelling of grain size effects in progressive microforming using CPFEM. ***International Journal of Mechanical Sciences***, 267, 108971.

[3] **Tong, X.**, Wang, Y. B., Li, Y., Fu M. W. (2025). Grain size effect analysis of progressive meso-scaled forming aided by Coupled Eulerian-Lagrangian approach and CPFEM. ***Journal of Manufacturing Processes***, under review.

[4] **Tong, X.**, Cai, W., Fu M. W. (2025). Microstructure evolution and deformation mechanisms in micro-extrusion: an integrated quasi-in-situ EBSD and CPFEM study. ***To be submitted***.

Conference papers

[5] **Tong, X.**, Fu M. W. Numerical Study of Grain Size Affected Deformation Behaviour in Two-Stage Micro Deep Drawing Using CPFEM, ***2022 World Congress on Micro and Nano Manufacturing***, 19-22 September, 2022, Leuven, Belgium.

[6] **Tong, X.**, Li, Y., Fu, M. W. Study on the Micro-Scale Deformation Behaviour of Al-B4C Composite by Using CPFE-CZ Model. ***The 14th International Conference on the Technology of Plasticity - Current Trends in the Technology of Plasticity***. September 24-29, 2023, Mandelieu-La Napoule, France.

[7] **Tong, X.**, Fu M. W., Crystal plasticity finite element method application in meso/micro-scaled deep drawing and some related concerns, ***The 44th Conference of the International Deep Drawing Research Group***. June 1-5, 2025, Lisbon, Portugal.

Acknowledgements

In October 2019, after a five-year hiatus from university life and at the age of 27, I stepped onto the campus of the Hong Kong Polytechnic University. For someone of my age, Professor Fu Mingwang accepted me, allowing me to pursue a research dream that had long been cherished by me, this “old boy”. Over the following six years, with Professor Fu’s guidance, I was able to conduct my master’s and doctoral research within an excellent team and on an advanced and inclusive university platform. Professor Fu’s support has been the re-launching of my career and the greatest help in my life. I will forever be grateful for Professor Fu and the Hong Kong Polytechnic University for the opportunities and experiences they have provided, and I will always cherish and reciprocate them.

A warm and harmonious research group has been the essential support for me to maintain my passion and original aspiration in research. I would like to extend my special thanks to Dr. Zheng Junyuan, who guided me in getting familiar with the team and learning how to conduct research. I am also grateful for the selfless help from Dr. Fu Jin, Dr. Fang Jieyichen, Dr. Huang Jihui, Dr. Wang Yubao, Prof. Shen Qingliang, Dr. Cai Wang, Prof. Yang Heng, Dr. Wang Jianying, Dr. Zhang Rui, Dr. Sun Xinxin, Mr. Hu Dien, Mr. Feng Zhenyong, Mr. Yu Zhenyu, Mr. Wong Boching Leslie, Mr. Huang Zihan, and Mr. Zhang Huaqing. Additionally, I appreciate the assistance from Dr. Wang Jilai, Dr. Ran Jiaqi, Dr. Li Wenting, Dr. Tang Xuefeng, Dr. Tian Wenlong, and Prof. Ma Jun, who continued to help me even after their graduation.

Lastly, I am grateful for the selfless dedication and love of my parents, Mr. Tong Guofeng and Madam Shi Linai, during my time as an older graduate student. I also thank my wife, Zhou Xuyan, who supported me throughout the long periods of

separation during the pandemic and has been the driving force behind the completion of this doctoral project.

Finally, I would like to conclude my six-year journey at the PolyU with a new written Chinese poem.

久别黉序返学林，理工焕彩梦初临。

恩师引路情如海，同窗携手续锦文。

科研途远多风雨，家暖如春志愈忱。

岁月悠长心自定，感恩一路伴君吟。

Table of Contents

List of abbreviations and acronyms

Abbreviations	Explanations
SE	Size effect
CPFEM	Crystal plasticity finite elements method
FEM	finite elements method
RVE	Representative volume elements
EBSD	Electron Backscatter Diffraction
FEA	Finite element analysis
HCP	Hexagonal close-packed
MDD	Micro deep drawing
CZM	Cohesive zone model
FG	Fine grain
MG	Medium grain
CG	Coarse grain
MAXS	Maximum nominal stress criterion
MODF	Misorientation distribution function
ODF	Orientation distribution function
LAGB	Low-angle grain boundary
PF	Pole Figure
CEL	Coupled Eulerian-Lagrangian method
UMAT	User-defined material subroutine
DMZ	Dead metal zone

Chapter 1 Introduction

1.1 Research background

The escalating prevalence of product miniaturisation is a notable trend across various industrial sectors, including micro lector mechanical systems, automobiles, and medical instruments [1-3]. In response to this trend, the efficient production of miniaturized components has emerged as a critical challenge. Meso/microforming, which entails the fabrication of parts and components at the meso/micro scale, has garnered significant attention due to its numerous advantages. These include low manufacturing costs, high productivity, efficient material utilization, and the enhanced mechanical properties of the resultant meso/microformed parts [4, 5]. However, despite these benefits, the assurance of product quality and the control of the meso/microforming remain problematic when dealing with metallic or metal-based materials. These issues are particularly pronounced in the production of complex and highly accurate meso/micro-scaled components and structures, where undesirable geometries, loss of dimensional accuracy, and tolerance deviations frequently occur [6-10]. This is largely attributable to the SEs, a phenomenon that arises due to the altered deformation mechanisms and mechanical responses during the downscaling process, thereby significantly impacting the overall forming behaviour [11, 12].

When sheet metal undergoes conventional heat treatment, the grain size typically approximates the thickness of the sheet, thereby exacerbating anisotropy during deformation [13-15]. This can impact the dimensional accuracy, surface finish, and load-bearing capacity of the formed metal components [16, 17]. Research by Fu et al.

has examined the SEs in progressive forming of various meso/micro-scaled axisymmetric components, including hollow flanged parts [18, 19], double-flanged parts [20], conical-flanged parts [21], and pogo pins [22]. These studies were conducted using metal sheets—copper, brass, and titanium—of 0.5-2.0 mm in thickness and with grain sizes ranging from 20 to 200 μm. The consensus reached indicates that the forming load for coarse-grained materials is lower, while the dimensional accuracy for fine-grained materials is enhanced. Contrary to these findings, the grain SE on the extrudate length is, however, opposite for the pogo-pin [22] and another hollow flanged micropart [23]. Additionally, other studies have been conducted by Ghassemali et al. [24] and Zhang et al. [25], employing two-step forming and progressive forming processes to manufacture micro-pins and bipolar plates, respectively. Many of these studies have relied on conventional FEM simulation, as it can significantly reduce the costs associated with process and tooling design and development. However, the SEs have not been well represented in the simulations conducted in the aforementioned studies, because the FEM is primarily developed for handling macro-scale scenarios.

In response to this challenge, several studies have explored innovative approaches, including the CPFEM. CPFEM is inherently well-suited for predicting grain SEs during meso/micro-scaled forming processes, as it takes into account crystal orientations, grain boundaries, and other microstructural features at the grain level that are directly related to the anisotropy and heterogeneity of material behaviour [26-28]. CPFEM has been extensively utilized to simulate the forming process. Guo et al. [29] employed CPFEM for the simulation of TWIP steel deep drawing characterized by a high ratio of sheet thickness to drawing depth. Kardan-Halvaei et al. [30] and Zheng et al. [31] subsequently applied the method to simulate the upsetting of similar flange parts, respectively. Tong et al. [32, 33] initially conducted 2D CPFEM simulations of

microembossing using a pure copper sheet and subsequently performed 3D simulations for the progressive forming of a hexagonal socket part by integrating CPFEM with the cohesive zone model. They observed that while CPFEM offers essential insights into the coupled behaviour of SEs and microscale deformation mechanisms, its computational expense may be excessively high, rendering it computationally infeasible, particularly for large deformation processes such as meso/microforming processes.

To summarize, the application of CPFEM in the meso/micro-scale has primarily been confined to Representative Volume Elements (RVE) and "simple" forming processes, and most of size effects cannot be captured by FEM, which greatly influence the product quality and process control. Given this gap, it is essential to conduct relevant research. Therefore, the focus of this thesis is on the application and expansion of CPFEM in the forming of meso/micro-scaled components.

1.2 Research objectives

This PhD thesis is driven by the need to expand the application of the CPFEM in the forming processes of meso/micro-scaled components. The research flowchart for this thesis is shown in Fig. 1.1. The detailed objectives are as follows:

1) To develop an integrated meso/micro-scaled progressive forming system combining product design, process analysis, and CPFEM simulation, and utilize it to investigate the interplay between scale-dependent deformation behavior, size effect mechanisms, and final part quality (e.g., dimensional accuracy, surface integrity, mechanical properties) across diverse product geometries.
2) To establish an engineering-feasible CPFEM framework for predicting material deformation in meso/micro-scaled forming, explicitly incorporating the effects of

grain-scale heterogeneity and texture evolution. This framework will be validated against experimental data for fundamental processes to quantify its accuracy in capturing critical engineering metrics.

3) To deploy the developed CPFEM framework for simulating complex progressive forming operations, assessing its predictive capability for deformation mechanics, failure initiation, and final part quality under strong size effects. Comparative analysis with conventional FEM methods will quantify gains in accuracy and computational practicality for engineering applications. To provide microstructure-informed guidelines for process optimization.
4) To elucidate the fundamental mechanisms linking microstructure, size effects, and deformation by integrating CPFEM predictions with high-resolution EBSD characterization across deformation zones. This will quantify the influence of initial grain structure (size, orientation) and deformation-induced heterogeneity on meso/micro forming behavior and final part performance.

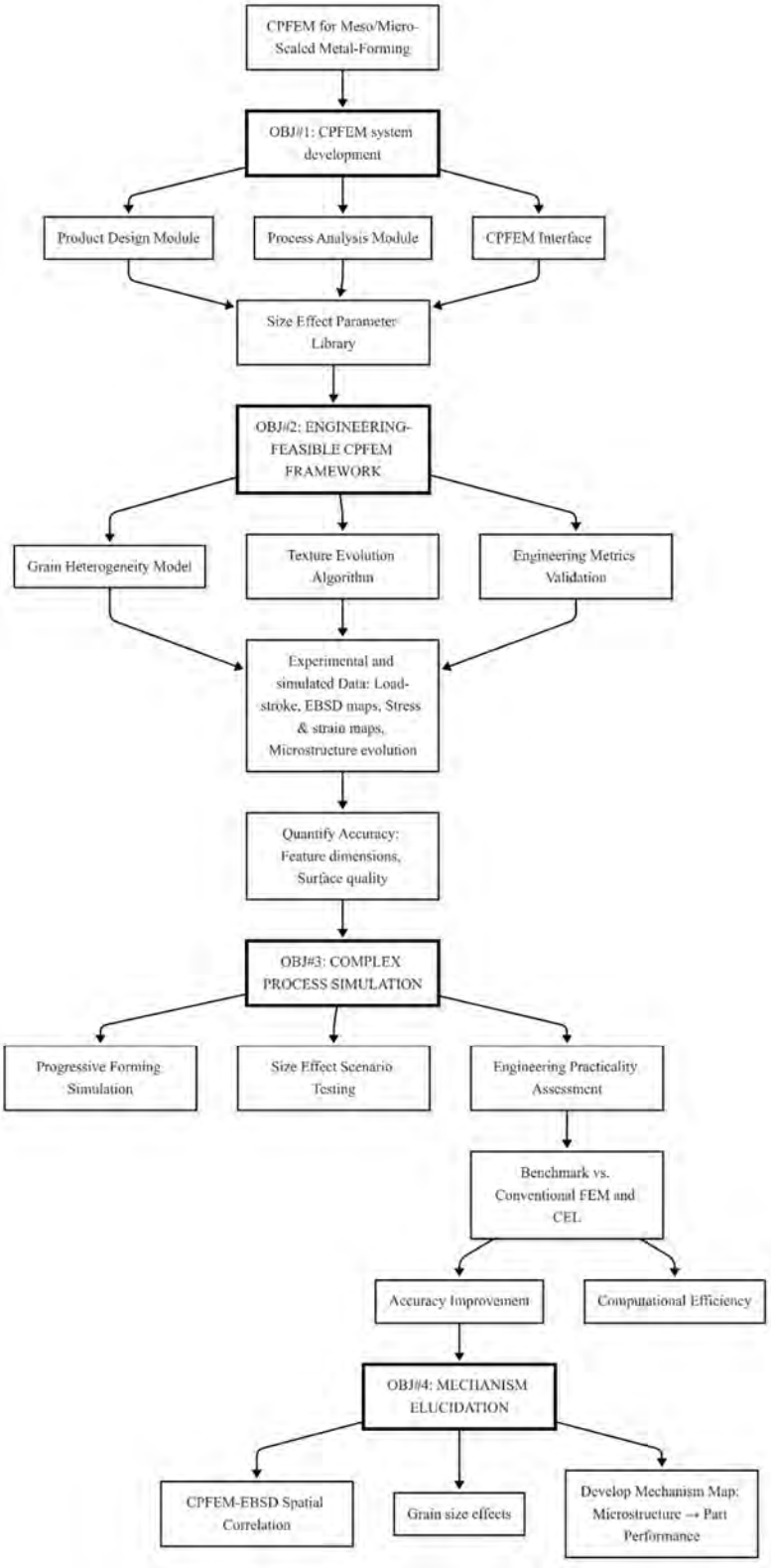

Fig. 1.1 Research flowchart for this thesis.

1.3 Significance of this thesis

In the short term, this thesis provides a comprehensive and detailed exploration of the application of CPFEM in the meso/microforming. By validating the feasibility of CPFEM through simulations and experimental comparisons, this research offers immediate practical benefits for industries involved in micro and meso manufacturing. Specifically, the insights gained from this study can be directly applied to optimize existing forming processes, leading to improved part quality, reduced production costs, and enhanced process reliability. The detailed analysis of CPFEM's capabilities in capturing material behaviour and deformation mechanisms also serves as a valuable reference for engineers and researchers looking to adopt advanced simulation techniques in their work. Furthermore, the comparative study with other methods provides actionable recommendations for selecting the most appropriate simulation approach based on specific process requirements, thereby facilitating more efficient and accurate process design.

From a long-term perspective, this thesis represents a significant step forward in advancing the theoretical and practical understanding of CPFEM in meso/microforming processes. By addressing the limitations of current research and expanding the application of CPFEM to more complex parts, this work lays the foundation for future innovations in manufacturing technologies. The detailed investigation of deformation mechanisms and microstructural evolution provides a deeper understanding of material behaviour at small scales, which is crucial for the development of new materials and advanced forming processes. Additionally, the integration of CPFEM with experimental techniques, such as EBSD, opens up new avenues for real-time monitoring and optimization of forming processes. These advancements have the potential to transform the way complex parts are designed and

manufactured, leading to more efficient, sustainable, and high-performance manufacturing solutions. Ultimately, this research contributes to the broader goal of enhancing the precision and reliability of meso/microforming processes, paving the way for the next generation of advanced manufacturing technologies.

1.4 Outline of the thesis

This thesis consists of seven chapters. Chapter 1 identifies the research gaps, presents the research objectives, and elaborates on the significance of this doctoral project. Chapter 2 provides a systematic literature review and critical analysis. Chapters 3, 4, 5, and 6 introduce the main research discussions and findings. Chapter 7 concludes the thesis with overall conclusions and suggestions for future research directions.

Chapter 2 Literature Review

2.1 Meso/microforming

Meso/microforming is an advanced manufacturing technology that focuses on the production of components within specific size ranges. As shown in Fig. 2.1, it is designed to create parts with dimensions typically ranging from a few micrometres (μm) to several millimetres (mm), bridging the gap between macro-scale and nano-scale manufacturing.

Fig. 2.1 Meso/micro-scaled components and structures fabricated by forming processes [3, 34-36].

At the micro-scale, forming processes are employed to produce small, intricate components with high precision and accuracy. These components are often used in applications requiring miniaturization, such as microelectronics and medical devices

[37, 38]. Meso-scaled forming, on the other hand, involves slightly larger dimensions and is used to create components that are still relatively small but require more robust mechanical properties. This scale is particularly relevant for industries like automotive and aerospace, where lightweight yet strong components are needed [39, 40]. Overall, meso/microforming leverages specialized techniques to achieve the desired process control and product quality within these specific size ranges.

Meso/microforming can be classified into several categories, including sheet metal-forming, bulk metal-forming, and hybrid forming processes. Each category has its unique characteristics and applications. The examples of these forming processes are illustrated in Fig. 2.2.

1) Sheet metal-forming

Sheet metal-forming is a versatile category of meso/microforming that involve the deformation of thin metal sheets into desired shapes [41]. This technique is widely applied for producing meso/micro-scaled components with high precision and complex geometries. The main subcategories of sheet metal-forming include:

i. Meso/micro-stamping and embossing are precision forming processes used to produce small-scale structures or parts directly from sheet foil [10]. It involves placing the metal sheet between punches and dies and applying high load to shape the material, as shown in Fig. 2.2 (a). The difference is that these processes involve blind stamping to create depth or height. Stamping creates a recessed effect, while embossing creates a raised effect [42]. These processes are highly efficient for mass production and can achieve high dimensional accuracy. It is commonly used in the manufacturing of microelectronic components, such as connectors and micro-sensors [43].

ii. Meso/micro-bending is a forming process that bends thin metal sheets into specific angles or shapes [44]. It is typically performed using specialized bending tools or fixtures, as shown in Fig. 2.2 (e). The process is highly precise and can produce complex geometries with tight tolerances. This process is widely used in the production of meso/micro-scaled components for medical devices and precision instruments [45, 46].

iii. Meso/micro-deep drawing is a process where a flat metal sheet is drawn into a die to form a cup-shaped or hollow part [47]. The sheet is subjected to tensile forces, causing it to stretch and take the shape of the die, as shown in Fig. 2.2 (b). This process is known for its ability to produce deep, intricate shapes with high precision. It is commonly used in the manufacturing of meso/micro-scale containers and housings for electronic components [48].

iv. Meso/micro-blanking is a process used to cut and separate small parts from a larger sheet of metal [49]. It involves using a punch and die to shear the material along a specific path, as shown in Fig. 2.2 (d). The process is highly precise and can produce parts with clean edges and minimal burrs. This process is widely used in the production of meso/micro-scaled components for aerospace and automotive applications [50].

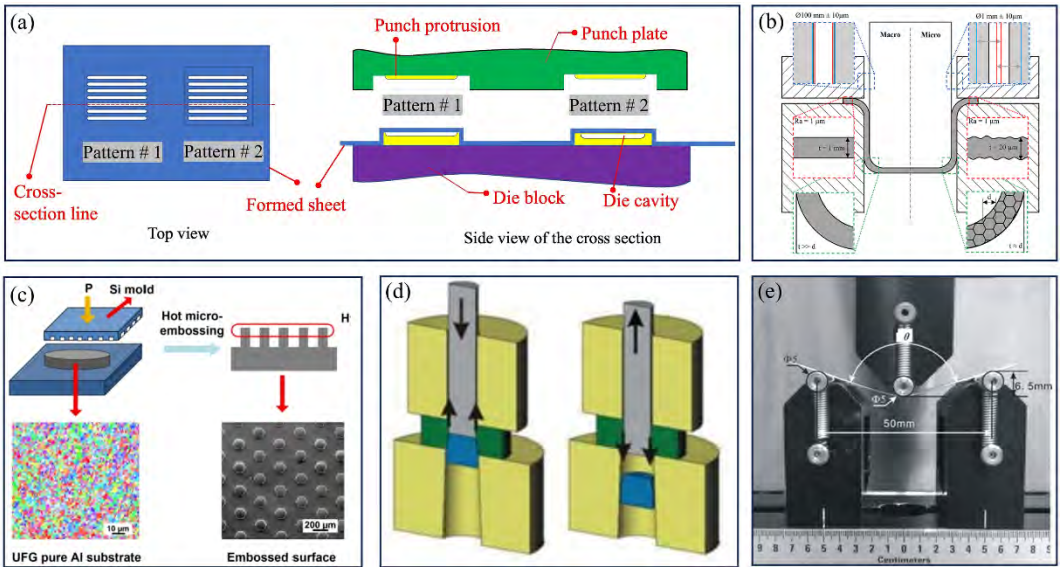

Fig. 2.2 Common meso/micro-scaled sheet metal-forming: (a) meso/micro-stamping [51], (b) meso/micro-deep drawing [52], (c) meso/micro-embossing [53], (d) meso/micro-blanking/heading [54], and (e) meso/micro-bending [6].

2) Bulk metal- forming

Bulk metal-forming is essential techniques in meso/micro-scaled manufacturing and utilized to make bulk metal materials into desired forms [55]. It involves significant deformation of the workpiece, resulting in components with high strength and dimensional accuracy. The representatives of meso/micro-scaled bulk forming processes are shown in Fig. 2.3. The main subcategories of bulk metal-forming include:

i. Meso/micro-forging uses localized compressive forces to shape metal, which is performed with a hammer (usually a powered hammer) or a die [56]. The dies are designed to control the flow of material, resulting in components with complex geometries and high dimensional accuracy. This process is often used for producing small-scaled components with intricate shapes, such as micro-turbine blades [57].
ii. Meso/micro-extrusion is a process where metal is forced through a die to produce long, continuous shapes [58]. In meso/micro-scale extrusion, the process is scaled

down to produce small-diameter or thin-walled components. Direct extrusion is ideal for manufacturing small-diameter rods, tubes, and wires. Indirect extrusion reduces friction and wear on the die, making it suitable for producing high-precision micro-scaled components such as micro-tubes and micro-channels.

iii. Meso/micro-rolling is a process where metal is passed through a pair of rolls to reduce its thickness and improve its surface finish [59]. Flat rolling is used to produce thin metal sheets for applications such as microelectronics and medical devices. Profile rolling is used to manufacture small-scaled components with complex profiles, such as micro-gears and micro-springs.

iv. Meso/micro-upsetting is a bulk-forming process where the metal is compressed to increase its cross-sectional area in one direction while reducing it in another. It is utilized to produce small-scaled components such as micro-bolts, micro-pins, micro-rollers and micro-bearings [60].

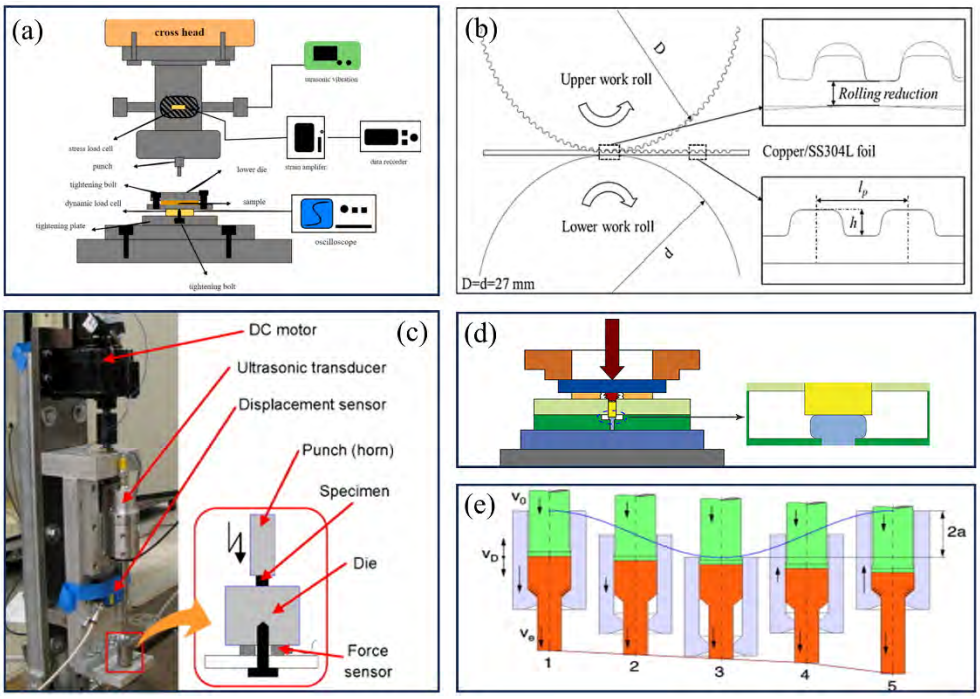

Fig. 2.3 Common meso/micro-scaled bulk metal-forming: (a) meso/micro-forging [61], (b) meso/micro-rolling [62], (c) meso/micro-heading [63], (d) meso/micro-

upsetting [64], and (e) meso/micro-extrusion [65].

3) Hybrid Forming Processes

Hybrid forming processes are innovative manufacturing techniques that integrate multiple forming methods to leverage their combined advantages. These processes are particularly useful in meso/microforming, where the production of complex geometries and high-precision components is required. The main utilization of hybrid forming in meso/micro-scale can be seen in Fig. 2.4. The following sections introduce some key hybrid forming processes.

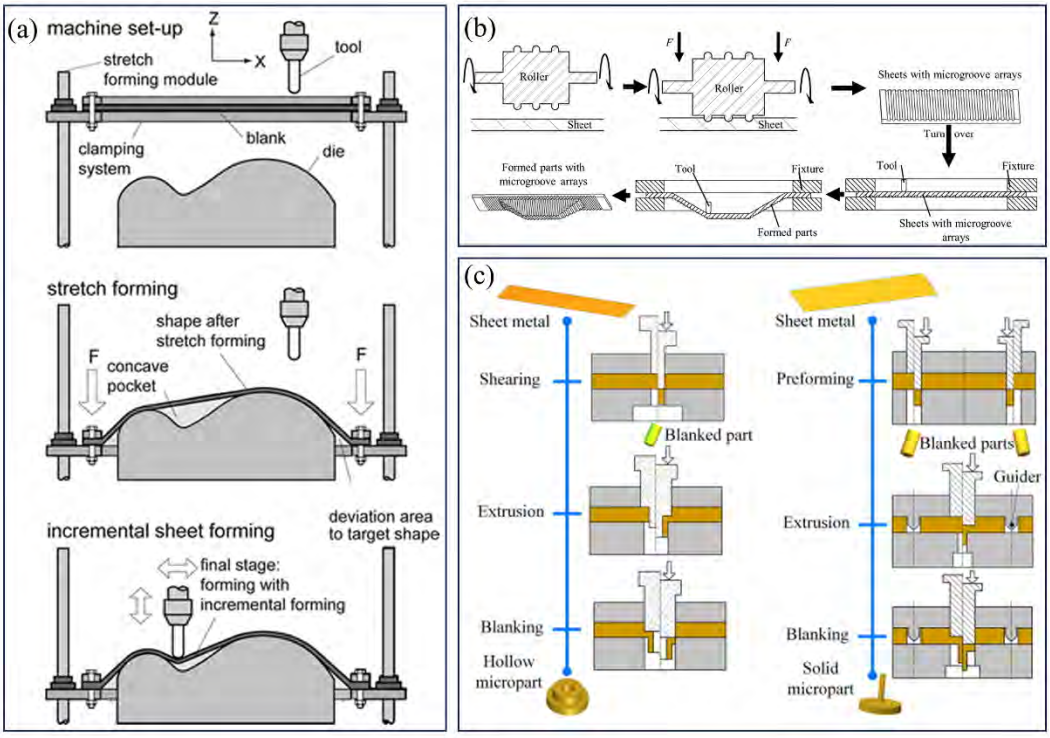

Fig. 2.4 Common meso/micro-scaled hybrid forming processes: (a) multi-point incremental forming and stretch forming [66], (b) micro-rolling & incremental sheet forming [67], and (c) progressive forming [68].

i. Hybrid incremental forming processes combine traditional incremental forming

techniques with other manufacturing methods to enhance formability and surface quality [69]. For example, incremental sheet forming combined with stretch forming integrates single-point incremental forming with stretch forming to produce complex geometries with improved surface quality and reduced springback. Multi-point incremental forming uses multiple forming points to distribute the deformation more evenly, resulting in better thickness distribution and reduced thinning.

ii. Progressive forming is a specialized hybrid process that involves continuous deformation of a workpiece through multiple forming stations [70]. In progressive forming, a metal sheet is fed through a series of dies, each performing a specific forming operation. The strip is advanced precisely between stations to ensure accurate alignment. This method is ideal for producing high-precision parts with complex geometries, such as microelectronics components and automotive parts.

To summarise, meso/microforming processes encompass a broad spectrum of techniques and applications, exhibiting considerable diversity and adaptability. Each category is distinguished by its unique attributes and associated challenges. A thorough comprehension of these distinctions is essential for the judicious selection of the most suitable forming process tailored to specific application requirements.

2.2 Size effects in meso/microforming

2.2.1 Concept of size effects

SEs play a crucial role in meso/microforming processes, significantly influencing material behaviour and the overall forming characteristics [71]. Unlike macro-scaled forming, where material properties are generally considered uniform and size-independent, meso/microforming involves dimensions that are comparable to the

material’s microstructural features. This leads to unique phenomena that must be understood and accounted for the design and optimization stages.

SEs refer to the changes in material properties and deformation behaviour that occur as the characteristic dimensions of the workpiece approach the size of the grains. These effects are categorized into two main types: feature SE and grain SE [72].

1) Feature SE: It arises when the workpiece dimensions are comparable to the microstructure size of the material. At these scales, the material behaviour deviates from classical continuum mechanics assumptions. For example, surface-to-volume ratios increase significantly at meso/micro-scales, leading to enhanced surface energy effects. This can result in phenomena such as increased strength, reduced ductility, and altered deformation mechanisms [73].
2) Grain SE: In meso/microforming, the grain size of the material can have a significant effect on the forming behaviour. Smaller grain sizes typically result in elevated stress and hardness levels. This phenomenon occurs because the higher number of grain boundaries serves as obstacles to dislocation movement, thereby enhancing the material's resistance to deformation [74]. However, smaller grains can also result in reduced ductility, making the material more susceptible to fracture during forming. Therefore, the grain size must be carefully controlled to balance strength and formability in meso/microforming processes.

2.2.2 Size effects on mechanical properties and material fracture

At the meso/micro-scale, the hardening behaviours of materials is significantly influenced by SEs, which arise due to the interaction between the characteristic dimensions of the workpiece and the material’s microstructural features. These effects

are particularly pronounced when the dimensions of the workpiece approach the scale of the material's microstructure. Understanding these SEs is crucial for predicting and controlling forming behaviours.

In the realm of meso/microforming, the dimensions of the workpiece, such as thickness or diameter, exert a substantial influence on the flow stress characteristics. As these dimensions are reduced, the material's response diverges from the conventional macro-scale behaviour. For instance, Fig. 2.5 illustrates a notable trend where the tensile stress of AA1070 is decreasing with sheet thickness across. Unlike interior grains, which are encased by neighbouring grains and thus experience higher resistance to deformation, surface grains encounter relatively less constraint. This disparity in deformation resistance results in a reduction in the overall stress. For example, micro-scale tensile testing has revealed that the stress of thin sheets diminishes as the ratio of thickness to grain size (t/d) drops below a critical threshold [75]. This phenomenon is indicative of the heightened influence of surface grains, which increasingly dictate the material's deformation behaviour at smaller scales.

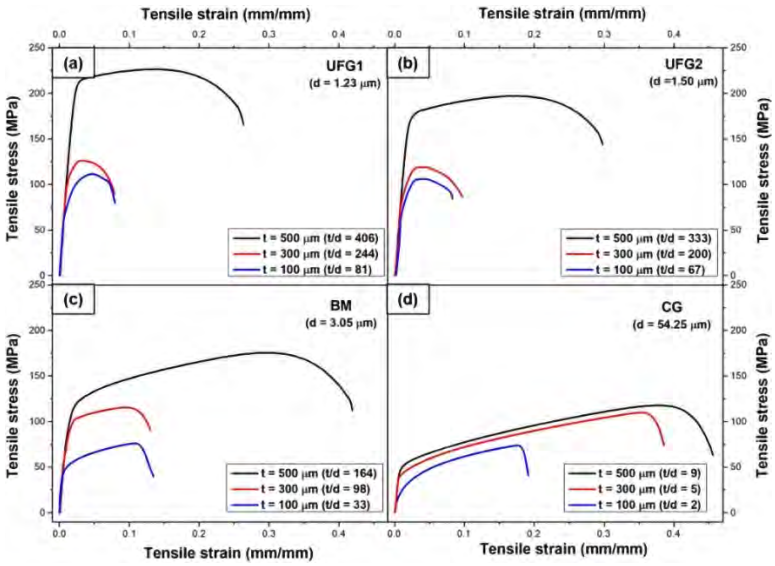

Fig. 2.5 Tensile stress strain curves for different sample thicknesses of AA1070,

showing feature SEs [76].

When materials possess identical thickness or diameter, the increasing grain size results in a greater proportion of surface grains, which are subject to reduced deformation resistance. This phenomenon consequently causes the stress to diverge from the classical Hall-Petch relationship. Fig. 2.6 illustrates the grain SEs on the yield and stress of various materials.

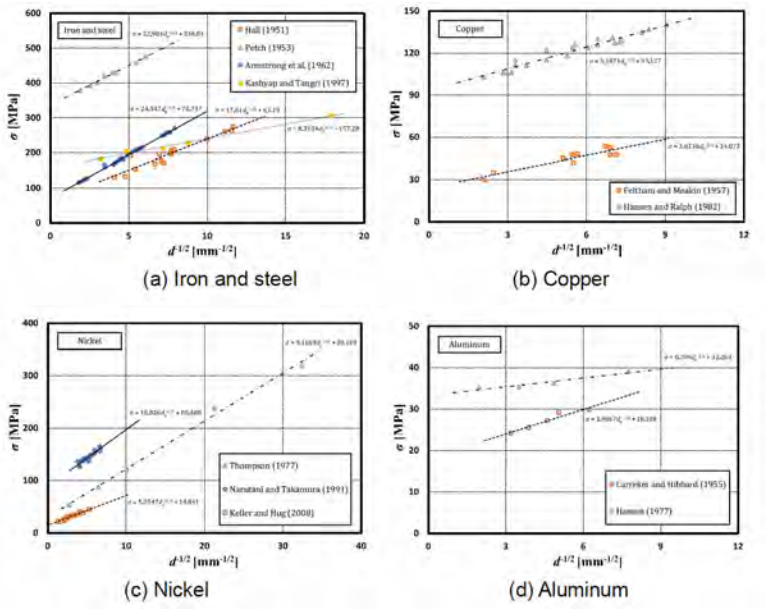

Fig. 2.6 Grain SEs in yield and stress of various materials [77].

Moreover, in meso/microforming processes, the fracture and damage behaviours of metallic materials under stress are strongly influenced by SEs. As shown in Fig. 2.7, the SEs on the fracture strain are very significant. These effects are distinct from those observed at macro-scales and are primarily driven by the interplay between the dimensions of the workpiece and the material's microstructure [78]. On the one hand, at meso/micro-scales, damage accumulation in metals is influenced by the increased surface grains ratio. Surface grains are more susceptible to deformation and damage due to their reduced resistance to deformation compared to the interior ones. This

results in a higher rate of damage accumulation, which can strongly influence the material's overall mechanical properties [79]. On the other hand, the increase of grain size can lead to significant microstructural heterogeneity. This heterogeneity can cause localized damage accumulation, especially in regions with fewer grains. Crack propagation in metals at meso/micro-scales is also affected by SEs [80]. Finer grains typically exhibit greater resistance to crack propagation, as the higher density of grain boundaries serves to impede crack growth. However, at meso/micro-scales, the reduced number of grains per unit volume can lead to more significant variations in crack propagation behaviour. For example, in micro-scale tensile tests, cracks are more likely to propagate along grain boundaries.

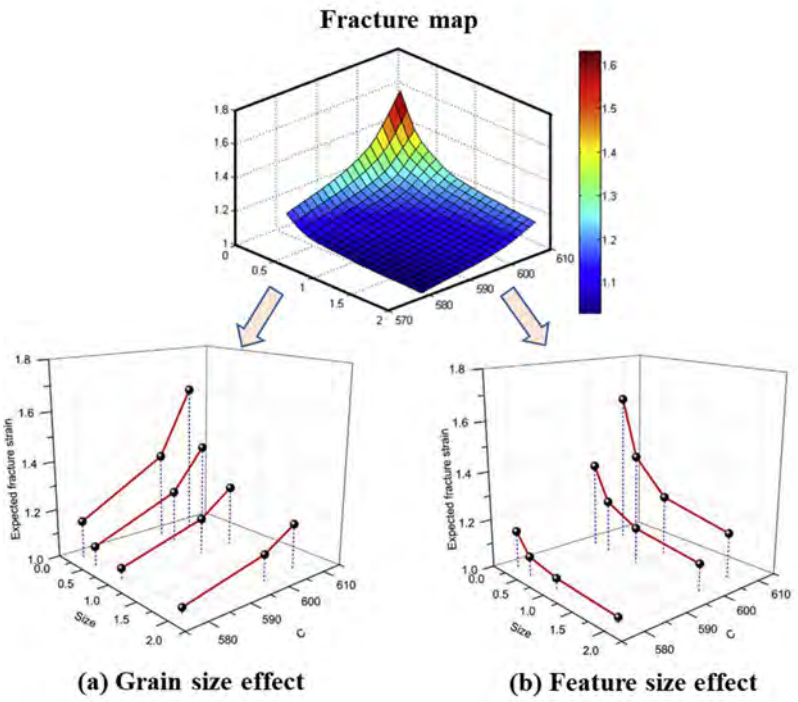

Fig. 2.7 Size effects in fracture strain of brass material [81].

2.2.4 Size effects on deformation behaviours in meso/microforming

In meso/microforming processes, SEs significantly influence the deformation

behaviours of materials, including load-stroke relations, dimensional precision, material flow, surface roughness, etc. As shown in Fig. 2.8, two cases (a pogo-pin and a connector) were selected to describe the grain SEs on the product quality issues in meso/microforming.

In the process control of forming technologies, the control of the load-stroke relations is highly critical. The load-stroke curve serves as a crucial diagnostic tool, offering comprehensive insights into the material's deformation characteristics throughout the forming process. By analysing this curve, it is possible to precisely monitor and obtain the process parameters. As shown in Fig. 2.8 (a), when the same set of dies and processing conditions are used to form materials with different grain sizes, distinct load variations are observed. As grain size diminishes, the load necessary to induce deformation correspondingly rises. Additionally, the disparity in load becomes particularly notable during the final blanking stage. During blanking, the material experiences abrupt and localized deformation, and the smaller grain size significantly amplifies the material's resistance to deformation. Consequently, the load required for blanking escalates markedly with decreasing grain size. Comprehending and managing these load variations are vital for refining the process and ensuring the reliability and quality of the formed components.

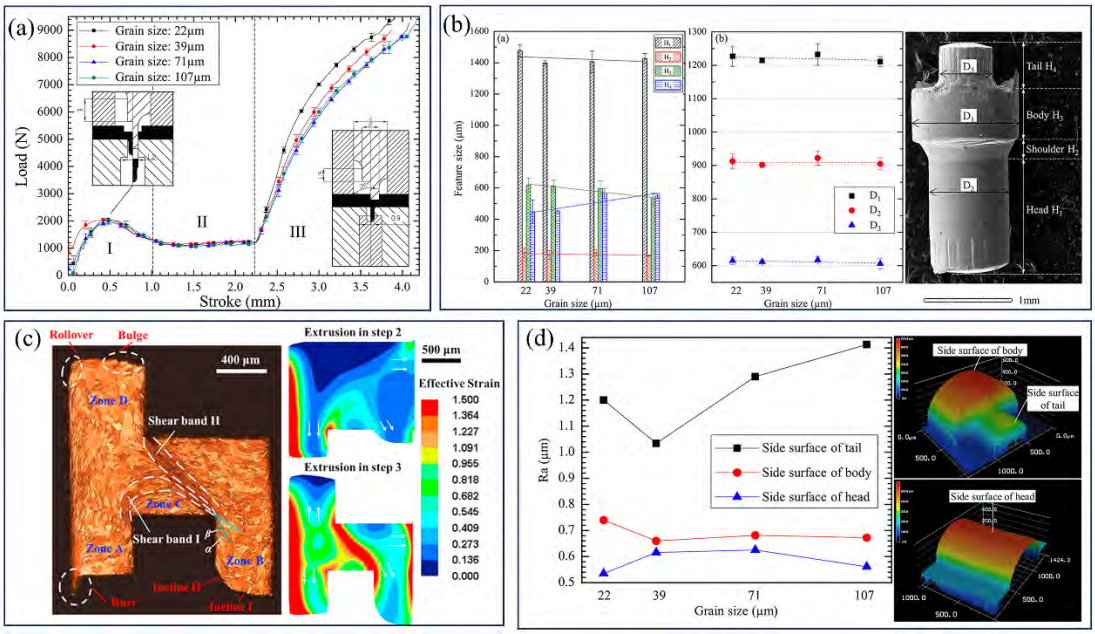

Fig. 2.8 The grain size effects on (a) load-stroke relations, (b) dimensional accuracy, (c) material flow behaviours, and (d) surface roughness [22, 23].

The quality of the final formed components is always a matter of great concern. For meso/micro-scaled parts, grain size becomes particularly sensitive to the dimensional accuracy of the components. As shown in Fig. 2.8 (b), there are SEs in the length and diameter of different sections of a pogo-pin. To analyse this behaviour, one can observe the material flow to predict the final dimensions. Fig. 2.8 (c) illustrates the microstructure and simulated strain accumulation in a cross-section of another connector part. It is evident that grains in different regions experience varying degrees of deformation, characterized by grain deformation and rotation. High-strain areas often exhibit smaller grain sizes and more pronounced deformation, resulting in the shear bands. Moreover, for most meso/micro-scaled parts, surface quality is crucial for their application. Surface roughness and defects can significantly affect the performance and reliability of these small-scaled components. For example, Fig. 2.8 (d) shows the quality of two mating surfaces of a pogo-pin. The grain SEs on surface

quality is apparent, and whether additional post-processing is required remains a topic for further investigation.

SEs are of paramount importance in mese/microforming processes. They significantly influence the dimensional precision, material behaviour, and surface quality of the components. To achieve high-quality and high-precision parts, it is essential to have appropriate tools and techniques to control and optimize the forming processes. Understanding and managing these size effects are crucial for ensuring the reliability and performance of micro/meso-scaled components.

2.3 Crystal plasticity finite element method

2.3.1 Basics of crystal plasticity finite element method

Most metallic materials are composed of crystalline structures, where atoms are arranged in a periodic lattice. This inherent crystalline nature gives rise to anisotropy, meaning that the material properties can vary depending on the direction within the crystal lattice [82]. Crystal anisotropy is a fundamental characteristic of metallic materials and significantly influences their mechanical behaviour. For example, the deformation mechanisms, such as slip and twinning, are highly dependent on the crystallographic orientation [83]. This anisotropy affects the material's response to applied stresses, leading to differences in strength, ductility, and deformation patterns along different crystallographic directions [84]. Accurate prediction of the metallic materials, particularly in complex forming processes, hinges critically on the recognition and incorporation of material anisotropy.

Finite element analysis (FEA) has long been a powerful tool for simulating the mechanical behaviour of materials. However, traditional FEA often assumes isotropic

material behaviour, which is insufficient for accurately capturing the anisotropic nature of crystalline materials. To address this limitation, crystal plasticity models were integrated into finite element frameworks. This integration allows for the explicit consideration of crystallographic orientation and deformation mechanisms within the finite element analysis. By incorporating crystal plasticity, the FEA can more accurately simulate the deformation behaviour of metallic materials, taking into account the anisotropic effects that arise from the underlying crystal structure.

Current phenomenological crystal plasticity mainly considers the slip and twinning mechanism in crystalline materials. As shown in Fig. 2.9 (a), slip is a fundamental deformation mechanism in crystalline materials, particularly in metals. It involves the movement of dislocations along specific crystallographic planes and directions. Twinning is another deformation mechanism that occurs in crystalline materials, particularly in metals with low-symmetry crystal structures, such as hexagonal close-packed (HCP) metals like magnesium. Twinning involves the formation of a mirror image of the crystal lattice across a specific plane, known as the twin plane. Moreover, the relative orientation between the slip plane, slip direction, and applied force can be seen in Fig. 2.9 (b). In such a way, a slip plane and a slip direction constitute a slip system, where the critical resolved shear stress τ_R is required to describe the slip system, as shown in the following:

$$\tau_R(\varepsilon) = cos\theta cos\varphi \cdot \sigma = f \cdot \sigma \tag{2.1}$$

where f is the Schmid factor related to the grain orientation. The Schmid factor is used to predict the likelihood of a particular deformation mechanism being activated. A higher Schmid factor indicates a greater likelihood of that mechanism being activated under a given stress state. For example, in polycrystalline materials, grains with higher Schmid factors for a particular slip system are more likely to deform by

that system when subjected to an external load.

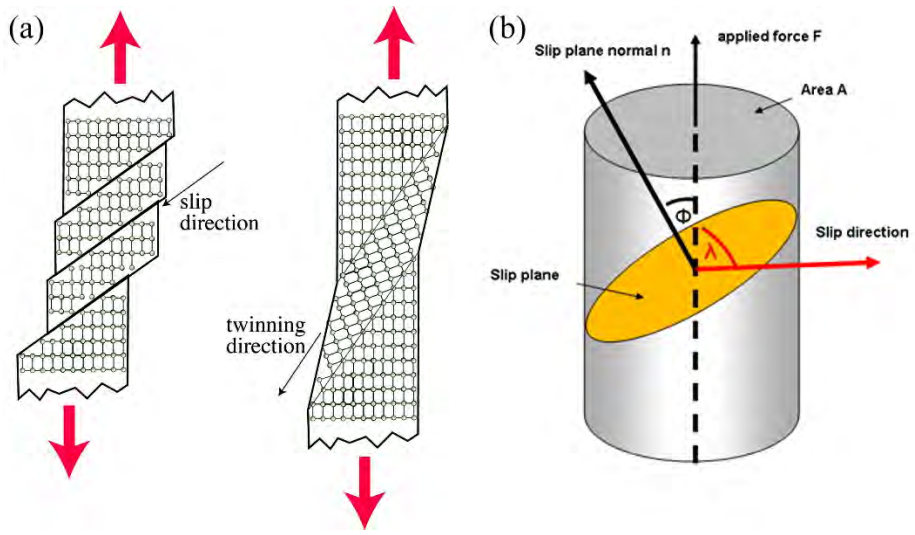

Fig. 2.9 Illustration of (a) slip and twinning, (b) the relative orientation between slip plane, direction, and applied force [85].

CPFEM is a computational framework that combines the principles of crystal plasticity with the finite element method. It explicitly models the deformation of individual grains within a polycrystalline material. The key features of CPFEM include: 1) CPFEM models each grain individually, considering its unique crystallographic orientation and deformation mechanisms. This allows for a detailed representation of the microstructure and corresponding effects on the macroscopic mechanical behaviour. 2) The method incorporates anisotropic deformation mechanisms such as slip systems and twinning, which are essential for accurately capturing the deformation behaviour of crystalline materials. 3) CPFEM enables multi-scale analysis, linking the microstructural behaviour to the macroscopic mechanical response. This is particularly useful for understanding the influence of microstructure on the overall behaviours of the material. 4) By integrating crystallographic orientation and anisotropic deformation behaviours, CPFEM

provides enhanced prediction of the mechanical performance of metals under various loading conditions..

2.3.2 Framework of CPFEM

The implementation of CPFEM follows a structured methodology to model the mechanical behaviour of crystalline materials. As depicted in Fig. 2.10, this procedure is generally segmented into three primary stages: the establishment of tessellation, the determination and input of material models, and the determination and input of constitutive equations. Each step is crucial for accurately capturing the deformation behaviour of the material at the microstructural level.

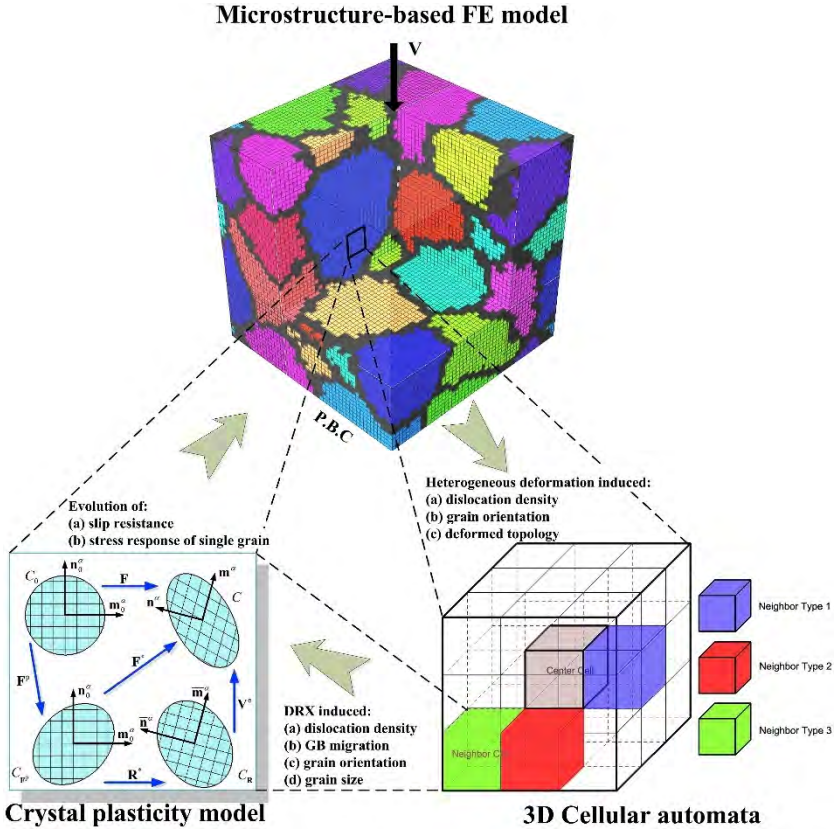

Fig. 2.10 Illustration of a common method of the utilization of CPFEM in analysis of material plasticity [86].

1) Tessellation establishment

Tessellation, or mesh generation, is the first and foundational step in CPFEM. This involves discretising the material into grains with meshing, each representing a small volume of the material. The precision and efficiency of simulations are heavily dependent on the tessellation's quality.

i. The mesh generation commences with the precise delineation of the material's geometry, encompassing its boundaries and intrinsic features such as grain boundaries. Subsequently, the material is discretised into a finite element grid. The selection of element type and mesh density are pivotal considerations. While a finer mesh affords greater resolution, it concurrently escalates computational expense.
ii. Within the framework of CPFEM, each grain within the polycrystalline material is commonly modelled using one or more finite elements. The orientation of these grains is of fundamental significance, as it dictates the crystallographic orientation and the associated deformation mechanisms. The initial grain structure can be derived from empirical data, such as EBSD, or synthesised through computational techniques. One widely employed method for generating the initial grain structure is Voronoi tessellation. This approach commences with a series of random seed points, each of which signifies the centroid of a grain. The space is subsequently partitioned into regions, known as Voronoi cells, surrounding each seed point, with each cell representing an individual grain. The orientation of each grain may be assigned either randomly or in accordance with experimental data.

2) Establishment and input of constitutive equations

The second step defines and implements constitutive equations based on crystal plasticity theory to model the anisotropic mechanical behavior of crystalline materials. The kinematic framework of CPFEM, based on theories by Rice [87] and Hill and

Rice [88], models material flow through dislocation motion, leading to elastic deformation, lattice rotation, and slip/twinning. The total deformation gradient $\boldsymbol{F}$ is decomposed as

$$\boldsymbol{F} = \boldsymbol{F}^{e} \cdot \boldsymbol{F}^{p} \tag{2.2}$$

Here $\boldsymbol{F}^{e}$ represents the elastic rotation and stretching of the lattice, while $\boldsymbol{F}^{p}$ corresponds to the deformation gradient component resulting exclusively from crystal slip. The instantaneous velocity gradient $\boldsymbol{L}$ is expressed as

$$\boldsymbol{L} = \dot{\boldsymbol{F}} \cdot \boldsymbol{F}^{-1} = \dot{\boldsymbol{F}}^{e} \cdot \boldsymbol{F}^{e\,-1} + \boldsymbol{F}^{e} \cdot \dot{\boldsymbol{F}}^{p} \cdot \boldsymbol{F}^{p\,-1} \cdot \boldsymbol{F}^{e\,-1} \tag{2.3}$$

In this context, the plastic deformation gradient is defined according to the flow rule as

$$\boldsymbol{L}^{p} = \dot{\boldsymbol{F}}^{p} \cdot \boldsymbol{F}^{p\,-1} \tag{2.4}$$

Then, the flow rule and hardening equations should be involved, which are different from case to case.

As for the input or utilization of these constitutive models, a user-defined subroutines is usually the best choice. For example, in commercial finite element software like ABAQUS, the constitutive equations can be implemented using user-defined subroutines (e.g., VUMAT). These subroutines allow for the custom implementation of crystal plasticity models. The user-defined subroutine must be carefully written to ensure accurate and efficient computation. Take VUMAT as instance, a VUMAT subroutine in ABAQUS includes the following components, as shown in Fig. 2.11: i. Initialization: define the initial state variables and material properties; ii. Stress update: calculate the stress and plastic strain increments based on the constitutive equations; iii. Hardening laws: Apply the selected hardening laws to update stress and state

variables.; iv. Output: return the revised stress and state variables to the finite element solver.

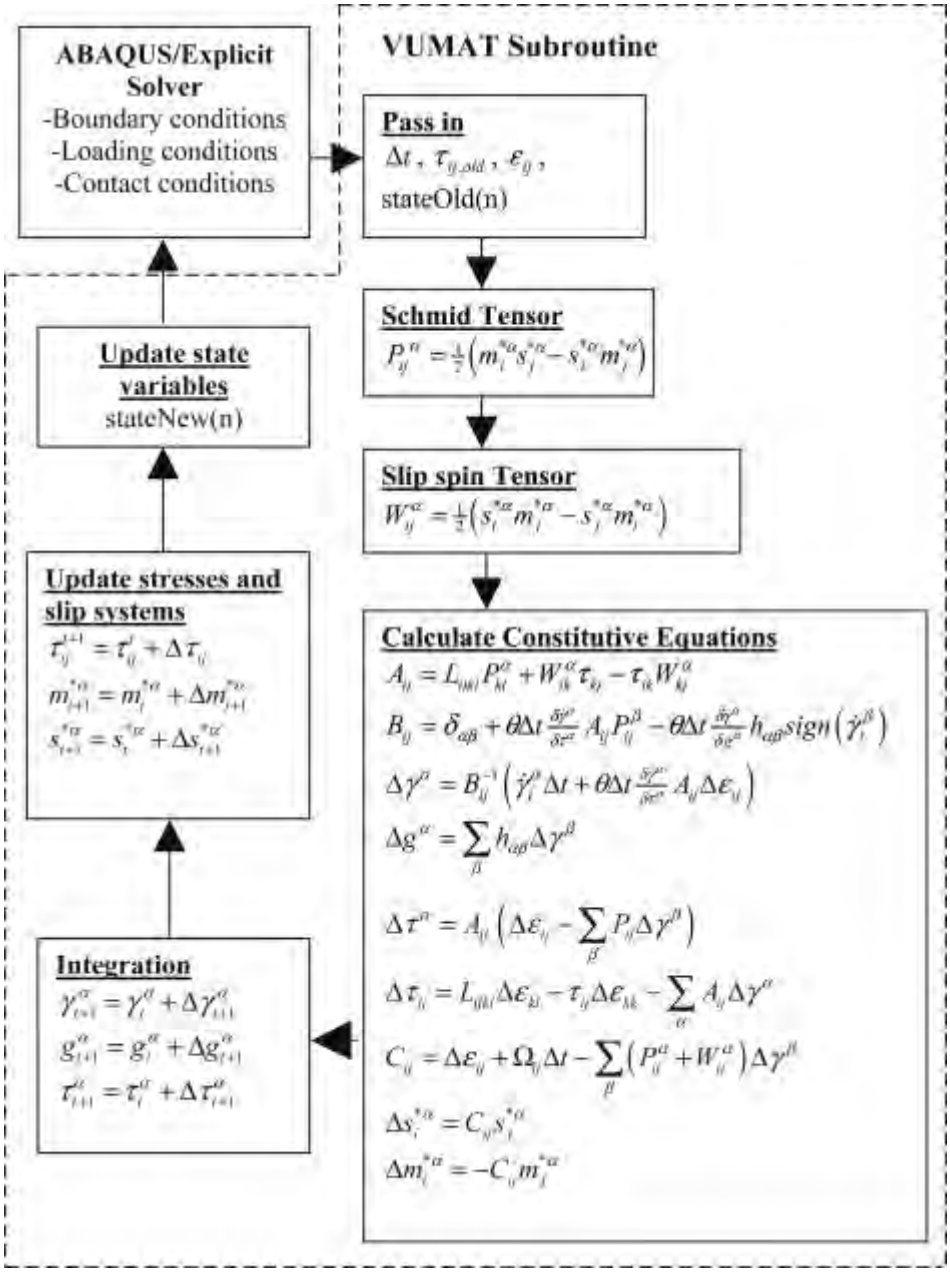

Fig. 2.11 The implementation procedure for CPFEM in ABAQUS/VUMAT [89].

3) Determination and Input of Material Parameters

The third step involves determining and inputting the material parameters that are

required for the constitutive equations. These parameters are critical for precisely characterizing the material's mechanical response and require meticulous calibration and validation.

Material parameters are typically determined through experimental testing. Common tests include tensile tests, compression tests, and microhardness measurements. These tests provide data on the material's yield stress, hardening behaviour, and other mechanical properties. Material parameters are identified by calibrating the constitutive model against experimental data. This methodology typically employs inverse analysis approaches, wherein parameters are iteratively calibrated to reduce discrepancies between computational outputs and empirical observations. Software tools like ABAQUS/CAE can be used to perform this parameter identification. For a crystal plasticity model, the material parameters might include: initial yield stress, hardening coefficient, slip or twinning system properties, etc. These parameters are subsequently utilized within constitutive relationships and finite element simulations to model material behaviour under varied loading states.

2.3.3 Applications of CPFEM in meso/micro-scaled metal-forming

Recent studies using CPFEM have mostly focused on understanding deformation mechanisms [90, 91], in-grain texture evolution [92, 93], and hardening and fracture behaviours [94, 95] by conducting simple tests, such as tension [96], compression [97], torsion [98], bending [99], while its application to understanding deformation behaviours during meso/micro-scaled metal-forming processes is very limited. This limitation is partly due to the complexity of forming processes, which involve multiple deformation stages and intricate interactions between the tooling and the workpiece. However, recent advancements in computational power and numerical techniques have enabled researchers to extend the application of CPFEM to more complex

forming scenarios, providing valuable insights into the deformation mechanisms and material behaviours.

Table 2.1 Recent examples for direct applications of CPFEM in meso/micro-scaled metal-forming

Meso/micro-scaled forming process	Reference
Embossing	Tong et al. [32] Zhang et al. [100]
Bending	Adzima et al. [101], Grogan et al. [102], Wang et al. [103], Singh et al. [104]
Deep drawing	Zhang and Dong [105], Guo et al. [29], Zhao et al. [106], Zhang et al. [107], Zhao et al. [108]
Forging	Yang et al. [109], Shao et al. [110]
Extrusion	Cao et al. [111], Feng et al. [112], Lu et al. [113], Deng et al. [114], Liu et al. [115]
Rolling	Chen et al. [116], Zhang et al. [117], Jung et al. [118]
Upsetting	Kardan-Halvaei et al. [30], Zheng et al. [119]
Ring expansion	Özdemir [120]

Table 2.1 list some examples for direct applications of CPFEM in meso/micro-scaled metal-forming. For detailed modelling methods, Zhang et al. [100] utilized CPFEM to conduct simulation of a two-stage microforming and studied the grain SEs on forming load, as shown in Fig. 2.12. Singh et al. [104] comprehensive analyse the microstructure evolution in V-bending by experiments and CPFEM simulations. Guo et al. [29] modelled a series of micro deep drawing simulations, and found the earing effect can be accurately predicted by CPFEM simulations.

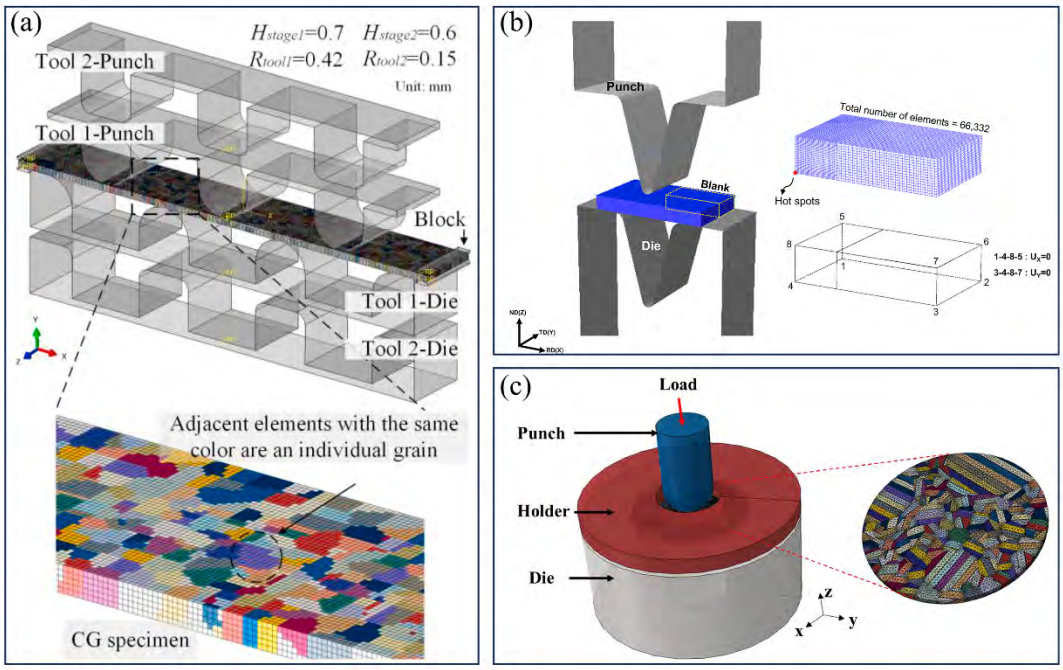

Fig. 2.12 Implements of meso/microforming processes using CPFEM: (a) embossing [100], (b) bending [104], and (c) deep drawing [29].

Despite some success cases, there are still some serious issues about directly applying CPFEM in meso/microforming processes. Firstly, compared to the vast number of studies on simulations for meso/microforming processes, the application of CPFEM is remarkably sparse. To tackle and improve meso/microforming processes and their related SEs, simulation stands out as the most practical and efficient method. The limited use of direct CPFEM applications can be explained by two key reasons: (1) the exorbitantly high computational costs; and (2) the considerable challenges in model construction. The high computational costs of CPFEM are a significant barrier to its widespread use. The detailed representation of the microstructure, including individual grains and their orientations, requires a fine mesh and complex calculations at each integration point. This leads to substantial computational demands, especially for large-scale simulations. Additionally, the iterative solution procedures and the need for high-resolution meshes further exacerbate the computational burden. The

complexity of model construction in CPFEM also poses a major challenge. Accurate representation of the material's microstructure, including grain orientations and initial texture, requires detailed experimental data or sophisticated computational methods. Additionally, integrating CPFEM into commercial finite element software typically relies on user-defined subroutines. This demands strong programming expertise and a thorough grasp of material behavior as well as numerical techniques.

Secondly, when comparing the scope of CPFEM applications to the literature on meso/microforming, the number of studies employing CPFEM remains exceedingly limited. The primary reason for this scarcity is the extremely high difficulty in model construction. On one hand, as shown in Table 2.1, none of the current applications involve material fracture and damage. Research on fracture and damage within CPFEM is still in its infancy, primarily focusing on intragranular and intergranular damage and fracture. Effective methods for general applications have yet to be developed. This means that most forming methods involving material fracture, such as blanking, heading, and progressive forming, cannot currently utilize CPFEM. On the other hand, the significant element distortion involved in the forming of complex parts presents another challenge. Whether using implicit or explicit algorithms, both can lead to numerous convergence issues or substantial reductions in increment time. These problems further increase the likelihood of CPFEM simulations, which are already computationally intensive, failing midway through the process. As a result, significant research opportunities remain for adapting CPFEM, a method well-suited for meso/micro-scale forming, to real-world applications.

2.4 Summary

This chapter offers a concise overview of the current advancements in meso/micro-

scale metal-forming processes, emphasizing fundamental concepts, SEs, and CPFEM. The chapter has been structured to build a solid understanding of the field, identify critical challenges, and highlight the research gaps focused in this thesis. Through this review, several key research gaps were identified:

1) Despite its theoretical capability to resolve grain-scale deformation, CPFEM remains underutilized for simulating multi-stage meso/micro-forming processes due to computationally prohibitive costs and challenges in modeling dynamic grain interactions. This hinders accurate prediction of size effects in progressive forming operations.
2) Current CPFEM frameworks lack robust integration of material damage and fracture mechanisms – particularly for shear-dominated processes like blanking and cutting within progressive forming systems. Effective methods to simulate grain-size-dependent fracture initiation and propagation remain underdeveloped.
3) Existing CPFEM approaches suffer from insufficient coupling with quantitative experimental data for model validation. The absence of high-resolution microstructure-deformation correlation limits confidence in predicting real-world forming behavior and final part quality.

Chapter 3 Feasibility of CPFEM in meso/micro-scaled complex shape part forming

3.1 Introduction

As discussed in Chapter 2, numerous studies have provided essential insights and actionable recommendations for the mass production of diverse meso/micro-scale sheet-forming processes. These processes include micro sheet bending, micro deep drawing, and microembossing. In particular, microembossing stands out as an excellent method for manufacturing sheet components with intricate indentations, such as ribs, channels, and lettering [121]. Additionally, there are several other product quality concerns related to SE in microembossing that require further examination. These involve the influence of grain size (G) and sheet thickness (t) on aspects such as thickness uniformity, height consistency, and surface quality. Additionally, in earlier work by Li et al. [122], a two-stage micro deep drawing (MDD) system was introduced, achieving a forming ratio of 3, compared to 2.1 for single-stage deformation with pure copper.

This chapter seeks to explore the potential of CPFEM in meso/micro-scale complex part deformation. To achieve this, a series of CPFEM simulations were performed to analyse SEs on deformation behaviours in microembossing and MDD, focusing on load-stroke relationships, thickness variations, and surface roughness. The insights and conclusions drawn not only validate the applicability of CPFEM but also provide a foundation for advancing the design of more complex parts and CP models.

3.2 Crystal plasticity constitutive model

T2 pure copper sheets were selected as the testing material mainly due to their good plastic-forming performance and corrosion resistance. The constitutive model in the CPFEM is within the framework proposed by Rice [87] and Hill and Rice [88] that only crystallographic dislocation slip leads to plastic deformation. Following Eqns. 2.2-2.4, by introducing the Schmid law, $\boldsymbol{L}^p$ can be expressed as

$$\boldsymbol{L}^p = \sum_\beta \dot{\gamma}^\alpha (\boldsymbol{m}_0^\alpha \otimes \boldsymbol{n}_0^\alpha) \tag{3.1}$$

where $\boldsymbol{m}_0^\alpha$ and $\boldsymbol{n}_0^\alpha$ are unit vectors defining the slip direction and the normal of the slip plane of the slip system α, and the quantity $\dot{\gamma}^\alpha$ is the plastic shearing rate of the slip system α. The constitutive functions for the $\dot{\gamma}^\alpha$ is [123]:

$$\dot{\gamma}^\alpha = \dot{\gamma}_0 \left|\frac{\tau^\alpha}{s^\alpha}\right|^{1/m} sign(\tau^\alpha) \tag{3.2}$$

where $\dot{\gamma}_0$ and m are reference strain rate and rate sensitivity, respectively. τ^α and s^α are the resolved shear stress and the slip resistance on the slip system α, respectively. The crystal work hardening is obtained from s^α and $\dot{s}^\alpha$.

$$\dot{s}^\alpha = \sum_\beta h^{\alpha\beta} \left|\dot{\gamma}^\beta\right| \tag{3.3}$$

with

$$s^{(\alpha)} = q^{\alpha\beta} s^{(\beta)} \tag{3.4}$$

$$h_{\alpha\beta} = q^{\alpha\beta} h_{\alpha\alpha} \ (\alpha \neq \beta) \tag{3.5}$$

where $h^{\alpha\beta}$ is hardening moduli and $q^{\alpha\beta}$ is latent hardening ratio, indicating the relationship between slip systems α and β. In this research, the FCC single slip

hardening model of Peirce et al. [124] is used:

$$h_{\alpha\alpha} = h_0 \, sech^2 \left| \frac{h_0 \gamma}{\tau_s - \tau_0} \right| \tag{3.6}$$

where h_0, τ_s and τ_0 are the primary hardening modulus, saturation stress, and yield stress, respectively, identical for all slip systems. γ represents the cumulative shear strain on all slip systems:

$$\gamma = \sum_\alpha \int_0^t |\dot{\gamma}^\alpha| \, dt \tag{3.7}$$

In this CPFEM model, the material parameters of pure copper are listed in Table 3.1.

Table 3.1 Elastic constants and work hardening parameters of pure copper used in CPFEM simulation.

Elastic constants			h_0	s_s	τ_0	$\dot{\gamma}_0$	m	q
C_{11} (GPa)	C_{12} (GPa)	C_{44} (GPa)	(MPa)	(MPa)	(MPa)	(s^{-1})	(1)	(1)
168.4	121.4	75.4	180	148	16	0.001	0.1	1

3.3 Feasibility of CPFEM in microembossing

3.3.1 Material and experimental methods

The copper sheets with the dimension of 100.0 × 12.0 × 0.1/0.2/0.3 mm were used to fabricate multi-channel structures. Before the forming process, the materials were annealed in different heat treatment conditions to obtain various grain sizes. The microstructures with the three related grain sizes for each sheet thickness were obtained by using an optical microscope, as shown in Fig. 3.1. Three different grain

sizes are sufficient to reveal the trend of SEs induced issues as the difference of the grain sizes is quite significant. The grain sizes of three different samples were measured to get the average grain size by the linear intercept method according to ASTM E112 standard.

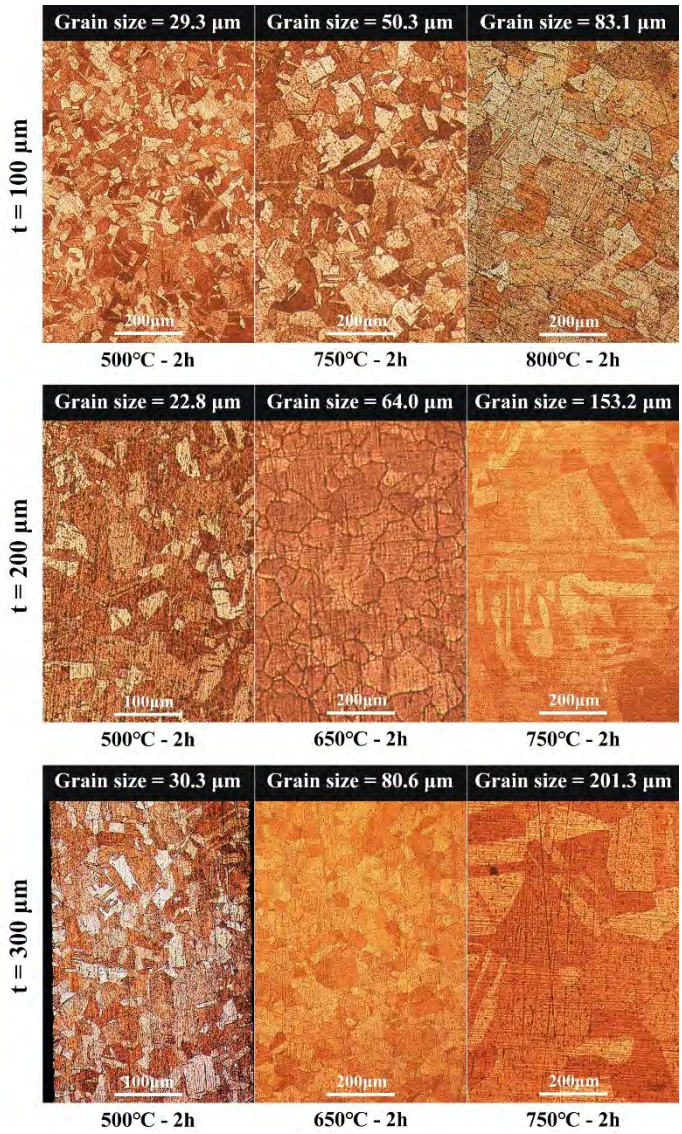

Fig. 3.1 Microstructures of the annealed copper sheets with thicknesses of 100, 200, and 300 µm and the related annealing conditions and average grain sizes.

In this research, multi-channel structures were fabricated to explore the SEs in the microembossing process. The schematic diagram of the microembossing system and

relevant dimensions of punches and dies are shown in Fig. 3.2, which consists of three sets of punches and dies for copper sheets with three thicknesses. The raised and sunken parts of those punches and dies matched each other, which was the most notable feature of microembossing. The installation of the microembossing system is shown in Fig. 3.2 (a), which performed the processing on a programmable MTS testing machine. All surfaces in the tooling assembly that may come into contact with the material were controlled to a roughness of Ra 0.8. Moreover, machine oil was applied in this experiment to lubricate all interfaces to reduce the frictional effect. The forming speed was 0.005 mm/s. As a result, the influence of strain rate could be ignored. The punch strokes for the copper sheets with the thickness of 100, 200, and 300 μm were 250, 500, and 750 μm, respectively. The microformed multi-channel structures and their designed dimensions are shown in Fig. 3.3.

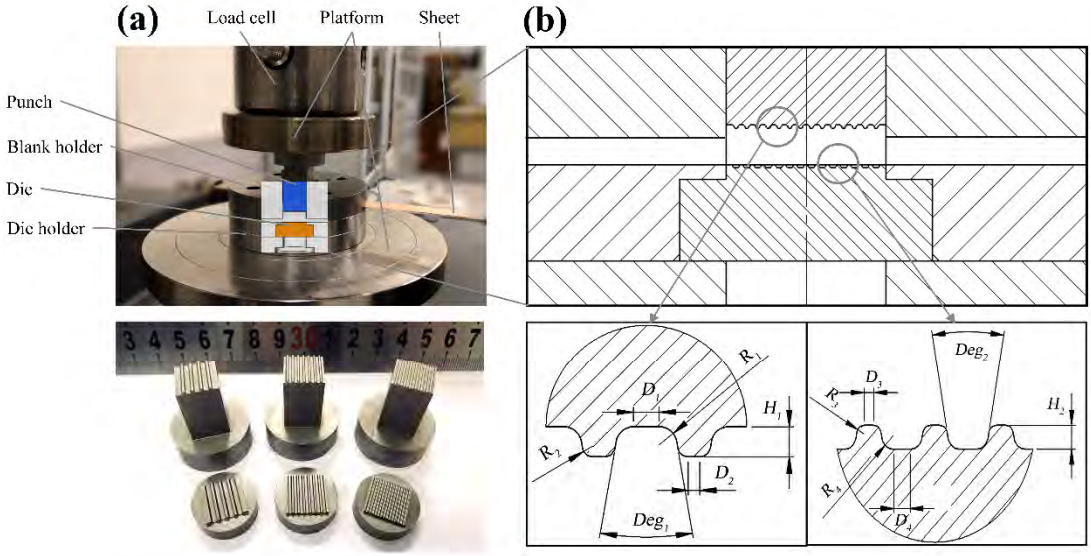

Thickness (μm)	Dimensions											
	D_1 (mm)	D_2 (mm)	D_3 (mm)	D_4 (mm)	R_1 (mm)	R_2 (mm)	R_3 (mm)	R_4 (mm)	H_1 (mm)	H_2 (mm)	Deg_1 (°)	Deg_2 (°)
100	0.22	0.1	0.12	0.2	0.15	0.09	0.09	0.15	0.25	0.25	20	20
200	0.44	0.2	0.24	0.4	0.3	0.18	0.18	0.3	0.5	0.5	20	20
300	0.66	0.3	0.36	0.6	0.45	0.27	0.27	0.45	0.75	0.75	20	20

Fig. 3.2 (a) The microembossing system; (b) the dimensions of punches and dies.

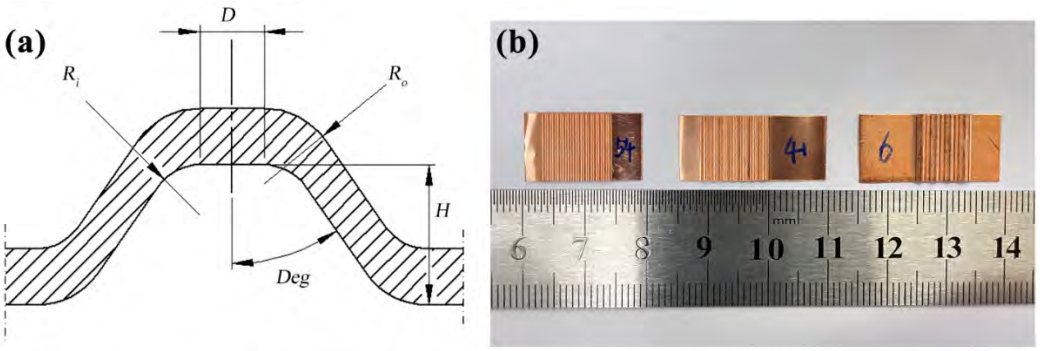

Thickness (μm)	Number of channels	Dimensions					
		L (mm)	D (mm)	H (mm)	R_o (mm)	R_i (mm)	Deg (°)
100	14	12	0.11	0.25	0.13	0.09	35
200	7	12	0.23	0.50	0.26	0.18	35
300	4	12	0.34	0.75	0.39	0.27	35

Fig. 3.3 (a) The designed multi-channel structure and its dimensions; (b) the microembossed multi-channel structures.

3.3.2 CPFEM modelling

The commercial software ABAQUS/explicit with a modified VUMAT subroutine based on the UMAT subroutine proposed by Huang [125] was applied for this CPFEM simulation. The initial grain orientations were randomly distributed. Random Euler angles are not used in the CPFEM modelling to generate the crystal orientations because they may lead to an uneven distribution of orientations. Two non-parallel vectors in the global coordinate system, and two corresponding randomly generated vectors in the local coordinate system of the cubic crystal, are needed to determine the orientation of the crystal. The Voronoi algorithm divided the sheet into a certain number of cells (grains). To simulate the microembossing process, various sheet models were established with 100, 200, and 300 μm thicknesses and different grain sizes as shown in Fig. 3.1.

Considering the computational efficiency, only a small part of the deformed sheets was simulated. As illustrated in Fig. 3.4, for example, a 3D meshed part with the

dimensions of 7.5 (X-axis) × 0.3 (Y-axis) × 0.9 mm (Z-axis) with 248 grains was established to represent the experimental copper sheet with 300 μm thickness and average grain size of 201.3 μm. An area of the same colour represented a single grain with the same material properties. C3D8 elements were applied to the sheet model. Specifically, on the x-axis, half of the actual dimensions are included, so restrictions on the x-axis have been added to the symmetry plane. Based on the actual tooling design, no holders have been added to the exposed material above or below. In terms of interaction, uniform face-to-face contact has been set, and the friction coefficient has been set to 0.12. The simulation settings also followed the same forming process: the forming speed was 0.005 mm/s and the punches moved upwards after the compression was finished. Considering the accuracy of simulation results, three repeated generated models for each group were subjected to the same simulation environment.

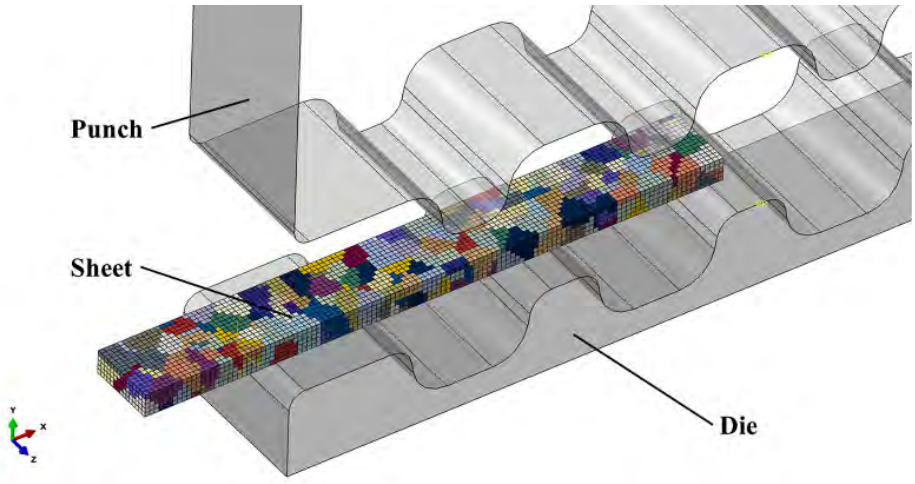

Fig. 3.4 Schematic of the CPFEM simulation setup.

3.3.3 Results and discussion

3.3.3.1 Size effects on load-stroke relations

The CPFEM-simulated and experimental deformation load and punch stroke relationships are plotted in Fig. 3.5. To assure data reliability, three repeated experimental tests average each value. The CPFEM simulation results are multiplied by the number of times the sheet model is scaled down. The simulation results agree well with the experimental results. However, the curves of CPFEM simulations all exhibit a rapid increase after the stroke approaches 90%, which is remarkably dissimilar to the experimental results. In the microembossing process, the deformation load increases approximately linearly with the punch stroke, and there is no clear division of stages. All curves with different sheet thicknesses and grain sizes exhibit the same tendency: the deformation load reduces as grain size increases, which can be explained by grain boundary strengthening [126]. Grain boundaries obstruct slip transmission and cause dislocations to accumulate. As a result, coarse-grained material with a small grain boundary volume fraction is more deformable. The simulated results overestimate the deformation load for a 100 μm thick copper sheet, while the simulated and experimental deformation load curves are relatively consistent when deforming the 300 μm and 200 μm copper sheets.

There are two kinds of SEs observed in deformation load and punch stroke relationships. One is a GSE, leading to the load deviation between simulated and experimental results for the identical thickness sheets. In 100 μm thick copper sheets, the deviation tends to rise with decreasing grain size, as shown in Fig. 3.5(a). This is attributed to the fact that as grain size varies, the grains at the corner region are subjected to varying degrees of force and exhibit harder or softer mechanical behaviour. The other one is a geometrical SE, referring to the sheet thickness in this

scenario. It is observed that the load deviation decreases with the increase of thickness. Furthermore, the microembossing process with a larger scaling factor has a smaller deformation load when vertically comparing the deformation curves of the three thickness copper sheets. One explanation is that the thinner copper sheet is softer and deforms slightly before applying longitudinal load on the punch. It can also be explained by the lubricant pocket model [12] that when the workpiece size scales down to micro scale, there will be fewer lubricant pockets, leading to an increase in the coefficient of friction and further increasing forming loads.

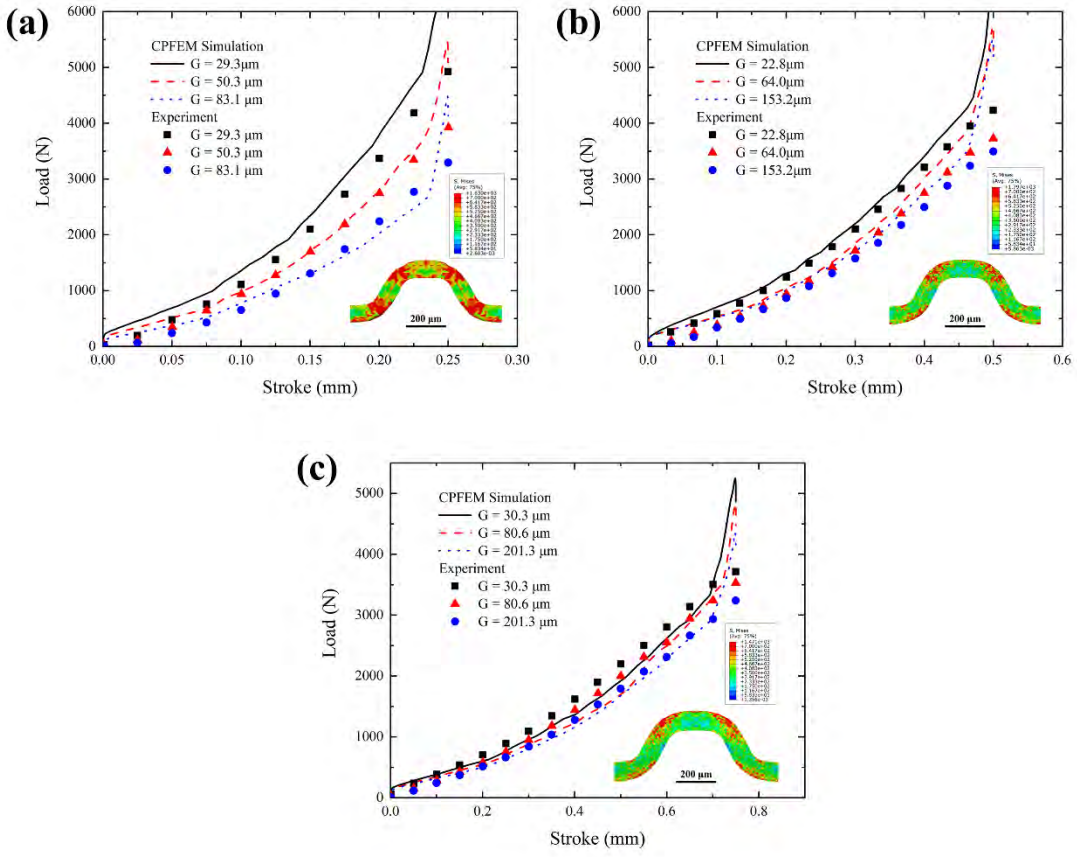

Fig. 3.5 Comparison of the load-stroke curves (symbols) between CPFEM simulations, and experiment with sheet thickness of (a) 100, (b) 200, and (c) 300 μm.

3.3.3.2 Size effects on thickness variation

The dimensional accuracy of microformed components is crucial for material design, process development, and product quality assurance. The microembossing process can be regarded as a plane strain scenario. Therefore, under longitudinal pressure, the sheets are supposed to be compressed and become thinner. As the punch moves downwards, the outer material is dragged into the die cavity and towards the central axis, while the inner material is pushed downwards. The schematic diagram of the thickness measuring locations and results of the multi-channel structure with various thicknesses are depicted in Fig. 3.6. Only the middle channels were selected because other channels present varying degrees of horizontal asymmetry. As shown in Fig. 3.6 (a), only a half-section of the middle channel needs to be measured due to the symmetric shape.

As shown in Fig. 3.6 (b-d), the thickness variation distributions in various sheet metals show similar tendencies that the thickness of the sheet first reduces from location A to C and then increases from D to F. The thickness reduction is small at points A and F, which indicates that the material in these locations deforms slightly. However, in zones BC and CD, the thickness decreases rapidly. It can be seen that the thinnest points are located at point C, with 17.95%, 22.27%, and 22.15% thickness reduction in 100, 200, and 300 μm thick copper sheets, respectively. The experimental results show that the thickness reduction is increased with grain size for the same thickness. The simulated results, however, do not show a similar tendency. The disparity between simulation and experiment is increased with grain size, owing to the stronger anisotropy of a single crystal. When the Schmid factor of the grain is very small under horizontal load, the thickness reduction of this zone will be minor due to the smaller strain. In addition, the thickness differences between the thickest and thinnest locations in the final

microformed parts are approximately 15.08%, 16.40%, and 14.87% in 100, 200, and 300 μm copper sheets, respectively, and increase with grain size for the same thickness sheets. The thickness difference in the CPFEM simulation results, however, is much smaller, as shown in Fig. 3.6 (b-d). This phenomenon indicates, to some extent, that CPFEM should be used under limited conditions to obtain more accurate results. For material with coarse grains, fewer grains are touching the tooling corner. The anisotropy of individual grain is enhanced, leading to more uneven deformation.

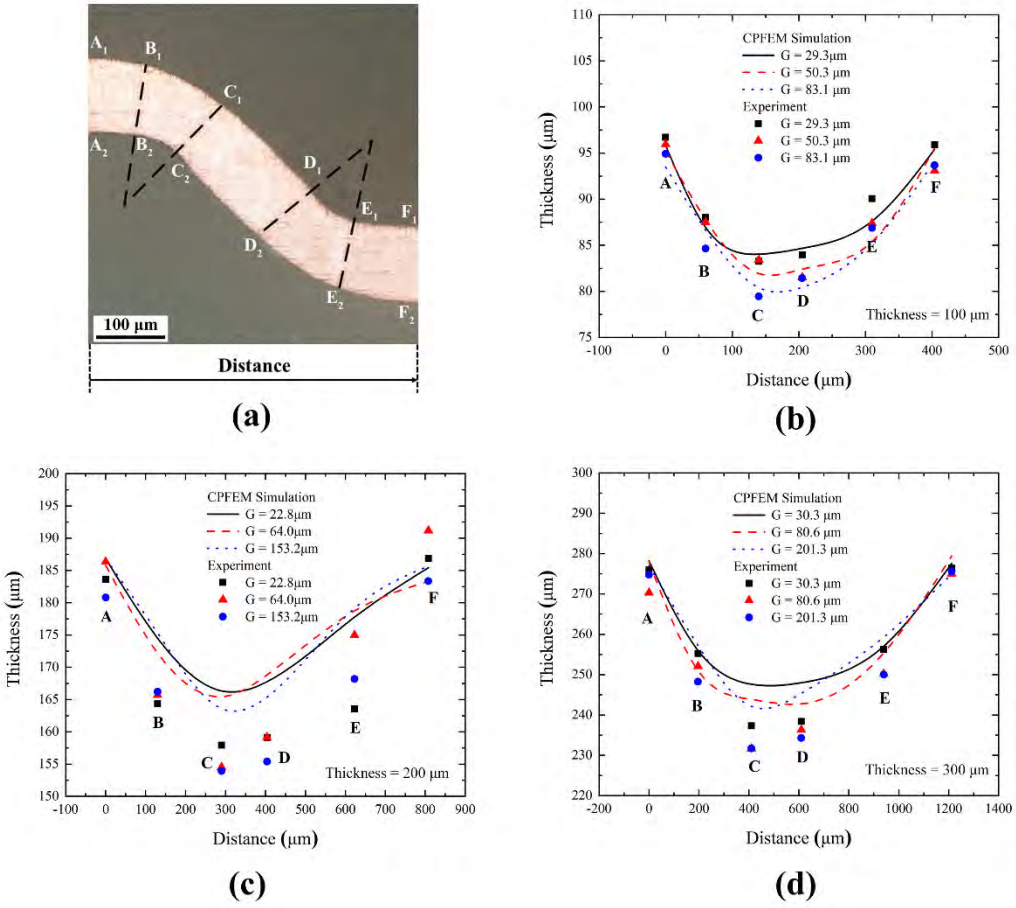

Fig. 3.6 (a) Schematic illustration of thickness measuring locations; comparison of the thickness distribution with sheet thicknesses of (b) 100, (c) 200, and (d) 300 μm.

3.3.3.3 Size effects on surface quality

The surface quality of microformed products has a considerable impact on the assembly and use of the part. In particular, when part feature size is scaled down to micro-level, its surface quality becomes more influenced by grain size due to the anisotropy of single grains. To investigate the SEs affected surface roughening, the morphology of the multi-channel structure surface was observed by SEM, and 3D Laser Scanning Microscope was used to measure the surface roughness. Fig. 3.7 (a) shows the schematic illustration of the roughness measuring locations. Since the accumulated strain on the channel bottom surface is minimal and the surface roughness of the sidewalls is challenging to measure, the channel peak surface on the top surface and bottom surface are chosen as the measuring locations. The predicted surface roughness was also calculated by the CPFEM simulation results:

$$R_a = \frac{1}{n}\sum_{i=1}^{n}\left|h_i - \bar{h}\right| \tag{3.8}$$

where h_i are the heights of the selected nodes in the surface and $\bar{h}$ stands for the average height. As shown in Fig. 3.7 (b-d), the surface roughness is decreased with grain size, and the value does not show a linear correlation with it. This GSE can also be observed from the CPFEM simulation results. Some grains tend to deform horizontally, and others will move along the thickness direction, which results in surface roughening [127]. As grain size increases, the surface grain is subject to less restriction, causing severe inhomogeneous deformation of the surface grains and thus increasing the surface roughness. It can be seen that the error also increases with grain size for the same reason. This SE can also be explained by the lubricant pocket model. Lubricant might be trapped in the roughness valleys or squeezed out when the tooling approaches the lubricated material surface. The so-called open lubrication pocket

(OLP) is generated when the lubricant is squeezed out. The asperity bears the deformation stress and is deformed to become flat, resulting in a larger actual contact area and an increased friction. The so-called close lubricant pocket (CLP) is generated when the lubricant is caught in the roughness valleys. The lubricant shares a portion of the deformation load, resulting in a reduction in normal pressure on the asperities. For the same thickness sheet, larger grain size leads to fewer lubricant pockets, leading to the increased friction and surface roughening. On the other hand, Fig. 3.7 (b-d) shows that the top surface is rougher than the bottom surface. The difference is mainly attributed to strain accumulation. In the microembossing process, the top surface and bottom surface are under different loading and contacting conditions with tooling, resulting in unequal strain and further roughness differences.

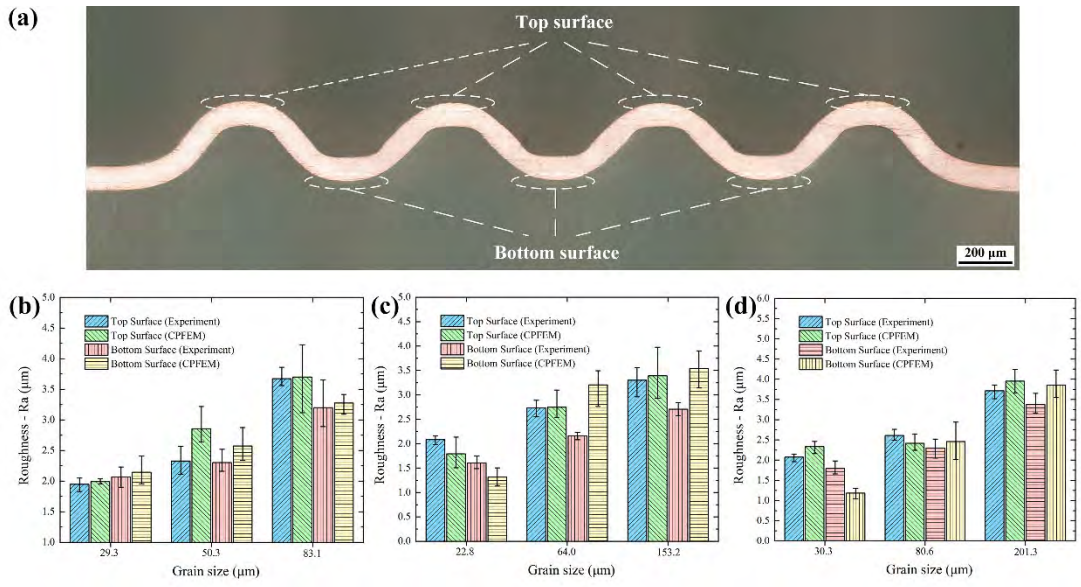

Fig. 3.7 (a) Schematic illustration of the surface roughness measurement locations; the surface roughness with sheet thicknesses of (b) 100, (c) 200, and (d) 300 μm.

3.4 Feasibility of CPFEM in two-stage micro deep drawing

3.4.1 CPFEM modelling

A pure copper sheet measuring 200 μm in thickness was employed for the two-stage deep drawing process. The material's average grain sizes, achieved through different annealing temperatures, were 25.5, 68.8, and 89.8 μm, respectively. Fig. 3.8 (a) illustrates the tooling designs. For simulating the two-stage micro deep drawing, the punches and dies for Stage I and Stage II were arranged as depicted in Fig. 3.8 (b). During Stage I, the first punch moves downward, and upon reaching the predetermined stroke, it retracts, allowing the second punch to complete Stage II. A friction coefficient of 0.1 was assigned to all potential contact surfaces. To optimize computational efficiency, only one-eighteenth of the copper blank was modelled, with cyclic symmetry boundary conditions applied to maintain realism and precision.

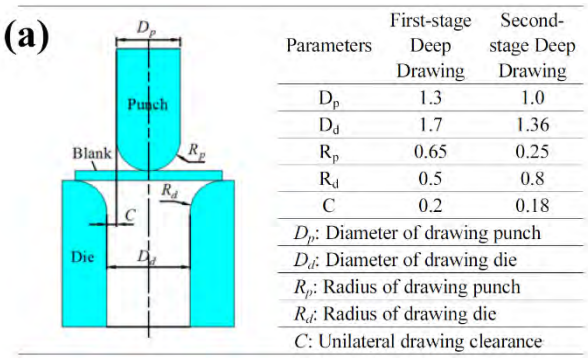

Parameters	First-stage Deep Drawing	Second-stage Deep Drawing
D_p	1.3	1.0
D_d	1.7	1.36
R_p	0.65	0.25
R_d	0.5	0.8
C	0.2	0.18

D_p: Diameter of drawing punch
D_d: Diameter of drawing die
R_p: Radius of drawing punch
R_d: Radius of drawing die
C: Unilateral drawing clearance

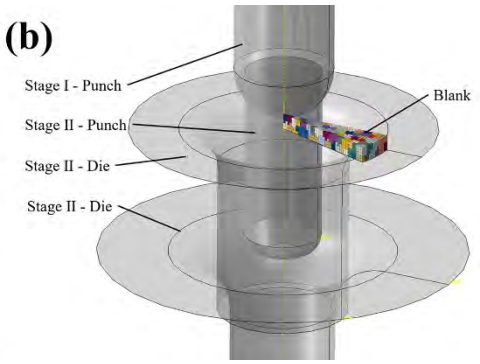

Fig. 3.8 (a) Design and dimension of tooling system; (b) simulation setup of the two-stage micro deep drawing process.

3.4.2 Results and discussion

3.4.2.1 Size effects on load-stroke relations

The cross-sections of the deformed parts following Stages I and II are shown in Fig. 3.9. It is evident that the profiles of the deep-drawn cups align closely between the

CPFEM simulations and experimental outcomes. The load-stroke curves derived from the CPFEM simulations are illustrated in Fig. 3.10. In terms of the overall trend of those curves, in both are consistent with the previous study in micro deep drawing [128], exhibiting a general upward and then downward tendency. The impact of grain size on the differences in the load-stroke relations can also be seen. It is discovered that the load lowers as grain size rises. This can be explained by two factors. One reason is that as grain size increases, the proportion of grain boundaries diminishes. Since grain boundaries act as the main obstacle to dislocation motion, their reduction enables the material to deform more easily. Another reason is that the proportion of surface grains that are less constrained increases. Furthermore, in both deformation stages, the curves from simulation utilizing material with a grain size of 25.5 μm exhibit characteristics that distinguish them from the others.

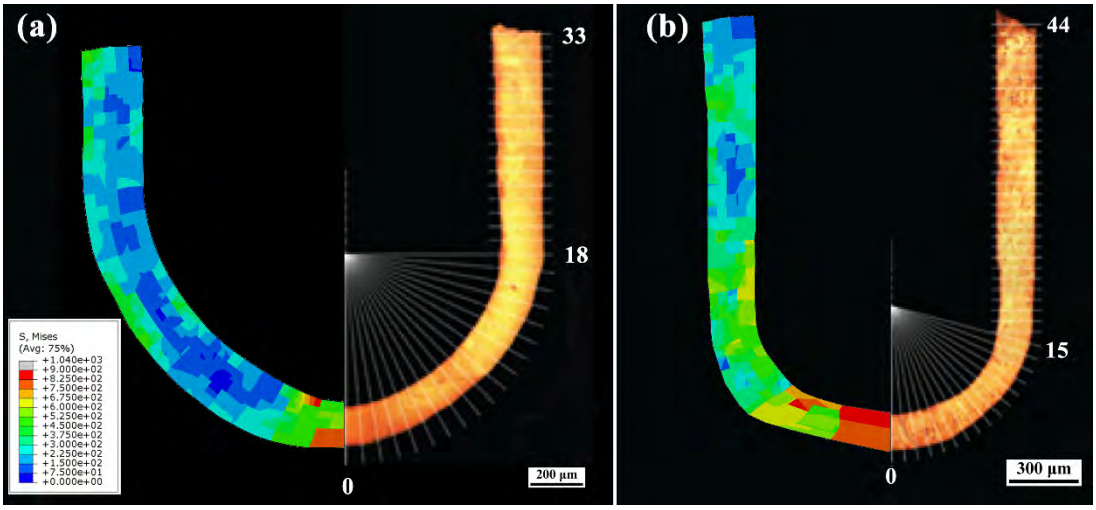

Fig. 3.9 Formed parts from simulated and experimental results: (a) Stage I and (b) Stage II.

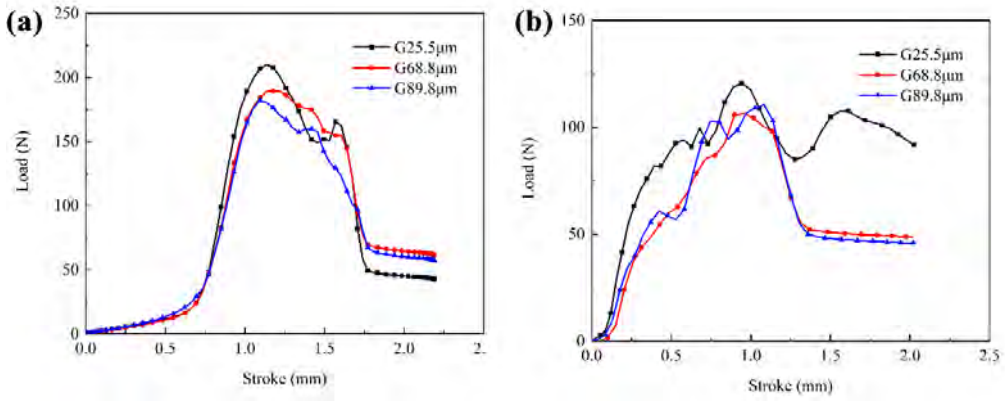

Fig. 3.10 Load-stroke curves for different-grained materials and stages: (a) stage I and (b) stage II.

3.4.2.2 Size effects on thickness variation

Fig. 3.9 also illustrates the schematic of the thickness tracking nodes used for measurements. The symmetrical half was employed for comparing and analysing geometric accuracy. As seen in Fig. 3.11, the thickness distribution is non-uniform. Measurements of the formed part from Stage I (Fig. 3.11 (a)) reveal that, in experimental results, the thickness first decreases from the bottom to the corner and then increases toward the wall. However, CPFEM simulations show a faster thickness increase at the corners. Overall, the cup wall appears thicker in the simulated results. Additionally, a clear grain SE is observed, with thickness decreasing as grain size increases. This is because materials with a grain size of 25.5 μm have more grains in the thickness direction compared to coarse-grained materials. Due to grain boundary strengthening and the growth of inner grains, the material becomes harder to deform in the thickness direction. This grain SE is also linked to surface roughening, which will be discussed in the next section.

For the thickness distribution of the final cup depicted in Fig. 3.11 (b), the experimental and CPFEM simulation results align more closely. A notable thickness

reduction is observed from the bottom to the corner area. This is primarily because, during Stage II, the contact between the punch and the material occurs mainly in the corner region.

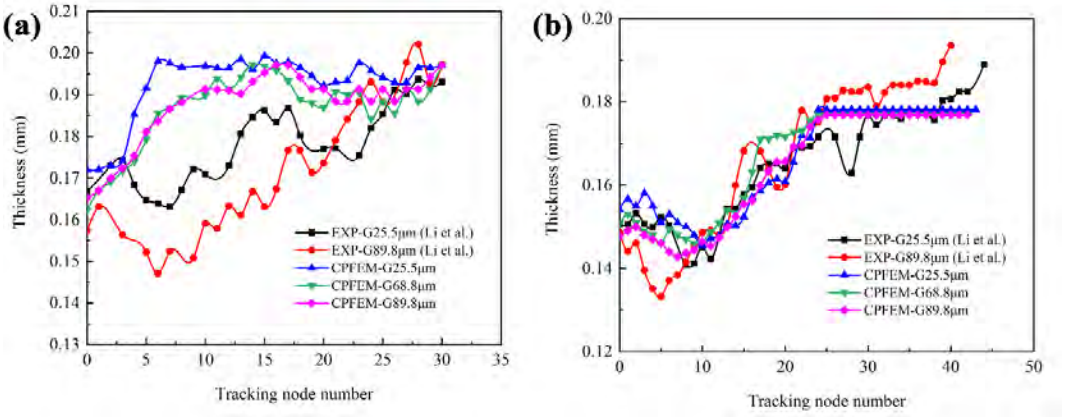

Fig. 3.11 Thickness variation of the formed parts: (a) Stage I and (b) Stage II.

3.4.2.3 Size effects on surface roughness

As shown in Fig. 3.12, the roughness of the cup wall is almost the same for each stage. For the formed part in Stage I, CPFEM simulations overestimate the surface roughness. In the final part, the roughness is smaller than that in Stage I. This occurs because, in Stage II, the entire cup wall undergoes an ironing process, resulting in a smoother surface. Furthermore, the simulation accurately predicts the surface roughness of the final cup. However, the overall error in each dataset remains relatively high.

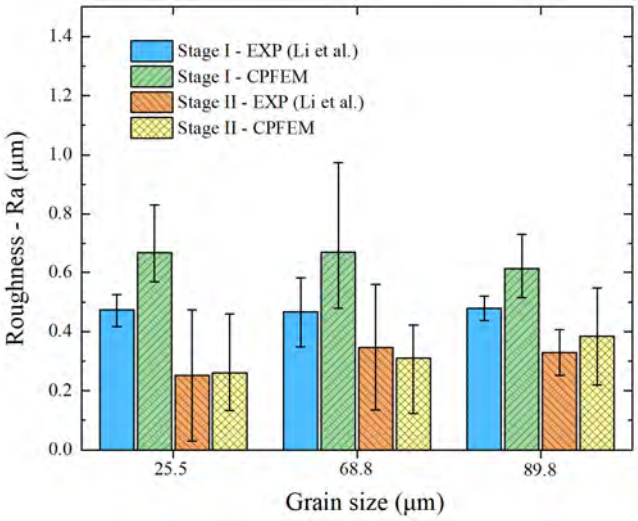

Fig. 3.12 Roughness at the wall of the formed parts.

3.5 Summary

To assess the feasibility of CPFEM in meso/microformed complex-shaped parts, this chapter examined the impact of thickness and grain size on load-stroke relationships, dimensional accuracy, and surface roughness in products produced through microembossing and two-stage deep drawing processes. The following conclusions can be drawn from this study:

1) In the microembossing process, deformation stress rises nearly linearly with punch stroke. As sheet thickness and grain size increase, CPFEM simulations more accurately predict the load-stroke relationship. With larger grain sizes, thickness reduction becomes more pronounced in sheets of the same thickness. The thinnest area is located at the edge of the corner zone, and CPFEM simulations tend to underestimate the extent of thickness reduction and variation. Surface roughness and its variability increase with grain size for sheets of the same thickness, a trend also confirmed by CPFEM simulations.
2) In the two-stage deep drawing process, the deformation load initially rises and

then declines with the punch stroke in both stages. The load decreases as grain size increases. The thinnest area is also found in the corner zone. This CPFEM model effectively predicts the thickness distribution of the microformed cup. After Stage II, the surface quality of the part improves, and the accuracy of CPFEM in predicting surface roughness is acceptable.

3) However, some limitations were also found when using CPFEM to study size effect issues. First, the study used randomly generated initial microstructures, and it remains to be seen whether this accurately reflects actual processing conditions. Second, although the size effect was accurately predicted in terms of part size, there were still some numerical errors. Last, in both processes, only the elastic and plastic deformation of the sheet material is considered, excluding material fracture, which is also common in mass productions.

Chapter 4 Exploration of Size Effects in Complex Progressive Microforming by Using CPFEM: Integration of Meso/Micro-scaled System, CPFEM Framework, and Interplay Analysis

4.1 Introduction

As reviewed in Chapter 2 and Chapter 3, the feasibility of CPFEM in meso/microforming simulation has been validated. However, all the forming processes mentioned in these literatures are “simple” forming, which means there is no material fracture occurring. At present, it is still a difficult problem to accurately embed material fracture models into the CPFEM framework, let alone for complex part forming issues.

To develop an integrated meso/micro-scaled progressive forming system combining product design, process analysis, and CPFEM simulation, and utilize it to investigate the interplay between scale-dependent deformation behavior, size effect mechanisms, and final part quality (e.g., dimensional accuracy, surface integrity, mechanical properties) across diverse product geometries. In this chapter, a more complex forming method, progressive forming, is selected to apply CPFEM simulation involving fracture to validate the superiority and feasibility of this method in meso/microforming. Progressive microforming, as the term suggests, involves the production of micro-scaled components with intricate shapes directly from metal sheets, achieved through a succession of processing steps. This method offers several advantages, such as overcoming the difficulties of positioning, transportation, and ejection, as well as

simplifying tooling design, by conducting multiple steps simultaneously, thereby saving a considerable amount of time. To reliably anticipate SE and thus improve the precision of progressive microforming and the manufacturing quality of micro parts, it is imperative to develop an efficient simulation framework for progressive microforming, which would enable the prediction and simulation stage to be precise, defect-free, and stable. The examination of SEs has encompassed a wide range of parameters, including loading conditions, dimensional accuracy, geometry irregularity, and surface quality, and has been conducted using both experimental and simulated methods. In recent years, the utilization of CPFE-based methods to analyse material fracture has become a prevalent practice. A fracture model that does not rely on the element deletion method enters the view of researchers, namely, the cohesive zone model (CZM). In finite element analysis, CZM refers to the insertion of cohesive elements with or without thickness between the desired material elements, allowing for the separation of elements to occur without affecting the overall material volume when the cohesive elements are deleted [129]. The present research endeavours to employ a newly devised CPFE-CZM method to simulate the intricate deformation behaviour caused by SEs in the context of progressive microforming. As a case study, a hexagonal socket component frequently utilized in electronic devices was selected, and a progressive microforming system comprising three operations of two-step extrusion and blanking using CuZn32 sheets were developed. The deviations in product quality and mechanical responses caused by SEs were analysed by comparing results from FEM simulations, CPFE-CZM simulations, and experiments. This comparison included strain patterns, load-stroke curves, dimensional accuracy, geometric imperfections, surface defects, and surface roughness. This work not only provides a more accurate and effective simulation method for all progressive forming processes but also will be the basis for more complex CP-based models and processing

methods in the next research work.

4.2 Material and experimental methodology

4.2.1 Testing materials and uniaxial tensile test

To thoroughly investigate the grain SEs, the brass sheet material with a thickness of 1000 μm was subjected to a range of heat treatments with varying conditions, including 450℃-1h, 600℃-1h, and 700℃-2h. Microstructural observations were made through both optical microscopy and electron backscatter diffraction (EBSD), as depicted in Fig. 4.1. The composition of the brass CuZn32 sheet is shown in Table 4.1. The samples were cut, polished, and then etched for 8-10s, while those intended for EBSD examination underwent electrolytic polishing. The acquisition and analysis of images were executed using the HKL 5-channel software package in conjunction with the EBSD system, with step size parameters of 1 μm and 2.5 μm, respectively. Data from the EBSD tests were utilized in the crystal plasticity model as described in Section 4.3, enabling a more accurate determination of average grain sizes for modelling and constitutive model calibration purposes. In this study, CuZn32 sheets with varying average grain sizes of 17.5 μm (fine grain - FG), 62.1 μm (medium grain - MG), and 157.7 μm (coarse grain - CG) were utilized in both uniaxial tensile tests and the progressive microforming process. The pole figures of the sheets for various grain sizes with a reference direction norm to the RD-ND section are illustrated in Fig. 4.2 (a).

Quasi-static uniaxial tensile tests were conducted along RD using a programmable MTS testing machine and an extensometer, and sample dimensions are illustrated in Fig. 4.2 (b). The tests were performed at a strain rate of 0.001 s-1 at room temperature to determine the correlation between grain size and the mechanical response of the

specimens. The engineering stress and strain data can be directly obtained from the software linked with the MTS and extensometer, which would be transferred to true stress and strain data. The test setup and sample configurations followed ASTM: E8/E8M standards and three samples were prepared for each grain size. The average true stress-strain response of the three samples was used to represent their macroscopic constitutive relationships. The goal of these experiments was to provide material information that could be integrated into both the conventional FEM framework and the CPFEM framework.

Table 4.1 Chemical composition of the as-received CuZn32 sample.

Content (mass fraction, %)						
Cu	Fe	Sb	Bi	P	Pb	Zn
67.50	0.1	0.005	0.002	0.01	0.03	Bal.

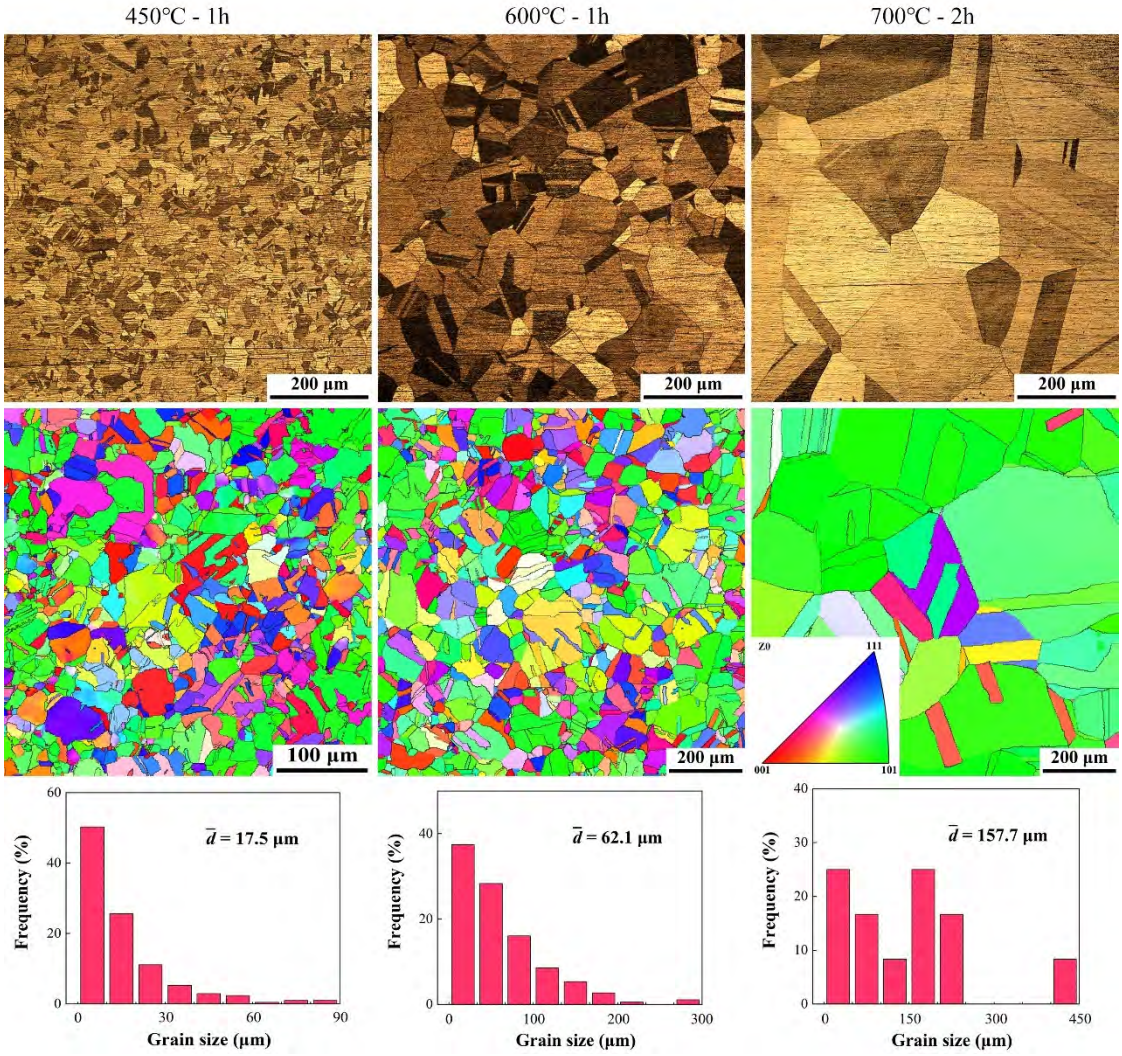

Fig. 4.1 The metallographic images and EBSD grain orientation mappings of the CuZn32 sheets under heat treatment conditions of 450˚C-1h, 600˚C-1h, and 700˚C-2h. The average grain sizes were calculated from the EBSD results as 17.5 μm, 62.1 μm, and 157.7 μm, respectively.

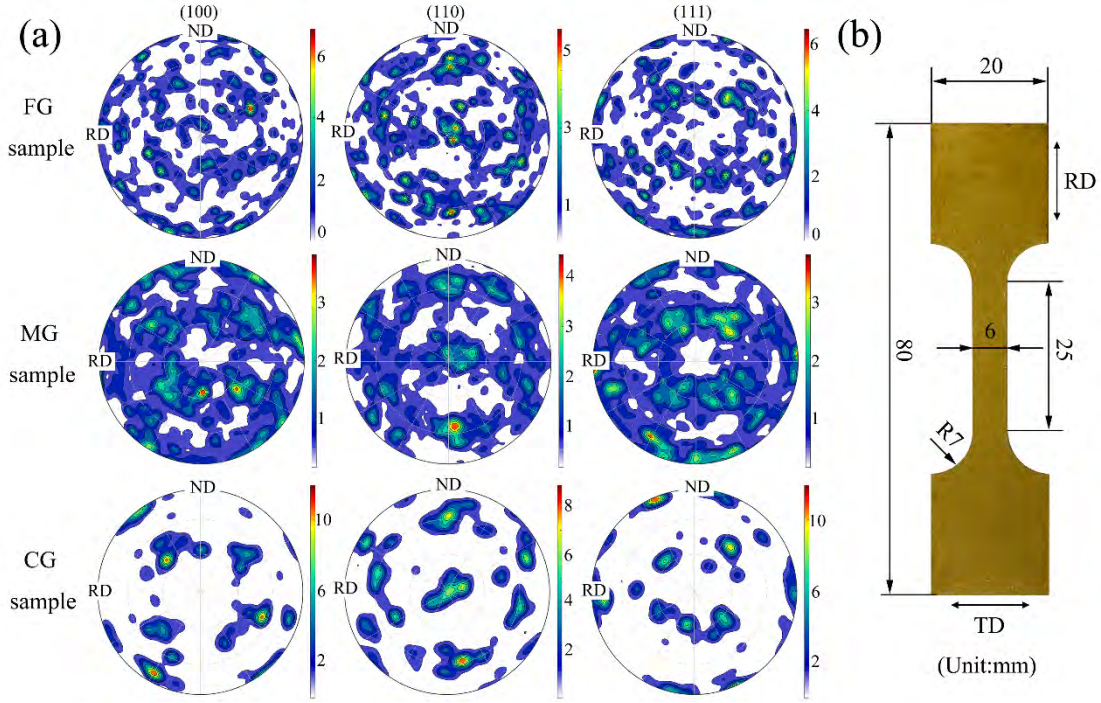

Fig. 4.2 (a) Pole figures of CuZn32 for different initial grain sizes with a reference direction norm to RD-ND section and (b) specimen design for the uniaxial tensile tests.

4.2.2 Progressive microforming process

Through progressive microforming, the study fabricated a hexagonal socket part as shown in Fig. 4.3 (c). Such socket parts with similar geometric configurations are typically produced using turning or extrusion processes. However, progressive forming has high efficiency and capacity to produce high-quality products. The tooling system utilized in the study, as illustrated in Fig. 4.3 (a), consists of a platform, a blank holder, a die holder, a bottom plate, and three sets of punch and die, all made of Cr12 cold-work die steel. During the microforming process, an 80 mm × 20 mm × 1 mm brass sheet was fed through the system from left to right. processing by 20 mm per step. Following two forward extrusion steps and a blanking step, the final product was deposited onto the bottom plate. Step I of the microforming process employed a punch

with a 1 mm radius to affect a 0.6 mm movement along the thickness direction. The material was extruded into a 0.5 mm radius tunnel with a 0.2 mm-45° chamfer. If a columnar material is employed, the extrusion ratio at this stage would reach 2. In Step II, a hexagon socket with 0.25 mm thickness and 0.8 mm diagonal distance was formed via forward extrusion at the top of the material. Finally, in Step III, a punch with a 0.8 mm radius was used to completely cut the part. A uniform slow punch speed of 0.005 mm/s was employed to eliminate the impact of strain rate in all three steps. All surfaces in the tooling assembly that may come into contact with the material were controlled to a roughness of Ra 0.8. Mechanical oil was used as a lubricant on each interface to reduce friction. The resulting microparts are shown in Fig. 4.3 (d).

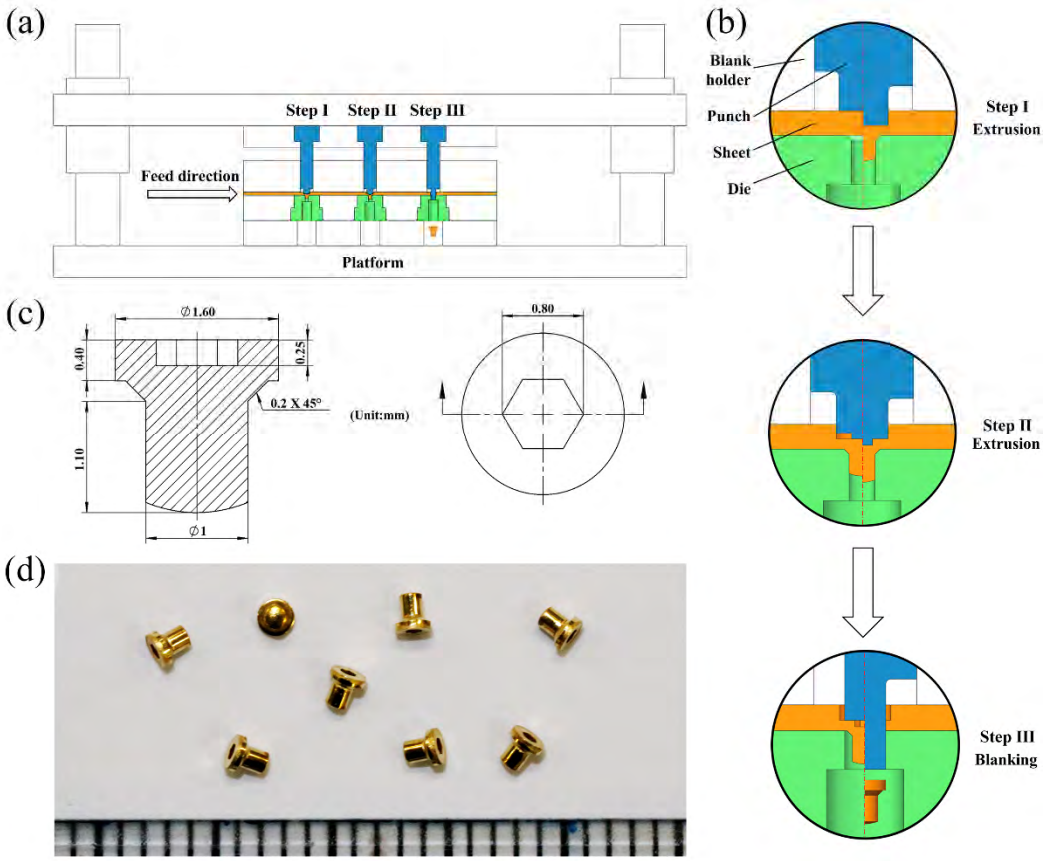

Fig. 4.3 The developed progressive microforming setup and the designed and fabricated hexagonal socket part. (a) The progressive microforming system consists

of an outer platform, blank and die holders, and three sets of punches and dies. (b) Schematic diagram of the processing in the three steps, including two extrusions and one blanking. (c) The design dimensions of the hexagonal socket part. (d) The final fabricated hexagonal socket part made by CuZn32.

4.3 Constitutive relations and modelling details

4.3.1 Crystal plasticity constitutive model

The total deformation gradient $\boldsymbol{F}$, imparted upon a crystalline material by means of crystal slip and twinning, can be decomposed into two constituent parts: the plastic deformation gradient $\boldsymbol{F}^p$ (from slip and deformation twinning) and the elastic deformation gradient $\boldsymbol{F}^e$ (from the reversible stretching and rotation of the crystal lattice):

$$\boldsymbol{F} = \boldsymbol{F}^e \cdot \boldsymbol{F}^p = \boldsymbol{F}^e \cdot \boldsymbol{F}^{twin} \cdot \boldsymbol{F}^{slip}. \tag{4.1}$$

The velocity gradient tensor $\boldsymbol{L}$ can be composed of the elastic deformation velocity gradient tensor $\boldsymbol{L}^e$ and the plastic deformation velocity gradient tensor $\boldsymbol{L}^p$ as:

$$\boldsymbol{L} = \dot{\boldsymbol{F}} \cdot \boldsymbol{F}^{-1} = \dot{\boldsymbol{F}}^e \cdot \boldsymbol{F}^{e\,-1} + \boldsymbol{F}^e \cdot \dot{\boldsymbol{F}}^p \cdot \boldsymbol{F}^{p\,-1} \cdot \boldsymbol{F}^{e\,-1} = \boldsymbol{L}^e + \boldsymbol{L}^p, \tag{4.2}$$

$$\boldsymbol{L}^p = (1 - f^{tw}) \sum_{\alpha}^{N^s} \dot{\gamma}^{\alpha} (\boldsymbol{m}^{\alpha} \otimes \boldsymbol{n}^{\alpha}) + \sum_{\beta}^{N^{tw}} \dot{\gamma}^{\beta} \left(\boldsymbol{m}^{\beta} \otimes \boldsymbol{n}^{\beta}\right). \tag{4.3}$$

Here $\boldsymbol{L}^p$ is contributed by 12 {111} <110> slip systems and 12 {111} <112> twinning systems [130]. $\dot{\gamma}^{\alpha}$ and $\dot{\gamma}^{\beta}$ denote the shearing rate on the α^{th} slip system and β^{th} twinning system. $f^{tw} = \sum f^{\beta}$ is the volume fraction of all twinning systems, which can be calculated by $f^{tw} = \sum f^{\beta} = \sum \gamma^{\beta} / \gamma^{tw}$. In this equation, γ^{β} is the calculated shear strain in the β^{th} twinning system, and γ^{tw} is the reference total twinning shear strain. In FCC materials, γ^{tw} =0.707 [131]. N^s and N^{tw} are the numbers of

slip and twinning systems, taking the value of 12. $\boldsymbol{m} \otimes \boldsymbol{n}$ is the Schmid factor.

According to the assumption of Kalidindi [130], only the effects between twinning and slip systems were considered in the working hardening model. The internal effects between different slip systems and twin systems were neglected. The following equations were used for the description of the shear rate:

$$\dot{\gamma}^{\alpha} = \dot{\gamma}_0^{\alpha} \left|\frac{\tau^{\alpha}}{g^{\alpha}}\right|^{1/m} sign(\tau^{\alpha}), \tag{4.4}$$

$$\dot{\gamma}^{\beta} = \begin{cases} \dot{\gamma}_0^{\beta} \left|\frac{\tau^{\beta}}{g^{\beta}}\right|^{1/m} & f^{tw} < 0.8\,, \\ 0 & f^{tw} = 0.8 \; or \; \tau^{\beta} \leq 0. \end{cases} \tag{4.5}$$

Here, $\dot{\gamma}_0^{\alpha}$ and $\dot{\gamma}_0^{\beta}$ are reference strain rates of slip and twinning. τ^{α} and τ^{β} are the corresponding resolved shear stresses. g^{α} and g^{β} are the critical resolved shear stress (CRSS) to resist slip and twinning evolution. m is the rate-sensitivity factor. The upper limit on the total volume fraction of twins is selected as 0.8 [130]. The evolution of g^{α} and g^{β} can be formulated as:

$$\dot{g}^{\alpha} = h_s^{\alpha} \left(1 - \frac{g^{\alpha}}{g_s^{\alpha}}\right) \sum \dot{\gamma}^{\alpha}, \tag{4.6}$$

$$h_s^{\alpha} = h_s[1 + a(f^{tw})^b], \tag{4.7}$$

$$g_s^{\alpha} = g_0 + g_{pr}(f^{tw})^{0.5}, \tag{4.8}$$

$$g^{\beta} = \eta g^{\alpha}. \tag{4.9}$$

Here, h_s^{α} is the hardening rate and g_s^{α} is the saturated slip resistance. Following the work of Salem et al. [132] and Kalidindi [133], the effects of twinning on slip can be characterized as the effects of the total volume fraction of twinning systems on h_s^{α} and g_s^{α} of the α^{th} slip system. a, b, and η are material constants. g_0 is the

saturated slip resistance in the absence of twinning and g_{pr} describes the contribution of the Hall–Petch effect.

4.3.2 Cohesive zone model

The constitutive relations governing the behaviour of the CZM in finite element analysis are described through the utilization of a Traction Separation Law (TSL). The TSL posits a dependence of the traction force on both the normal and tangential displacements. Characterization of the CZM requires consideration of three fundamental features: material stiffness, damage initiation criterion, and damage evolution law [134]. The bi-linear TSL depicted in Fig. 4.4 encompasses both the elastic and damage stages. Initially, traction strength linearly builds up as separation increases. Once it reaches the peak t_0, damages start to occur. Further separation promotes damage accumulation due to material softening. A complete material fracture occurs once the separation strength reduces to zero. The corresponding critical separation is δ_f. In this study, the maximum nominal stress criterion (MAXS) was chosen as the damage initiation criterion according to:

$$max\left\{\frac{t^n}{t_0^n}, \frac{t^s}{t_0^s}, \frac{t^t}{t_0^t}\right\}=1. \tag{4.10}$$

Here t_0^n, t_0^s, and t_0^t are the maximum stresses in the normal direction, the first shear direction, and the second shear direction, respectively. The energy-based damage evolution law was used by defining the damage energy G_c.

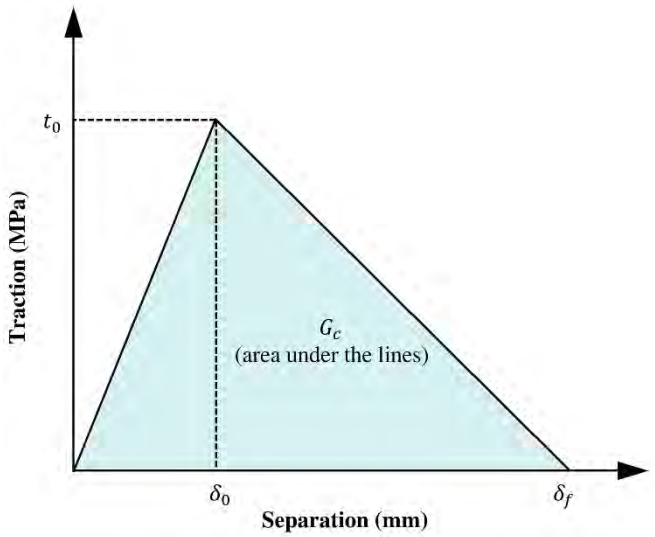

Fig. 4.4 Typical bi-linear traction-separation response used in CZM, involving two stages: the elastic deformation stage and the damage stage. The critical damage energy indicating the complete failure of the cohesive element could be identified as the area under the curve.

4.3.3 Numerical implementation and model calibration

The flowchart illustrating the sequence of algorithms employed in the new method within one single time step is presented in Fig. 4.5. The procedure starts with the calculation of the crystal plasticity component, including slip and twinning. Then, the updated stress, strain, and other variables were transferred to the calculation flow of CZM. This calculation serves as a basis for determining whether partial or complete fracture occurs during the deformation process. The whole algorithm was written in a VUMAT subroutine used for the ABAQUS/Explicit environment.

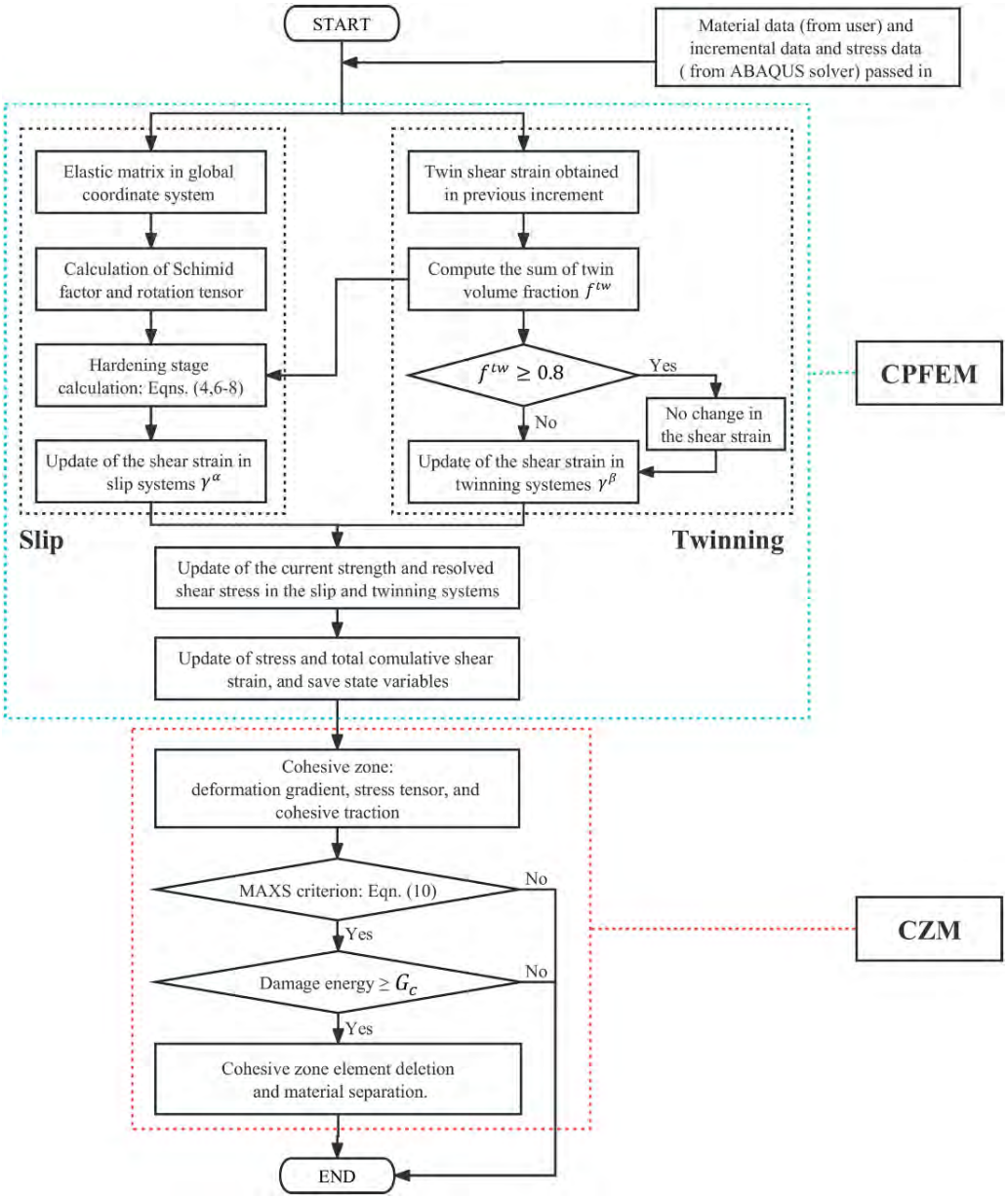

Fig. 4.5 The algorithm flow chart of the CPFEM and CZM method. The first stage represents the CPFEM part, involving the updates of stress and strain for various slip and twinning systems. The results are passed to the CZM stage to calculate the mechanical behaviour of the cohesive element and determine whether it would fail.

For the CPFEM parameters, the elastic parameters were obtained based on the work of Jia et al. [135] and Chiarodo et al. [136]. Kalilindi [133] provided the reference

values of $\dot{\gamma}_0^{\alpha}$, $\dot{\gamma}_0^{\beta}$, g_0^{β} (the initial twinning resistance), a, and b in Eqns. (4-7). The initial slip resistance g_0^{α} was calculated based on Li et al. [137]:

$$g_0^{\alpha} = \frac{1}{M}(\sigma_y + \frac{K}{\sqrt{d}}). \tag{4.11}$$

Here, the Taylor factor $M = 3.06$, and yield stress $\sigma_y = 111, 72, 55$ MPa when the average grain size is 17.5 μm, 62.1 μm, and 157.7 μm, respectively. $K = 304$ MPa $\cdot$ $\mu m^{1/2}$ represents the Hall-Petch coefficient. Other constitutive parameters were calibrated based on the residuals of the computed values and tensile test results. All parameters used for the CPFEM in this research are listed in Table 4.2.

Table 4.2 Elastic constants and hardening parameters of CuZn32 used in the CPFEM.

C_{11} (GPa)	C_{12} (GPa)	C_{44} (GPa)	$\dot{\gamma}_0^{\alpha}$ (s^{-1})	$\dot{\gamma}_0^{\beta}$ (s^{-1})	m
145	110	70	0.001	0.001	0.02
g_0^{β} (MPa)	g_{pr} (MPa)	a	b	η	
60	350	5	10	1.25	
d (μm)	g_0^{α} (MPa)	g_0 (MPa)	h_s (MPa)		
17.5	60	400	200		
62.1	36	375	190		
157.7	26	360	175		

Key parameters t_0^n and G_C^n in CZM were determined based on the research of Wang et al. [138] and Cai et al. [131]:

$$t_0^n = 1.35\sigma_f, \text{ and} \tag{4.12}$$

$$G_C^n = \frac{{K_c}^2(1-\nu^2)}{E}. \tag{4.13}$$

Here, σ_f, K_c, ν, and E are the fracture stress, stress intensity factor, Poisson's ratio and Young's modulus. The Poisson's ratio $\nu = 0.34$, and Young's modulus $E = 110$ GPa [139], and Kumar and Misra [140] gave the specific stress intensity factor of CuZn32 as $K_c = 80\ \text{MPa} \cdot \text{m}^{-1}$. The damage shear stresses can be calculated via $t_0^s = t_0^t = t_0/2(1+\upsilon)$. All parameters used for the CZM in this research are listed in Table 4.3.

Table 4.3 Parameters used in CZM for various grain sizes.

G_C^n (MPa · mm)	G_C^s (MPa · mm)	G_C^t (MPa · mm)	
51	138	138	
d (μm)	t_0^n (MPa)	t_0^s (MPa)	t_0^t (MPa)
17.5	741	277	277
62.1	621	232	232
157.7	513	191	191

4.3.4 Modelling of uniaxial tensile test and progressive microforming process

The study utilized a series of polycrystalline RVEs and implemented them in uniaxial tension simulations using the commercial software ABAQUS. The RVEs were divided into the cell aggregates via the Voronoi tessellation method, as illustrated in Fig. 4.6. To reduce the computational time, only RVEs of the specimen gauge section used in the uniaxial tensile tests were modelled. Since the initial shapes of the grains were regenerated, the grain orientation mapping of the corresponding grains was used in this research. In such a way, the relative positions of the grains corresponding to the grain orientations were fixed, i.e. the grain orientations of the neighbouring grains

were determined according to the actual textures to ensure their compatibility. Furthermore, the grain sizes were averaged as the same as the mean sizes of corresponding samples. The RVEs were modelled with C3D8 bulk elements, and the periodic boundary conditions were applied to ensure accuracy and reliability.

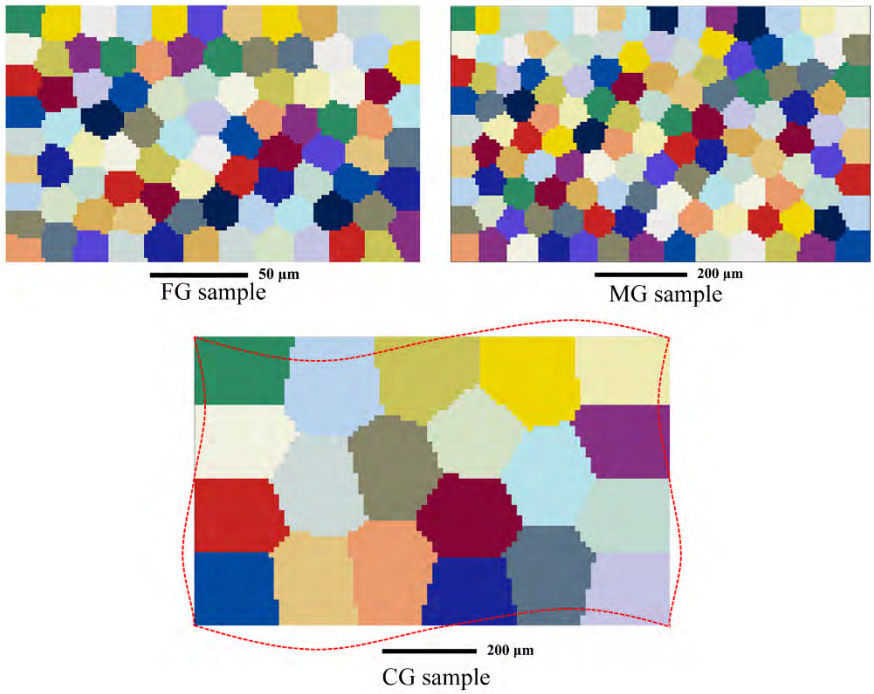

Fig. 4.6 Illustration of RVEs for various grain sizes and applied periodic boundary conditions. The RVEs were built to show the same surface as the EBSD samples with a reference direction norm to the RD-ND section. The RVE and periodic boundary condition method can reduce the computational cost without compromising the accuracy.

The progressive microforming process was modelled using both CPFEM and conventional FEM, as shown in Fig. 4.7. The simulations were performed step by step. As Step I is finished, the 1st punch will move away and the 2nd punch will move to the designated location to start Step II. The conventional FEM simulations were conducted in Deform-3D software. Considering the computational efficiency, only a

quarter of the deformed sheet was simulated under symmetric boundary conditions. As illustrated in Fig. 4.7 (b), conventional FEM does not account for microstructure details of the CuZn32 sheet. Its constitutive relationship is directly obtained from uniaxial tensile testing.

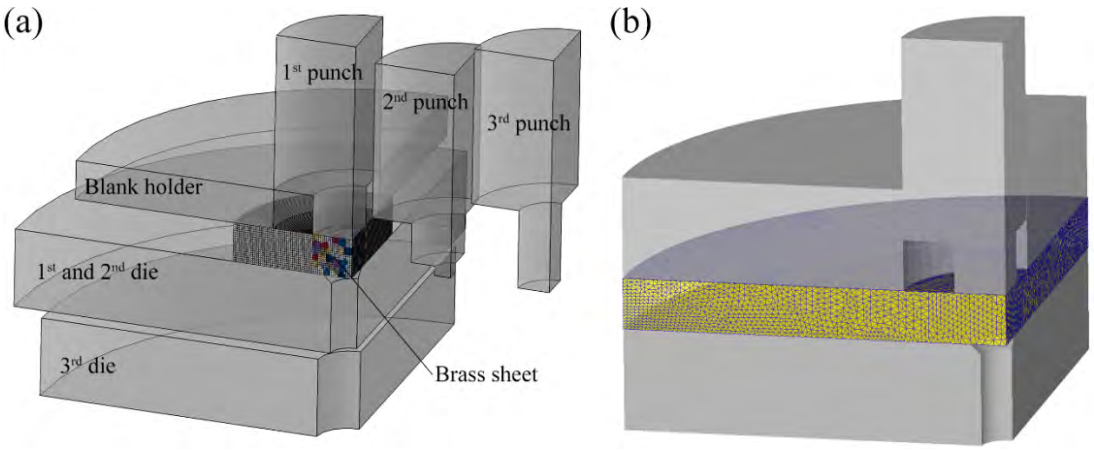

Fig. 4.7 Modelling of the progressive microforming process using (a) CPFEM and (b) conventional FEM. The simulations were conducted step by step.

For the CPFEM approach, ABAQUS software was utilized as the simulation platform. The sheet was modelled by a combination of different zones and different simplification ratios for various grain sizes. For example, the inner region of the sheet that is in direct contact with the punches and dies has a dimension of 1 mm in both radius and thickness, which was set as the crystal plasticity zone for 201 grains for the CG sample as shown in Fig. 4.7 (a). The detailed models of the inner regions of the brass sheet are illustrated in Fig. 4.8. The models of the inner regions with the grain size of 17.5 μm, 62.1 μm, and 157.7 μm were simplified into 1/360, 10/360, 90/360 based on their symmetry planes with 1650, 370, and 201 grains, respectively. CPFEM was applied to the inner region while the rest of the CuZn32 sheet followed the isotropic stress-strain relationship obtained from the uniaxial tensile tests. Constitutive behaviour in this region was defined using the CPFEM in Section 4.3.1, and the actual

texture was assigned to the materials. The models were first divided into different grains by using the Voronoi tessellation approach. Since the textures obtained by EBSD were measured in 2D, the surface grains of the RVEs were assigned with the initial grain orientation according to the same mapping method to ensure compatibility; the internal grains were then individually assigned with the grain orientations according to the layering. The experimental and simulation misorientation distribution functions (MODF) are given in Fig. 4.8. The consistency of the EBSD formation and the simulation modelling information demonstrates the feasibility of this modelling approach and the reliability of the subsequent simulation results.

It is worth noting that in the CPFEM simulation, the distribution of the cohesive elements was set as full-field. In this study, cohesive zones were established between every element within the RVEs by considering both intergranular and transgranular fractures. C3D8 and COH3D8 were assigned for the bulk elements and cohesive elements, respectively. The shear friction model ($f_s = \mu p$) with a friction coefficient of 0.12 on the lubricated tooling-workpiece interface was employed for both FEM and CPFEM simulations.

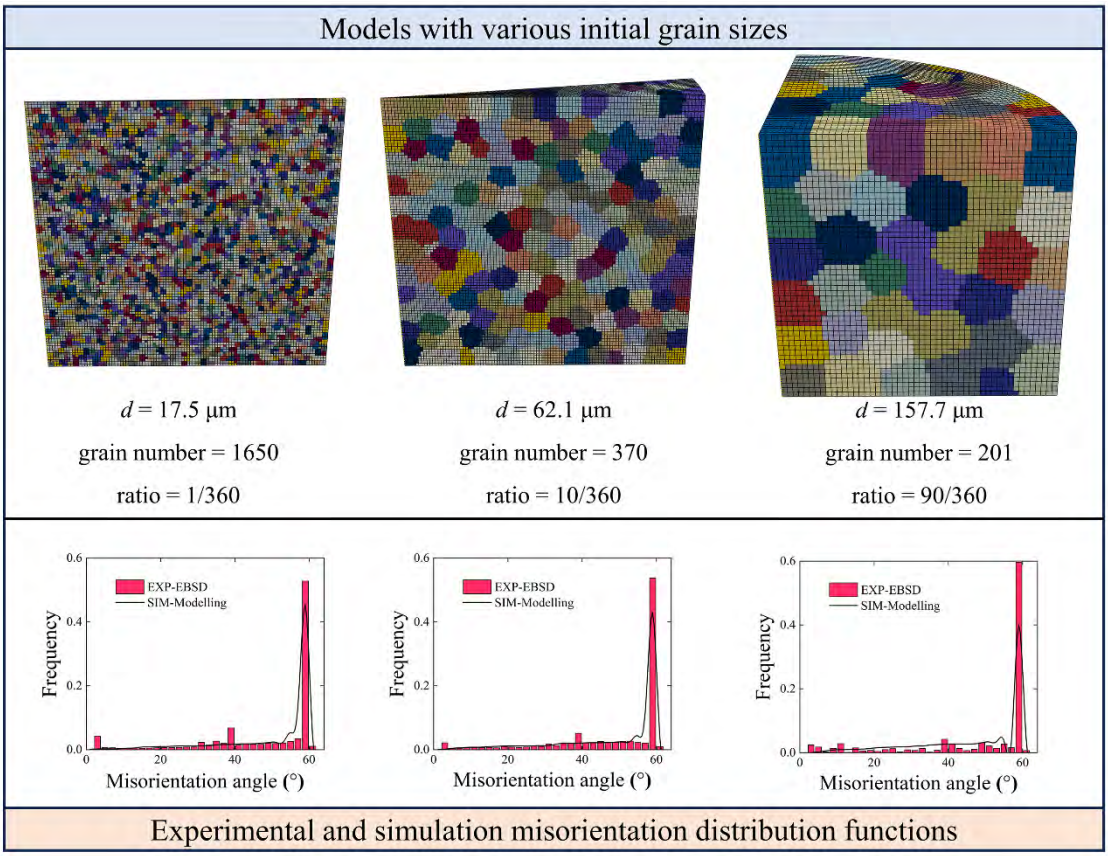

Fig. 4.8 Models for the progressive microforming CPFEM simulation with information of average gran sizes, grain number involved, and simplification ratio and experimental and simulation misorientation distribution functions (MODFs) in the models. The consistency of the MODFs in the EBSD and the simulation modelling information demonstrates the feasibility of this modelling approach and the reliability of the subsequent simulation results.

4.4 Results and discussion

4.4.1 Size effect in tensile test simulation

As depicted in Fig. 4.9 (a), the experimental results indicate that specimens with coarser grain correspond to a lower true stress response and therefore lead to lower initial yield stress due to the reduced grain boundary strengthening effect. Moreover,

the coarser-grained specimens were found to be more brittle as the fracture strain decreased with increasing grain size. In CuZn32 microstructure, deformation twinning plays a crucial role, as it is a typical FCC metallic material with low stacking fault energy [141]. In the initial stages of deformation, specimens with finer grains exhibit a higher strain hardening rate due to the severe impediment of dislocation movement at the grain boundaries. This trend does not hold when the truss stress goes beyond a threshold. As indicated in Fig. 4.9 (b), the CG specimen starts to exhibit a higher work hardening rate than the MG one when the true stress is beyond 300 MPa. Deformation twinning generates an additional hardening mechanism. The correlation between work hardening and twinning can be ascribed to three factors: (1) twinning activates the grain splitting, reduces the effective distance of dislocation slip, and facilities strain hardening by the Hall-Petch effect; (2) twinning changes the lattice orientation; and (3) twin region in a less strained matrix is harder than the adjacent non-twin region within a grain according to the Baczynski hardening mechanism [142]. Fig. 4.10 compares the true stress-strain curves for various grain sizes. A close match of simulation and experiment results was found for samples with real textures. Simulation results for the samples with random textures, which are represented by the shaded areas, tend to exhibit a larger scatter with increasing grain size. This indicates that the CPFEM can provide a good prediction of the strain-hardening behaviour in CuZn32 when the real textures are considered. Therefore, only the actual textures were utilized to model progressive microforming simulation.

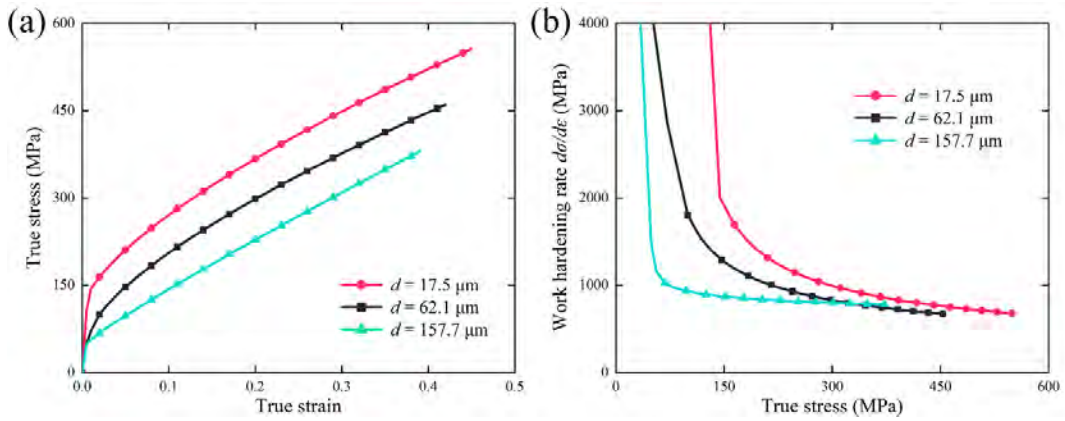

Fig. 4.9 Comparison of experimental true stress-strain curves and work hardening curves with various grain sizes.

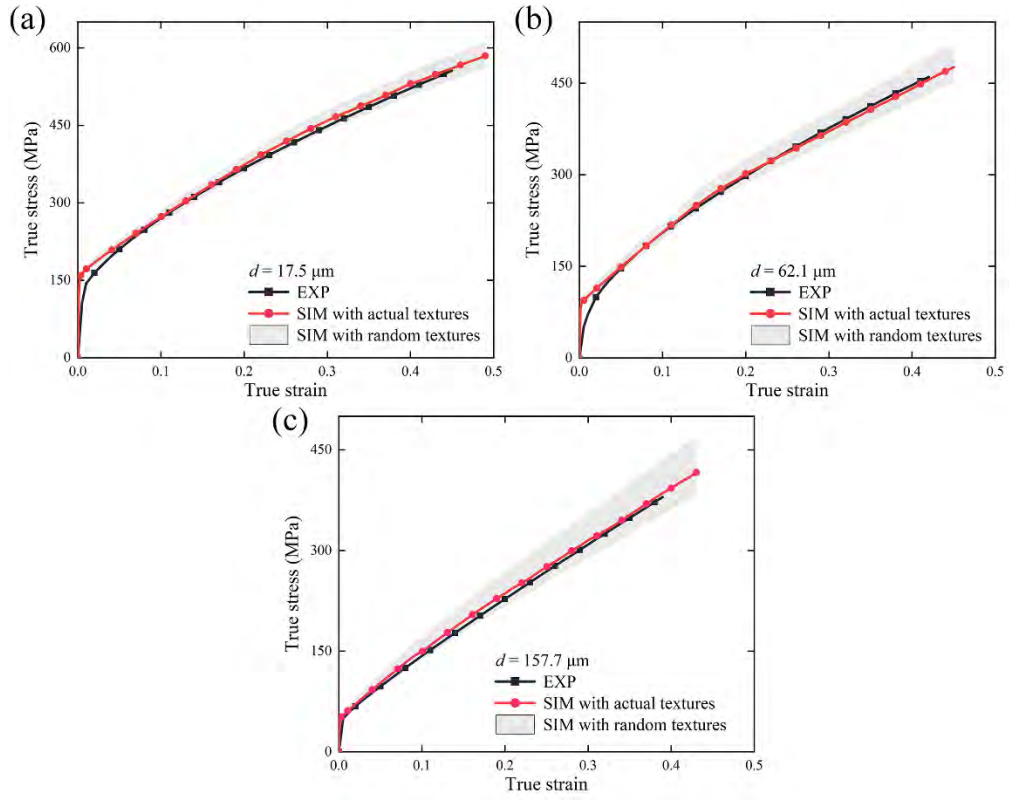

Fig. 4.10 Comparison of the simulated and experimental true stress-strain curves for (a) FG, (b) MG, and (c) CG samples. The grey areas are obtained by simulations with randomly generated textures. On the one hand, the consistency of the experimental and simulation results validates the CPFEM model and the

corresponding parameters; on the other hand, the uncertainty of the results due to the random initial textures proves the necessity of the real texture in the modelling.

The deformed microstructure and the distribution of von Mises stress resulting from the tensile test simulation are depicted in Fig. 4.11. The analysis revealed several key insights. Firstly, the Hall-Petch relations at the micro-scale hold, as evidenced by the reduction in stress as grain size increases. Upon examination of the experimental results at 0.4 strain (Fig. 4.9 (a)), the simulation and experimental results demonstrate a fracture stress ratio of approximately 1.45:1.18:1 and 1.43:1.28:1 for the three different grain sizes, respectively. This close agreement between the simulation and experimental data supports the accuracy of the proposed CPFEM approach and the corresponding parameters. Secondly, certain grains experience significantly greater deformation than others. It is found that grains experiencing higher average stress and strain tend to undergo deformation along the tensile direction and exhibit greater misorientations in relation to the surrounding grains. Lastly, stress concentration occurs more frequently around the grain boundaries of highly deformed grains due to the blocking effect of grain boundaries on dislocation motion and the consequent promotion of twin nucleation and growth in brass materials. The highest stresses are typically concentrated near grain boundaries oriented parallel to the direction of deformation.

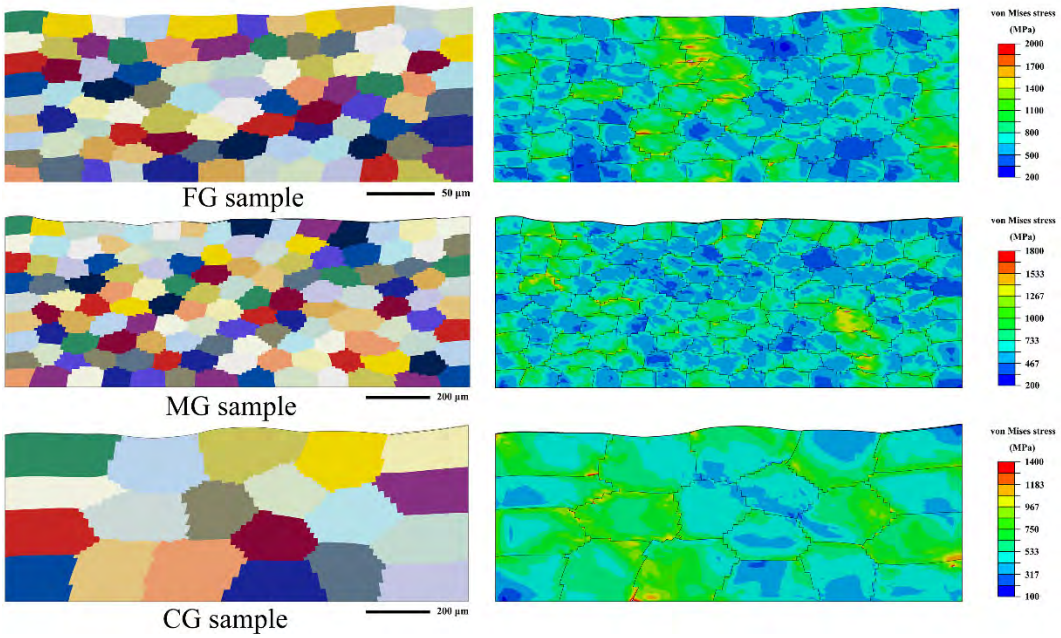

Fig. 4.11 The deformed results (strain at 0.4) of RVEs under uniaxial tension. The RVEs are modelled with actual textures for FG, MG, and CG samples, respectively. The von Mises stress mappings for each grain size are listed to show the differences.

4.4.2 Size effect on load-stroke relation

In this forming process, effective load control not only ensures product quality but also increases the longevity and cost-efficiency of the associated tooling system [143]. Especially, the maximum value of the load will have an impact on the choice of pressure equipment, holding time, and tooling materials in mass production [144, 145]. During microforming, correlations between load and stroke in hexagon socket parts with various grain sizes in the three steps are illustrated in Fig. 4.12 (a-c). In this work, the average results of three sets of repeated experiments were utilized for the load-stroke relations. Since only a part of the material was simulated, the load results of the CPFEM simulation were multiplied by the scale of the model simplification.

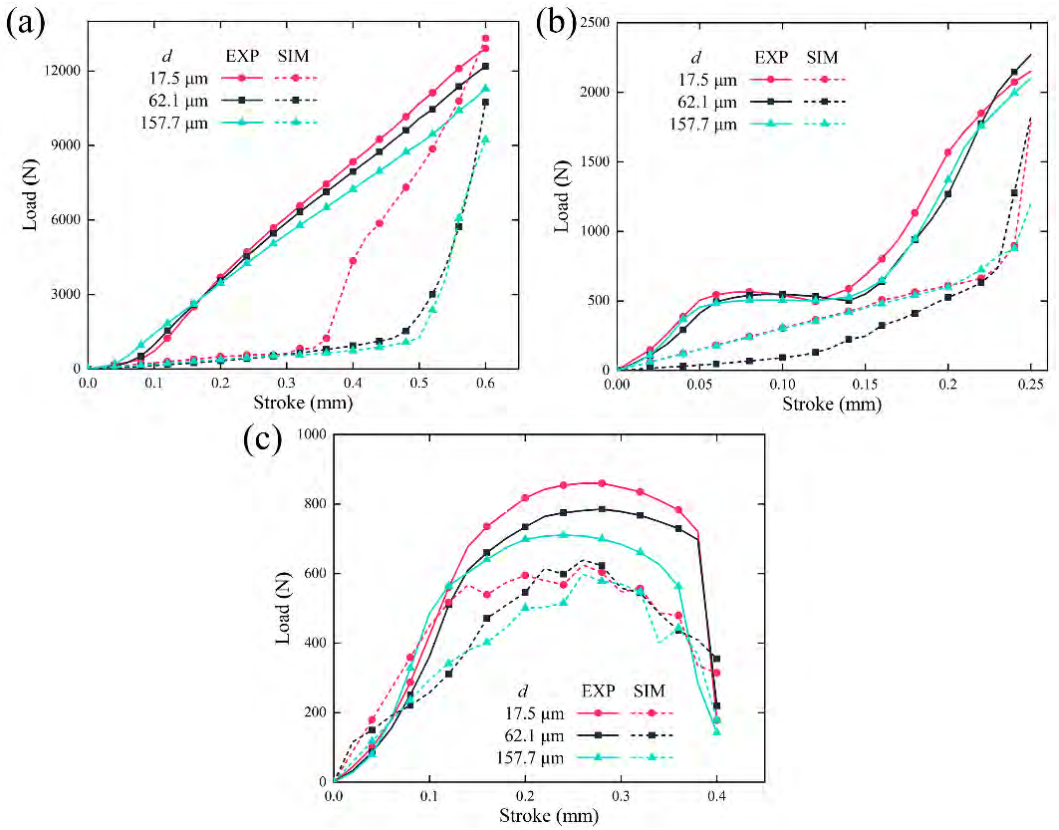

Fig. 4.12 Comparison of the load-stroke curves between CPFEM simulations and experiments with various grain sizes in (a) Step I, (b) Step II, and (c) Step III.

It can be observed from Fig. 4.12 (a) that the load in Step I is significantly greater compared to the subsequent two steps, with a difference in maximum value as much as a dozen-fold. During Step I, which involves the first forward extrusion process, the experimental results demonstrate an essentially linear increase in load with a maximum value of approximately 11,000-13,000 N. In contrast, the simulation results show slow growth and then a sharp increase only during the final 0.3 mm or 0.15 mm stage as shown in Fig. 4.12 (a). During Step II, as the forming process continues, the load is initially raised to 500 N and then maintained within this range for strokes ranging from 0.06-0.15 mm. Subsequently, the load increases linearly to a range of 2,100-2,300 N. For the simulation results, a steep increase occurs in the last 0.02 mm stroke, while the maximum load is below 2,000 N. Step III necessitates the full

extraction of the part from the die tunnel, resulting in a much greater stroke compared to the first two steps according to Fig. 4.3 (b). During Step III, specifically within the stroke range of 0.4-0.9 mm, only sliding friction between the punch and the shear-finished sheet material occurs. As a result, the load experiences fluctuations limited to the tens of Newton. Therefore, an effective stroke from 0 to 0.4 mm is enough for the analysis. As shown in Fig. 4.12 (c), the load first rises in step III and then experiences a slow increase and decrease during the continuous blanking process. After the cutting process is completed, the load abruptly drops to approximately 200 N, mainly generated by longitudinal sliding friction during the insertion of the part into the die tunnel. The maximum limit value for load in this progressive microforming system is 15,396 N, which is the sum of the individual maximum load values for each stage: 12,907 N from Step I, 2,269 N from Step II, and 220 N from Step III. The CPFEM yields a similar prediction of (13317+1828+355=) 15,500 N. This suggests that the new method can accurately predict the load limit.

The load-stroke curves exhibit various grain SEs. Firstly, the experimental results demonstrate that samples with smaller grains exhibit higher applied loads for the same stroke in every step. This trend is consistent with the conclusions in Section 4.4.1 as smaller grain size leads to increased stress. Secondly, the load for the FG sample shows an earlier steep increase compared to other grain sizes in Step I (forward extrusion), indicating a delayed occurrence of fracture. In 1972, Phillips and Armstrong [146] found that the fracture strain in brass materials (CuZn30) linearly decreased with $d^{-1/2}$. Nonetheless, this SE is much more pronounced in the simulation than in the experiment. Besides the steep rise, there are no significant differences in load between the other two larger grain sizes. Similarly, Zheng et al. [22] reported the load-stroke curves in CuZn35 flat pogo pins with larger initial grain sizes (71 and 107 μm) were the same compared to smaller grain sizes. This indicates that there exists a threshold

grain size beyond which the load-stroke response is not affected by the extrusion operation. Thirdly, at the initial stage of the experiment, the load for coarse-grained material tends to be greater but is quickly surpassed by that of fine-grained material when the stroke is less than 0.15 mm and 0.1 mm for Step I and III, respectively. This can be attributed to the difference in yield strain among different grain sizes. According to Li et al. [147], who synthesized the grain SE on yield strain for brass CuZn30 material, there is an increase in yield strain from approximately 1.95×10-3 to 2.2×10-3 when the grain size decreases from CG to FG. While fine-grained material is still undergoing elastic deformation, coarse-grained material has already entered into the plastic stage for the same stroke.

4.4.3 Size effect on product quality and deformation behaviours

4.4.3.1 Size effects on microstructure and texture evolution

Given that the microstructure evolution is closely linked to dimensional accuracy and the formation of undesirable and asymmetric geometries [148], understanding the material flow behaviour in the progressive microforming process is crucial for optimizing the process and enhancing product quality [149]. Fig. 4.13 showcases the strain maps, texture changes, and microstructure of the cross-sections, highlighting the typical inferior geometry observed in the microformed parts with different initial grain sizes. It should be noted that the effective strain ε_{eq} in the conventional FEM can be directly extracted from software, while the effective strain ε_{eq} in the CPFEM simulation needs to be calculated following the equation [150]:

$$\varepsilon_{eq} = \frac{\gamma}{\sqrt{3}} = \frac{1}{\sqrt{3}}\left[(1 - f^{tw})\sum_{\alpha}^{N^s}|\gamma^{\alpha}| + \sum_{\beta}^{N^{tw}}\left|\gamma^{\beta}\right|\right]. \tag{4.14}$$

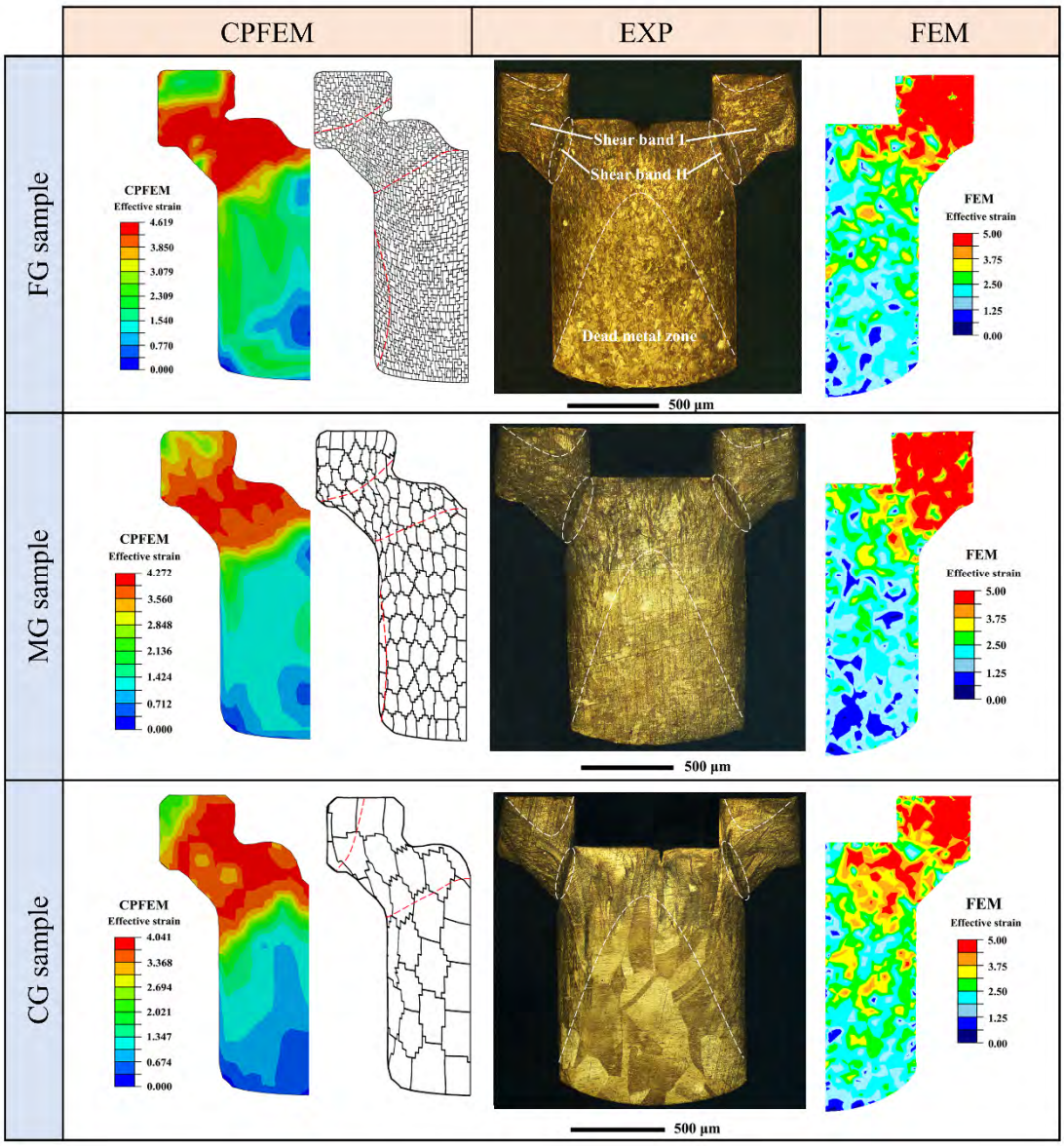

Fig. 4.13 Comparison of the experimental, CPFEM, and FEM simulated effective strain maps, texture, and microstructure changes of the cross-sections of the formed parts for FG, MG, and CG samples, respectively. The effective strain mapping based on the CPFEM simulation results is calculated using Eqn. 4.14. The metallographic images of the cross-section of the parts indicate the important material flow behaviour and microstructure evolution.

The microstructural examination of the cross-sections of the resulting component

reveals the presence of two prominent shear bands in which the material has undergone pronounced plastic deformation and flow, as shown in Fig. 4.13. Shear band I, which covers most of the head feature, was formed during the extrusion process in Step I and then continues to develop in Step II. This shear band also governs the material flow in the upper portion of the body. A gradual increase in the material flow line density becomes apparent when observing from the middle region of the head downwards. Shear band II, which was generated during the second operation, exhibits a higher flow line density in comparison to Shear band I. Shear band II appears as a series of lines of tens of micrometres, linking the bottom corner of the hexagonal socket feature to the junction between the shoulder and body portions. Regions with intense material flow, such as the shear bands, are more accurately predicted via the strain maps in CPFEM simulations than the conventional FEM. Elevated strain accumulations were observed in these regions, as illustrated in Fig. 4.13. However, the conventional FEM fails to maintain the continuity of strain distribution, resulting in a disjointed and unrealistic strain pattern. In addition to the aforementioned shear band regions, three dead metal zones were identified, located at the summit of both head regions, as well as the middle and lower portions of the body feature.

Dead metal zones are characterized by a lack of material flow, with these three dead metal zones demarcated based on the extent of grain deformation, flow lines, and comparatively lower levels of strain accumulation as illustrated in Fig. 4.13. A comparison of the microstructures and flow patterns of the manufactured product with varying initial grain sizes reveals that the area occupied by shear bands decreases as the grain size increases, which contradicts the findings of Zheng et al. [22]. These shear bands and dead metal zones can also be roughly inferred from the texture of the CPFEM simulation results. The grains located in the shear band region underwent a large deformation, whereas the grains in the dead metal zones maintained their original

shape. It should be noted that the CPFEM simulation did not accurately capture two areas of material damage, namely the crack in the middle of the top and the ring-shaped necking at the junction of the shoulder and body. This demonstrates the limitations of this method.

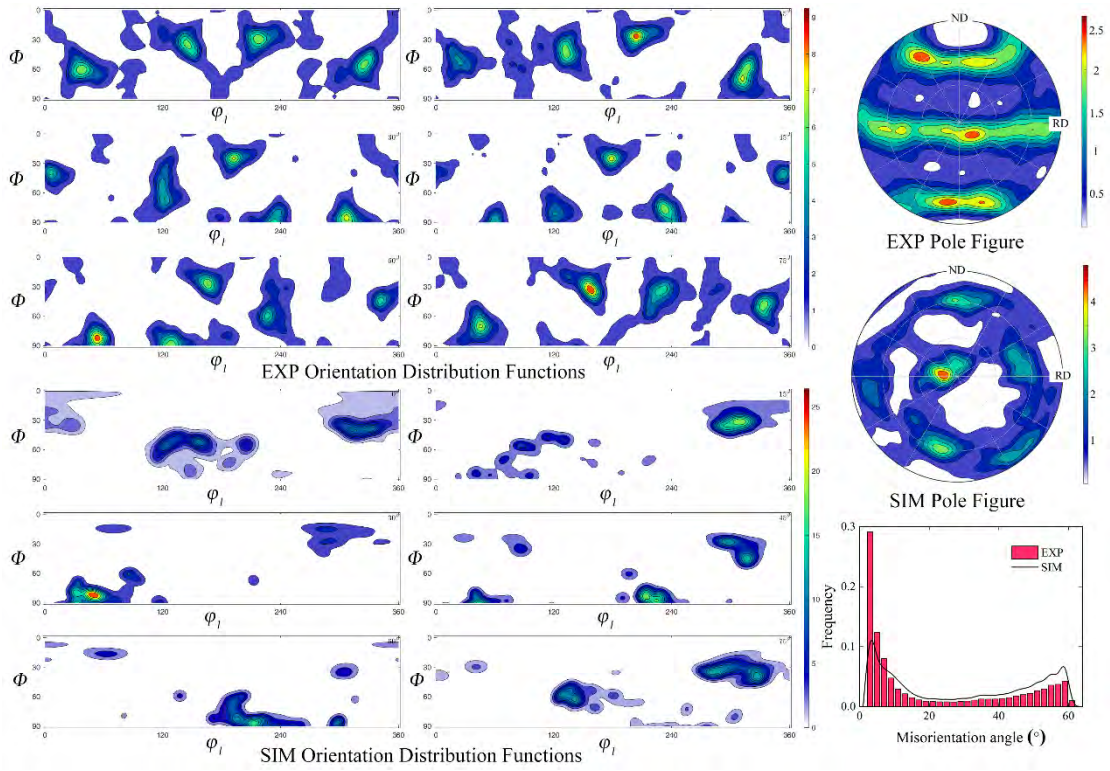

Fig. 4.14 Comparison of the experimental and CPFEM simulation orientation distribution functions, pole figures, and misorientation distribution functions of the FG sample.

To further validate the reliability of this CPFEM simulation, the comparisons of the experimental and CPFEM simulation orientation distribution functions (ODF), pole figures (PF), and MODF are given in Figs. 4.14-4.16 for FG, MG, and CG samples, respectively. Combining the ODFs and the PFs, the relative consistency of the orientation distributions in the experimental and simulation results can be observed and is particularly evident for FG and MG samples. However, the crystal orientations

show higher degree of concentration in the simulations. The difference is because the number of grains involved in the simulation is less than that in the experiment. The overall changes in the textures were very dramatic because of the complexity of the process when comparing the initial texture (Fig. 4.2) and the deformed texture (Figs. 4.14-4.16). After two extrusion and one blanking operations, the preference for anisotropic texture can be observed for the FG and MG cases, as shown in Fig. 4.14 and Fig. 4.15, which is very similar to the compressed α-brass texture [130]. In contrast, the CG sample shows a more isotropic texture, in which the maximum density reaches 9.87 and the maximum values for FG and MG samples are only 5.62 and 6.05 in the PFs. This indicates that the grain size plays an important role in the texture evolution. In the head and body of the product, the interactions among grains during deformation, particularly between surface and internal grains, are minimal with the presence of coarse grains. Considering the dead metal zones in the middle of the body feature, for instance; the grains in this zone experienced minimal deformation but exhibited pronounced rotating. For the CG material, the tilting of these grains is more diversified, whereas for the FG and MG materials, the deformation tends to follow a specific pattern.

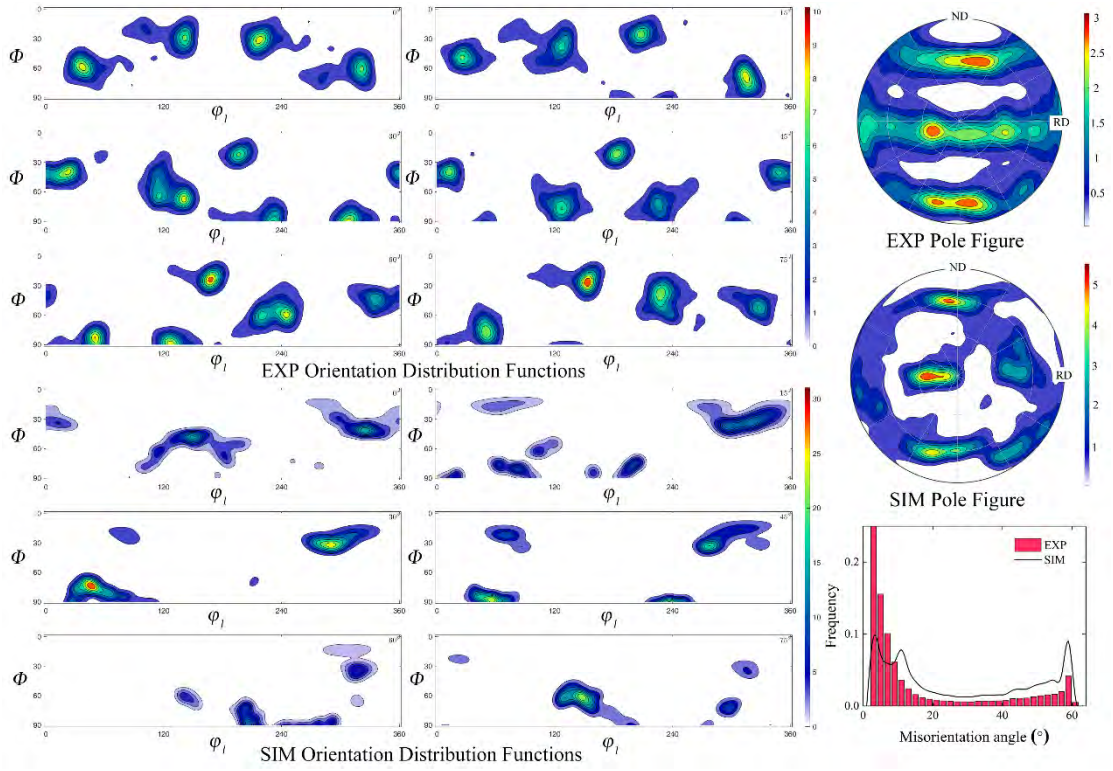

Fig. 4.15 Comparison of the experimental and CPFEM simulation orientation distribution functions, pole figures, and misorientation distribution functions of the MG sample.

In addition, there is a partial agreement and variability between the resulted experimental and simulation MODFs. Comparing the initial and resultant MODFs (Fig. 4.8 and Figs. 4.14-4.16), the proportion of misorientations around 60 degrees is greatly reduced, while the fraction of low-angle grain boundaries (LAGBs) grows dramatically. The increase in LAGBs is very common during compression [151]. However, the ratio of LAGBs in the simulation results is not as high as in the experimental results because a large amount of grain fragmentation and sub-grain boundaries were produced in physical experiments. In summary, the reliability and validity of this CPFEM simulation method can be verified by comparing and analyzing the ODFs, PFs, and MODFs in the experimental and simulation results.

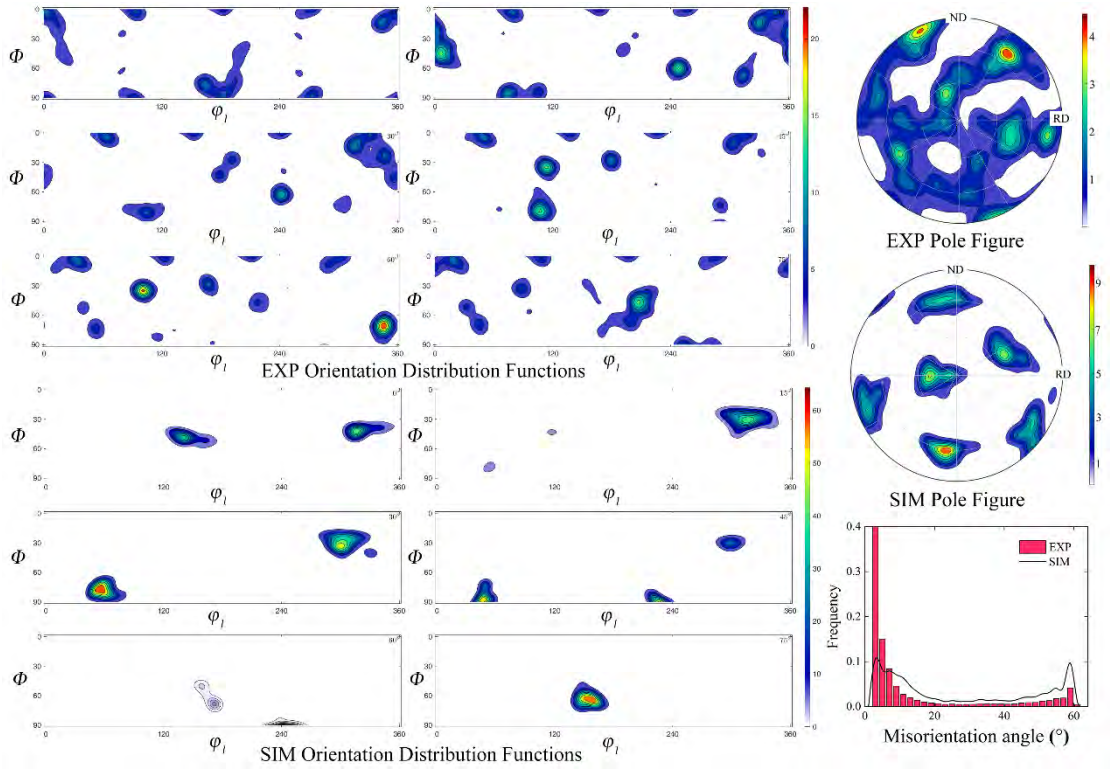

Fig. 4.16 Comparison of the experimental and CPFEM simulation orientation distribution functions, pole figures, and misorientation distribution functions of the CG sample.

4.4.3.2 Size effects on dimensional accuracy

The material anisotropy arising from the microstructure and texture leads to inhomogeneous deformation, which becomes increasingly pronounced with the grain size [152]. To determine and compare the SEs on dimensional accuracy, the height and diameter distributions of key features of the hexagonal socket part were examined, as depicted in Fig. 4.17. The part was divided into head, shoulder, body, and rollover features from top to bottom (Fig. 4.17 (a)). Firstly, the heights of each feature were collected from the SEM results and cross-section images, as shown in Fig. 4.17 (b). Based on the data, two grain SEs can be summarized: (a) the scatter of every feature height increases with grain size; (b) except for rollover, the heights of all features

decrease with the increasing grain size. These observations are consistent with the conclusions of prior research by Tang et al. [23]. Based on the microstructure and texture evolution shown in Figs. 4.13-4.16, the grain orientations gradually concentrate to several specific directions according to the pole figures. For the finer-grained and medium-grained materials, the concentration of crystal orientations is higher, resulting in more radial material flow and higher heights of the product. The design dimension for the total height of the part was set as 1.7 mm. During testing, the actual measurement error was found to be $\pm$ 0.02 mm, which falls within the acceptable limit. Secondly, the head and body diameters were evaluated experimentally and showed different levels of scattering (Fig. 4.17 (c-d)). The locations of each measuring points can be seen in Fig. 4.17(a). The head diameter distribution displayed a gradual rising trend from top to bottom. The measured error was found to be substantial when compared to the design dimension of 1.6 mm due to irregular material fracture in the upper region. Thirdly, the body diameter showed an initial increase followed by a gradual decrease with a slight increase at the junction with the rollover feature. The design dimension for the body diameter is 1 mm, and the results are deemed acceptable only for the FG case since the dimension differences reach 4% and 8% for MG and CG samples, respectively. The abrupt change in diameter at the topmost measuring point is a consequence of necking that occurs during the second step of the process.

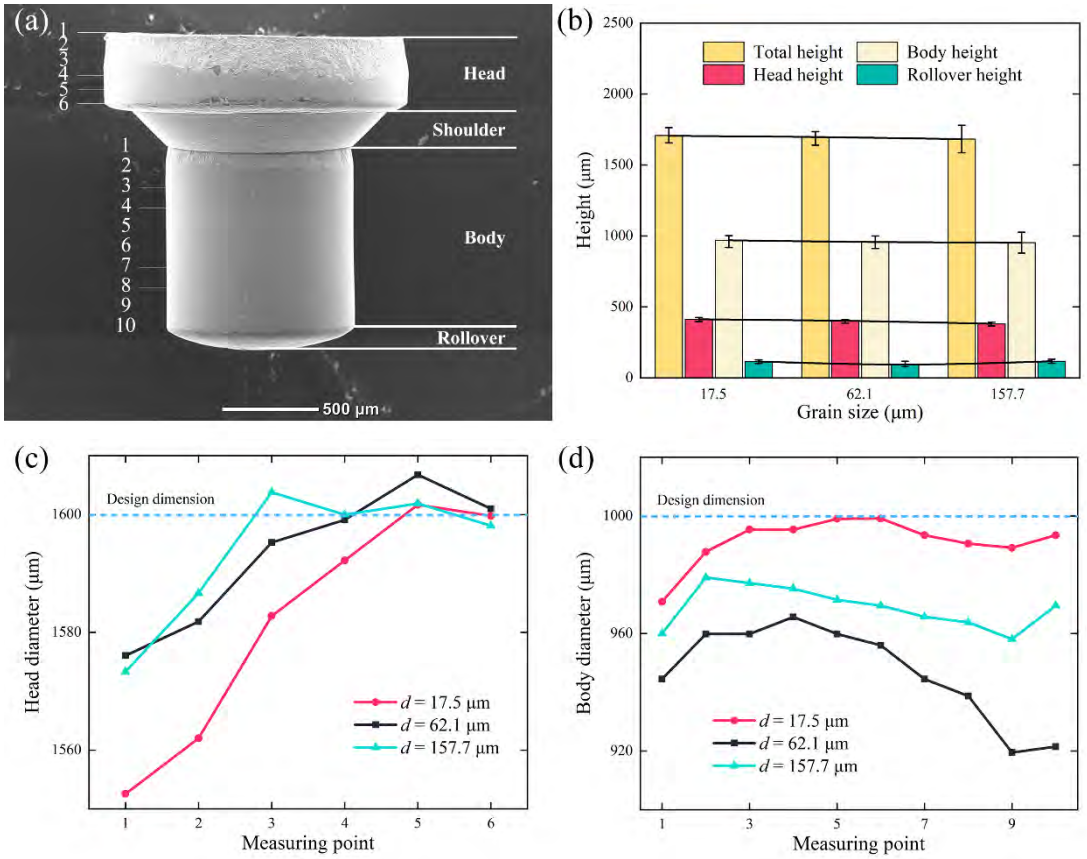

Fig. 4.17 (a) The SEM image of the fabricated part indicates several features: head, shoulder, body, and rollover. (b) The average values and errors of the heights of these features for each grain size. (c) The head diameter measurements from top to bottom with the design dimension of 1600 μm for each grain size. (d) The body diameter measurements from top to bottom with the design dimension of 1000 μm for each grain size.

Fig. 4.18 provides a comparative analysis of feature dimensions in both experiments and simulations with varying grain sizes. The simulation results directly determine heights, as demonstrated in Fig.13, while the diameters are twice the values mentioned earlier. Due to the lack of distinct boundaries between the body and rollover features in the simulation results, their heights were integrated for analytical purposes. As shown in Fig. 4.18 (a), major differences in overall height arise from variations in the

body and rollover dimensions, while the head heights remain consistent. The inclusion of burr geometry, which was not considered in the simulation results, significantly contributes to overall height. The simulation results exhibit a slight underestimation of the experimental height, and this discrepancy becomes more pronounced for coarser-grained materials. This discrepancy can be attributed to an increase in transverse material flow and a decrease in extrudate height caused by the presence of coarse grains. In the case of a limited number of grains in the direction of sheet thickness, the presence of grain inhomogeneity results in unfavourable material flow directions that deviate from the intended punching direction. As depicted in Fig. 4.18 (b), the simulation results indicate a decrease in head diameters with the rising grain size. The middle region of the head demonstrates minimal deviation from the experimental results, while the ends show significant decreases. In contrast to the head diameters, the simulation results do not reveal significant grain SEs on the body diameter distributions. However, the experimental results show a decrease followed by an increase in the body diameter with grain size (Fig. 4.18 (c)). Interfacial friction, despite the use of identical machine oil as a lubricant, is also considered a contributing factor to grain SEs. In summary, the dimensional accuracy of the CPFEM predictions is satisfactory, with corresponding grain SEs being adequately reflected. However, Fig. 4.13 further highlights the shortcomings of the conventional FEM simulations in predicting the total heights, with an error of 0.1 mm and a slight overestimation of the rollover feature height.

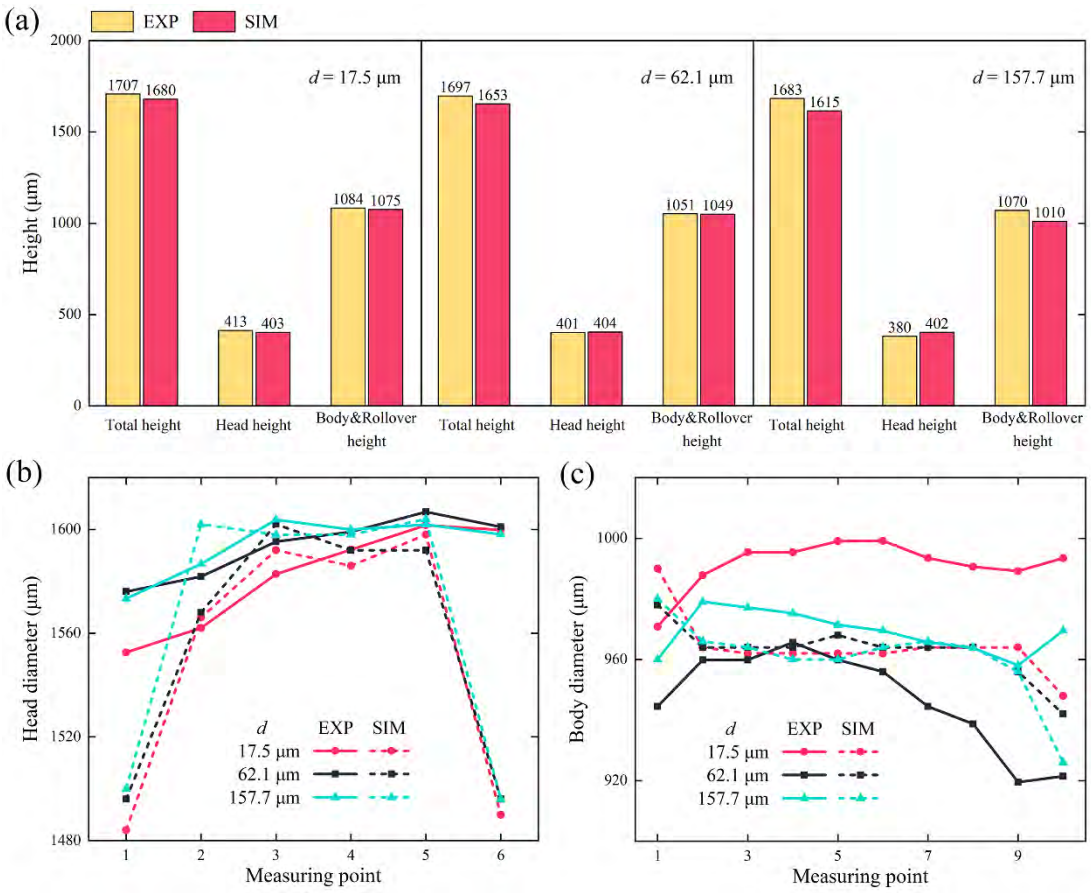

Fig. 4.18 The comparison of the important feature sizes in simulation and experiment results. (a) The heights of the head, body, and rollover, and whole part for different grain sizes are collected and compared. (b)-(c) The assembly dimensions, that is, the diameters of the head and body features, are measured from top to bottom and compared.

4.4.3.3 Size effects on surface roughness

To study the grain SEs on surface roughening, the morphology of the surfaces on the hexagon socket part was observed by SEM, and the surface roughness was measured by using a 3D laser scanning microscope. Fig. 4.20 shows the measuring location and results of the roughness. The side surfaces of the head and body features were selected as the measurement locations, which were first tilted by an accompanying software to

transform them into a plane. The roughness R_a was calculated by Eqn. 3.8.

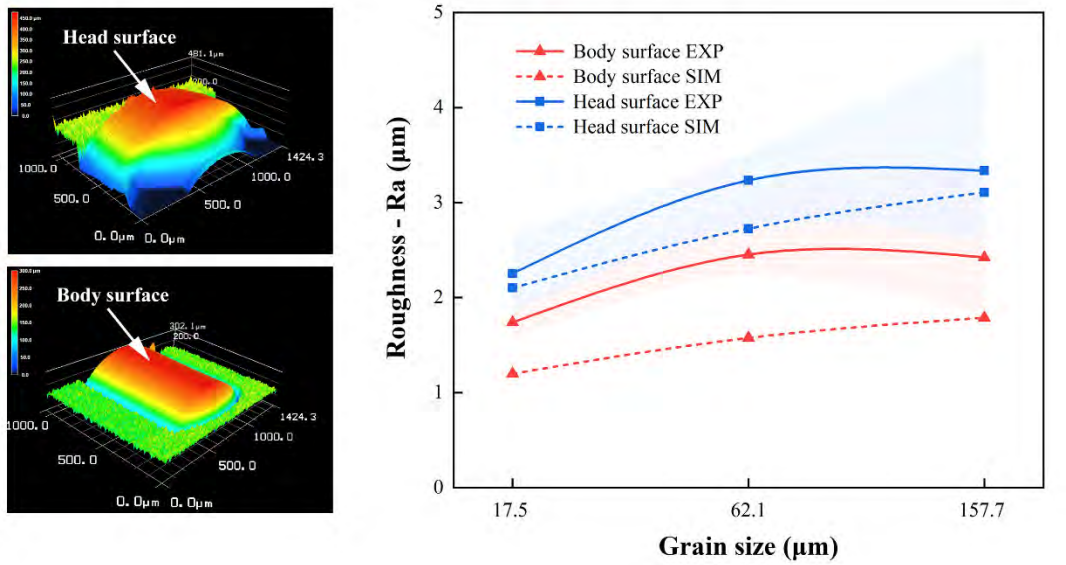

Fig. 4.20 The surface roughness measurement mappings of the head and body surfaces. The simulation results are calculated via Eqn. 3.8, and the shaded areas represent the calculation errors in simulation results. Then the surface roughness in experimental and simulated results are drawn and compared.

Fig. 4.20 demonstrates the disparity in roughness between the head surface and the body surface, which is primarily attributed to the different mechanisms. The head surface is characterized by the formation of a blanking shear band, as opposed to the friction shear band that constitutes the body surface. In contrast, the body surface exhibits a notably smooth appearance, with minimal irregularities, except for the occurrence of a few sporadic longitudinal fine lines. These fine lines can be attributed to the relative sliding between the material and the die during the manufacturing process. It is also observed that the surface roughness is positively correlated with the grain size. The trend mentioned above is evident in the results obtained from the CPFEM simulations, albeit with magnitudes smaller in comparison to the experimental findings. The anisotropy of the grains induces incompatible strains

within neighbouring grains, leading to a scenario where certain grains undergo vertical deformation while others deform in different orientations. This phenomenon ultimately gives rise to a rough surface. As the grain size increases, the surface grains are subjected to lower constraints, leading to more severe incompatible deformation of those grains and a corresponding increase in surface roughness. The error in the simulation results (shaded area) also increases with the grain size for the same reason. Moreover, the surface roughness is intricately related to the lubrication conditions. For a given sheet thickness, when the grain size increases, it leads to a reduction in the presence of lubrication pockets, resulting in an increase in friction and surface roughness [153]. In conclusion, the roughness of the formed part is significant, and the performance of the fine-grained materials is comparatively superior. Efforts towards improving the product surface quality, such as further surface treatment of the tooling and optimized lubrication conditions, are imperative.

4.4 Summary

To develop an integrated meso/micro-scaled progressive forming system combining product design, process analysis, and CPFEM simulation, and utilize it to investigate the interplay between scale-dependent deformation behavior, size effect mechanisms, and final part quality. A novel CPFEM and CZM method was developed to investigate the deformation and failure behaviours induced by grain SEs in uniaxial tensile tests and progressive microforming in this chapter. A three-step progressive microforming process was designed and implemented as a case study for the production of a hexagonal socket part, to evaluate the effect of grain size on the stress and strain distribution, microstructure evolution, load-stroke relations, dimensional accuracy, irregular geometries, and surface quality. The following conclusions were reached:

1) Due to the complexities of the progressive microforming, a new CPFE-CZM method was proposed for simulation and prediction: the CPFE model incorporates the effects of slip and twinning on deformation behaviour in brass materials, while the CZM considers the distribution of cohesive elements for different processes through the adoption of the bi-linear TSL and MAXS criterion. The RVEs with the actual textures of CuZn32 material with various grain sizes were simulated using this method and validated by uniaxial tensile tests; the results are in good agreement in terms of the mechanical response of the material.

2) The CPFE-CZM simulations were compared with experiments and conventional FEM simulations, demonstrating the superiority of the CPFE-CZM method over conventional FEM in predicting experimental outcomes. The results showed that the CPFE-CZM method could accurately anticipate the trend of decreasing forming load with increasing grain size, as well as the approximate range of maximum load. The CPFE-CZM method was able to provide consistent results with experiments in terms of part dimensional accuracy, with the total height being negatively correlated with grain size and the head diameter rising with grain size. Overall, the part with the initial fine-grained material has the best fit with the design scenarios in terms of its size.

3) The microstructure evolution during progressive microforming was revealed through the observation of shear bands and dead metal zones, which could be accurately predicted by strain maps from CPFE-CZM simulations, with dead metal zones becoming larger with coarser grains. The surface defects, including dimples, micro pits, and micro wrinkles, were found to be more prominent in coarser-grained materials, difficult to directly determine from the CPFE-CZM simulation results, and can only be inferred from the measured surface

roughness. This shows the limitations of this novel method.

In conclusion, the CPFE-CZM method provides a robust approach for the simulation and prediction of complex meso/microforming processes that involve shearing and plastic deformation. The methodology holds promise for the refinement of constitutive models and fracture models for different materials, processes, and products in future studies. However, this method also brings many problems, such as extremely high computational costs. Next, we will continue to explore the advantages and disadvantages of CPFEM in meso/microforming in depth.

Chapter 5 Deployment and Assessment of the CPFEM Framework for Complex Progressive Meso-Forming: Predictive Capability for Deformation, Failure, and Part Quality under Size Effects and Comparative Analysis with Conventional FEM

5.1 Introduction

While CPFEM has shown considerable advantages over traditional FEM in the forming processes of complex meso/micro-scaled parts, especially in capturing detailed material behaviours and deformation mechanisms, it still encounters significant challenges. These include extremely high computational costs and complex modelling processes, which limit its practical usability. To address these issues and provide a comprehensive understanding of CPFEM's capabilities, this chapter aims to conduct a thorough comparison and analysis of CPFEM with other commonly used advanced simulation methods. By evaluating their respective strengths and weaknesses, this study will offer valuable insights for selecting the most appropriate simulation technique for complex progressive meso/microforming processes and identify potential areas for future improvements.

In this chapter, an advanced simulation technique, the coupled Eulerian-Lagrangian (CEL) method, was introduced for the first time to model the progressive meso-forming of complex components. This approach was used to compare the strengths and limitations of CPFEM, conventional FEM, and CEL in addressing SEs induced during the forming process. A novel experimental forming system was specifically

designed and developed to fabricate a meso-scaled gear shaft, thereby validating the simulations. This research assessed the impact of SEs on computational efficiency, process load control, feature size accuracy, microstructural and texture evolution, and product surface quality of progressive meso-formed parts by comparing CPFEM, CEL, FEM, and physical experiments. Furthermore, the mechanisms of SEs in the progressive meso-forming of polycrystalline materials were elucidated, and the SE on extrudate length was explained and validated. As a result, this study marks a notable advancement in the development of precise and computationally efficient techniques for forming complex components.

The concept of the CEL can be encapsulated by setting up a Lagrangian mesh for die and a Eulerian region for deforming material, thereby, to some extent, circumventing the task of meshing the material at the initial stage [154-156]. As depicted in Fig. 5.1, Lagrangian mesh conforms to the shape of material, with the material points moving synchronously; in contrast, the Eulerian mesh is stationary, considering only the flow of fluid through it, with the volume fraction within each element used for description. Compared to FEM and CPFEM, the CEL offers numerous advantages. On one hand, by eliminating distorted elements and thus avoiding the need for remeshing, CEL significantly reduces the time required for simulation setup and execution. On the other hand, CEL enables the use of straightforward material models like the Swift [157] and Johnson-Cook models [158], which are much less complex than those used in CPFEM. The CEL has been successfully applied in various metalworking domains, including friction stir welding [159, 160], orthogonal cutting [161, 162], cold spray [163], and end milling [164]. For forming purposes, Al-Athel and Gadala [165] conducted wire drawing simulations using CEL, in which the wire was regarded as an Eulerian grid. Hah and Youn [166], Liu et al. [167], and Asadi and Akbari [168] all successively applied the method to back extrusion, sheet drawing, and friction stir

back extrusion, respectively. These applications underscore the potential of CEL in addressing the challenges faced by FEM and in the manufacturing of complex-shaped parts.

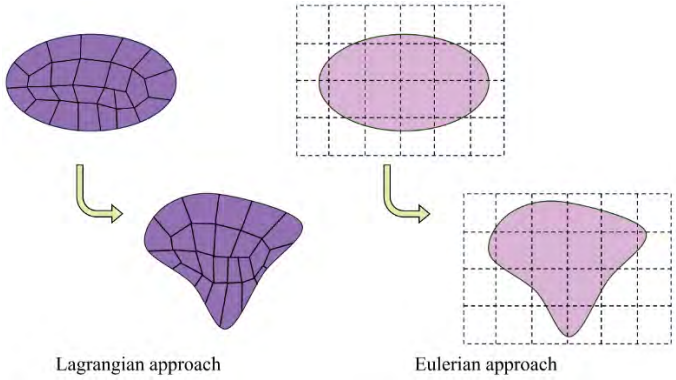

Fig. 5.1 Schematic of Lagrangian and Eulerian approaches in ABAQUS/Explicit. The Lagrangian mesh follows the part shape and the material points move as a single entity; the Eulerian mesh remains fixed, with material flowing through the meshed elements and represented by the volume fraction within each element.

5.2 Experimental methodology

5.2.1 Grain size analysis and property evaluation

In this study, recrystallization-annealed T2 pure copper sheets, each with a thickness of 2 mm, were utilised. To investigate grain SEs, heat treatments of 400℃-1h, 500℃-1h, and 600℃-1h were carried out with argon protection. A variety of grain sizes were ascertained and documented via microscopic analysis conducted on the surface aligned with the rolling-normal direction (RD-ND), as shown in Fig. 5.2. For the purposes of this investigation, pure copper sheets featuring average grain sizes of 23 ± 2 μm (designated as fine grain - FG), 35 ± 4 μm (medium grain - MG), and 59 ± 8 μm (coarse grain - CG) were used and subsequently subjected to both uniaxial tensile

testing and a progressive forming regime.

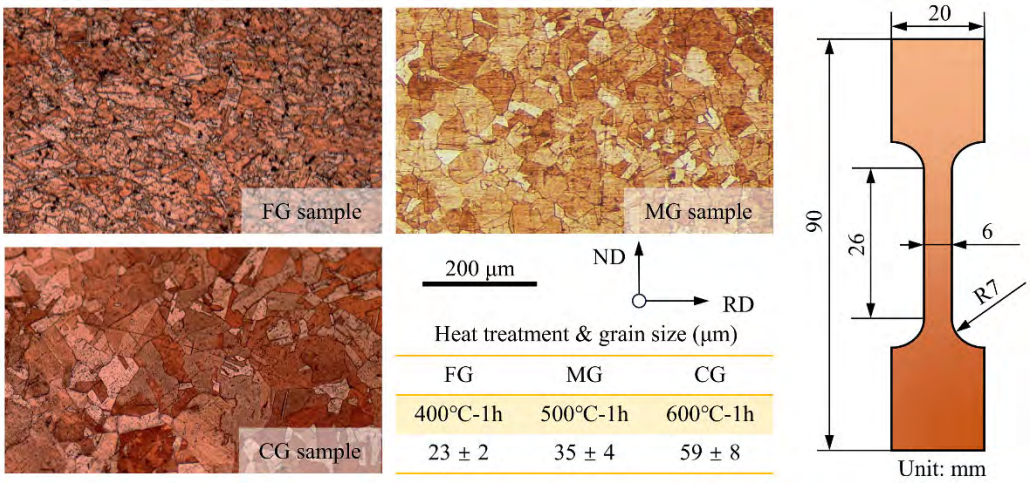

Fig. 5.2 Microstructures of the pure copper sheet after heat treatments and sample dimensions for uniaxial tensile test. The average grain sizes were obtained as 23, 35, and 59 μm under recrystallization annealing of 400˚C-1h, 500˚C-1h, and 600˚C-1h.

The mechanical properties were determined through uniaxial tensile tests, conducted in accordance with the ISO 6892-1 standard, to assess the influence of grain size on material behaviour. The material properties derived from these tests were subsequently incorporated into FEM and CEL simulations. Input parameters such as elastic properties, yield strength, and strain hardening behaviour, which dictate the material's stress-strain response under load, are essential for modelling. Fig. 5.2 depicts a tensile testing specimen with a gauge length of 26 mm, extracted from a pure copper sheet and aligned for elongation along RD. The specimens were tested using an MTS machine under quasistatic loading conditions (0.001 s^{-1} strain rate). Three independent testing repetitions of each type of specimen were considered for data reliability. The experimentally measured stress-strain curve is fitted into the Swift constitutive model described by the following equation

$$\sigma = K(\varepsilon_0+\varepsilon_p)^n. \tag{5.1}$$

Here σ, K, and n represent the flow stress, the hardening coefficient, and the strain hardening index, respectively. The fitted curves were plotted alongside the experimental results, as illustrated in Fig. 5.3.

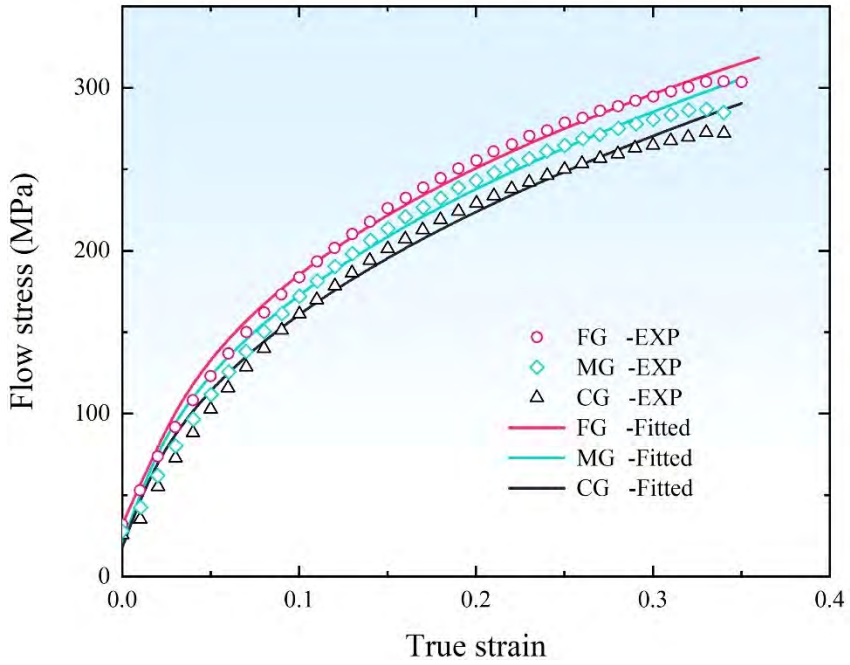

Fig. 5.3 Experimental flow stress-true strain curves and Swift model based fitted curves for FG, MG, and CG specimens. The experimental results were obtained by averaging three repeated tests.

5.2.2 Progressive meso-forming system

A set of new equipment was designed, fabricated, and integrated for progressive meso-forming including a control system, pressure system, and tooling components, as shown in Fig. 5.4 (a). The control box can be personalized regarding punch speed, punch stroke, holding time, counter speed, and counter stroke. For the pressure system, a hydraulic electric cylinder is a type of mechanical actuator used to force through a unidirectional stroke. Secured by means of bolts and guide posts, the hydraulic cylinder takes the full load-bearing strength of the tooling system. The tooling system

consists of a platform, punch holder, blank holder, die, and feeding system, as depicted in Fig. 5.4 (b). All surfaces in the tooling assembly that may come into contact with the material were controlled to a roughness of Ra 0.8. The hydraulic system's cylinder tube is positioned above the platform, with the piston rod linked to the punch holder, enabling the control system to manage the punch's ascending and descending trajectories. In this setup, the punches (blue parts) and dies (green parts) are swappable to maintain versatility for other studies and parts. The sheet metal is held by the blank holder and die in the forming processes and does not move or tilt due to excessive loads. It is worth mentioning that the newly designed feeding system is simple but function able, the rail inside is directly connected with the fixture of the sheet metal, a helical micrometer is used to measure and feed distance. Once the first step is complete, the strip will be manually lifted and adjusted. Then, the strip can be fed by using a helical micrometer for a fixed distance. This will enable accurate processing.

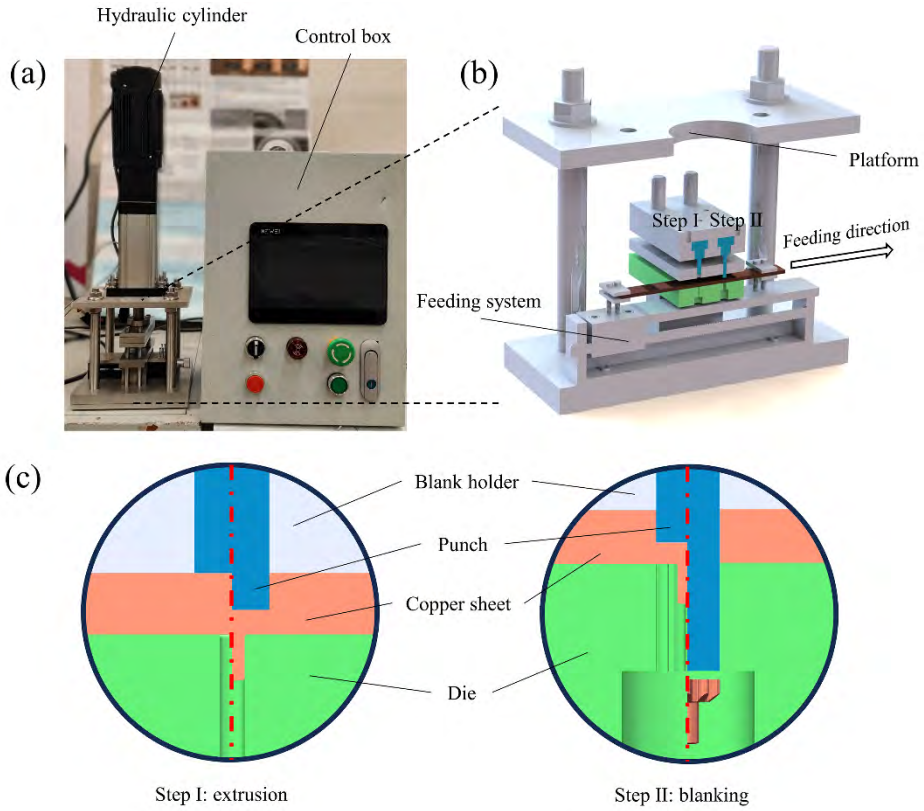

Fig. 5.4 (a) The progressive forming system consists of a control box, a hydraulic cylinder, and tooling system. The control system allows for user-defined punch speed, punch stroke, hold time, reset speed and reset stroke. (b) The tooling system consists of a two-step working system and other components. (c) Schematic diagram of each step: Step I - forward extrusion and Step II – blanking.

A pure copper gear shaft (m2-z10) was chosen as the case study in this research. Gears are fundamental mechanical components crucial for transmitting motion and/or power across various industries, and there is no doubt that gear manufacturing is a fundamental process in manufacturing engineering [169]. There are three systematic classifications that can be used for traditional methods of fabrication of gears: (a) material removal processes like hobbing and milling; (b) additive manufacturing; and (c) forming process like stamping and extrusion [170]. Manufacturing of gear shafts is often subjugated to multiple processes or high-temperature conditions; however, progressive cold forming is a very efficient option, and it exhibits excellent quality. In this study, a two-step progressive meso-forming process for gear shafts was developed, as illustrated in Fig. 5.4 (c) and Fig. 5.5 (a). A pure copper sheet (length: 80mm; width: 20 mm; thickness: 2 mm) was incrementally fed through the system along a left to right direction, with each advancement of the material representing a stage of 16 mm. The preliminary step, labelled as Step I, was performed using a 2.4 mm-diameter punch. A similar punch was employed to displace the copper material by 1.2 mm in the thickness direction, extruding it into a tunnel with a 0.8 mm diameter and a 0.1 mm radius corner. Advancing to Step II, a punch inherently matching the upper surface design of the gear shaft was used to complete part separation from the sheet. This procedure ensures the final component produced met the design specifications. To ensure procedural consistency, the forming speed in both process steps was strictly maintained at 0.005 mm/s. Every potential contact surface uses machine oil as a

lubricant to reduce friction. The fabricated gear shafts with different initial grain sizes are displayed in Fig. 5.5 (b).

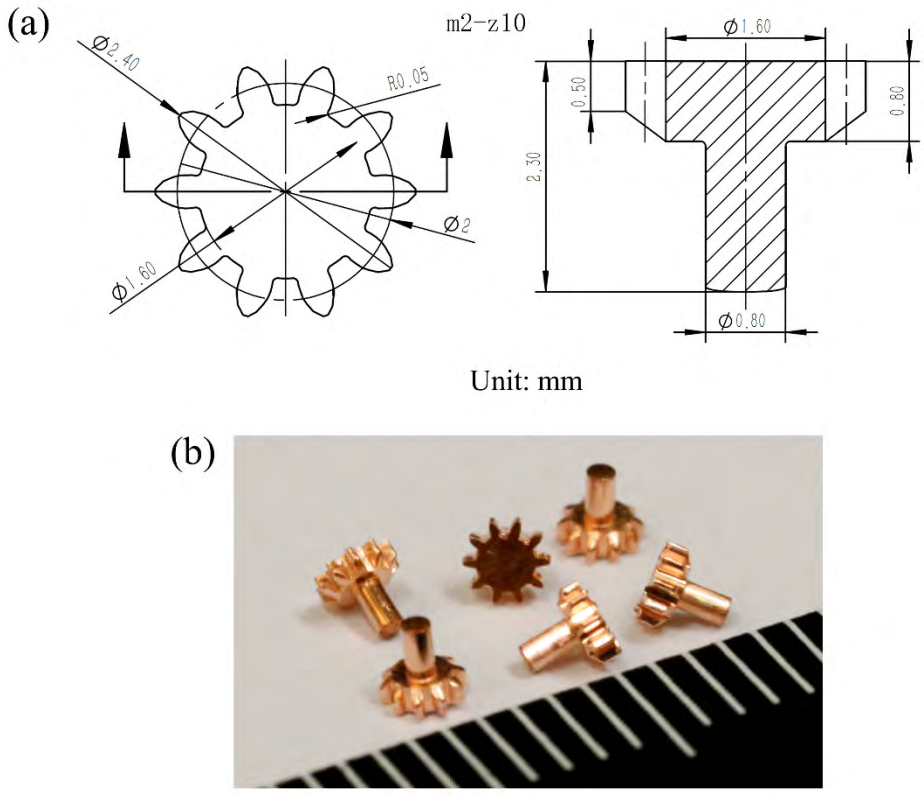

Fig. 5.5 (a) Dimensions of the case study part – pure copper gear shaft (m2-z10) with a modulus of 2, 10 teeth, 2.4 mm tip diameter, 1,6 mm root diameter, and 2 mm pitch diameter. (b) The progressive meso-formed pure copper gear shafts with various initial grain sizes.

5.3 Simulation setup and constitutive modelling framework

5.3.1 Simulation setup of progressive meso-forming process

The progressive meso-forming system was modelled as depicted in Fig. 5.6. Simulations based on CEL and CPFEM were conducted within the ABAQUS/Explicit environment, whereas Deform3D was utilized for FEM simulations. Considering the

computational expense, only a segment of the cylinder was generated to represent the raw material. For CEL and CPFEM, the material was simplified to a 18/360 ratio, representing half a tooth, whereas a 72/360 ratio was used for FEM. In the simulation, the progressive meso-forming system was simplified by only retaining the punches, dies, and blank holder. All tooling components were configured as rigid bodies. Within the manufacturing process, Step I punch initially moves downward along the Y-axis. Upon completion of Step I, Step I punch and die retract, and the Step II punch and die are positioned to initiate Step II. The gear shaft can be manufactured in a manner analogous to the experiments. Cyclic symmetry boundary conditions were applied. Moreover, a friction coefficient of 0.12 was utilized for simulations, which is a common value in cold forming with lubricating oil [171]. The penalty contact algorithm was applied to all possible contacting surfaces between the material and other 5 tooling parts.

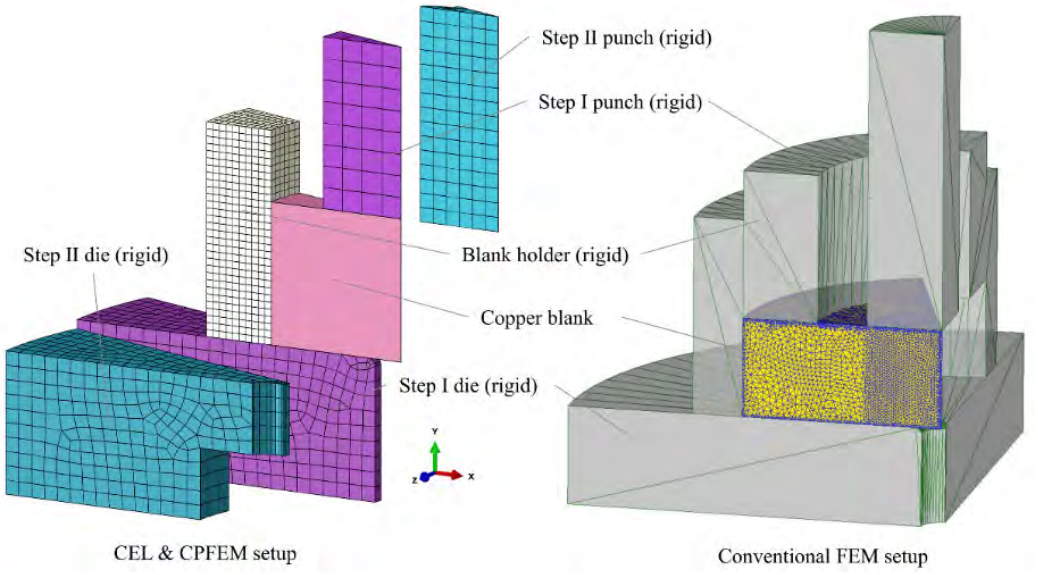

Fig. 5.6 Simulation setup of progressive meso-forming for various approach.

5.3.2 CPFEM and CEL based modelling

For the constitutive models used in the CPFEM simulations, most of them follow the equations mentioned in Section 3.2 except for the FCC single slip hardening model:

$$h_{\alpha\alpha} = h_0 \left(1 - \frac{g^{\alpha}}{\tau_s}\right)^a. \tag{5.2}$$

Here h_0 and τ_s are the primary hardening modulus and saturation stress, respectively, identical for all slip systems. a is the rate sensitivity of the rage of strain hardening. In this CPFEM simulations, the parameters used for this material and research are listed in Table 5.1.

Table 5.1 Parameters in CPFEM simulation [172, 173].

C_{11} (GPa)	C_{12} (GPa)	C_{44} (GPa)	h_0 (MPa)	s_s (MPa)	τ_0 (MPa)	$\dot{\gamma}_0$ (s^{-1})	m (1)	$q^{\alpha\beta}$ (1)	a (1)
168.4	121.4	75.4	180	148	16	0.001	0.05	1.4	2.25

The CPFEM simulations were conducted in the ABAQUS/Explicit environment using a user-developed VUMAT subroutine to define the constitutive relations. To solve the computational issue in modelling the microstructure of an entire sheet, a hybrid modelling manner is proposed. It mixes the FEM approach to assess the overall structure with the CPFEM method in order to high-fidelity microstructural simulation over the critical areas, which has been utilized and proved with great results in our prior study [33]. As demonstrated in Fig. 5.7 (b), the pink parts represent traditional FEM modelling, while the rest of the parts are modelled using CPFEM. By comparison with Fig. 5.6, it shows that the FEM part is far away from the final formed part during the manufacturing process, so this strategy can effectively reduce the consumption of computational resources in unnecessary places. The tessellation (CPFEM zone with

radius of 1.2 mm and a 2 mm height) was created using a controlled Voronoi method, covering the material that is direct contact with the punch. The adjoining two zones were bonded with the layer with zero-free cohesive elements. In all models, cohesive zones between elements were included to capture the fracture, modelling the apparent fracture behaviour at the tooling contact area observed in the experiments. This distribution of cohesive zones can be observed in Fig. 5.7 (b), and the cohesive elements were set between all element surfaces inside the blue frame. This setting can not only be strategic and smart for reducing superfluous computational work since they are not applied in parts that are highly unlikely to be fractured, but they also guide the direction of fractures locally (independent of the overall shape of the object). This targeted strategy provides an optimal balance between computational efficiency and simulated effectiveness while maintaining a competitive performance in the fracture prediction.

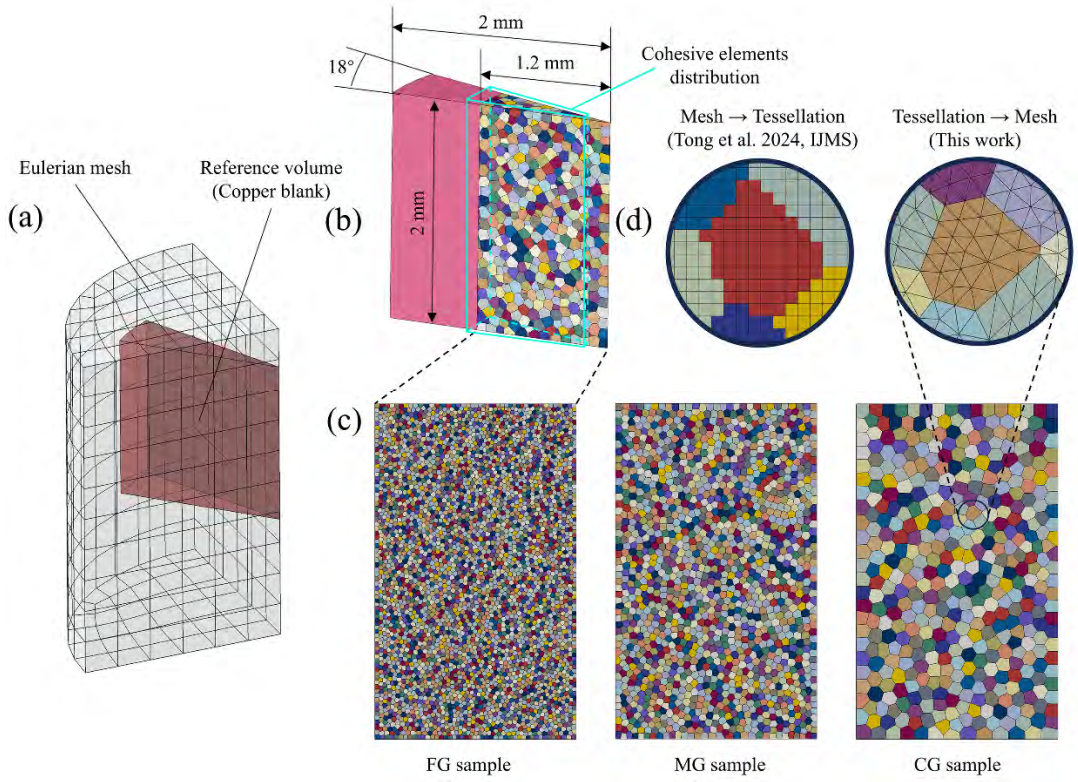

Fig. 5.7 (a) Modelling of the CEL approach includes the reference volume and Eulerian mesh part. (b) The modelling of material for CPFEM, its dimensions, and the distribution of cohesive zones. (c) CPFEM modelling setup and models for FG, MG, and CG samples. The tessellation was created by using a controlled Voronoi method, and a uniform grain size generating method was applied. (d) The tessellation-mesh approach was used in this research instead of the opposite way in our prior study [33].

As for the meshing, a different approach was used in this study as compared to our previous work [33]. In the previous method, the model was first meshed and then divided into multiple grains. Nevertheless, this approach may cause a lot of errors in the mesh distortion. For this research, a different method was applied in which tessellation was first generated and that tessellation was then meshed, as presented in Fig. 7(d). This greatly reduces the frequency of errors due to the use of tetrahedral elements [174, 175], and the mesh size can be increased (0.01 mm) to shorten computation time. C3D10M and COH3D6 mesh types were applied for the copper elements and cohesive elements, respectively. Additionally, random initial grain orientations were assigned to the grains. The generating method of those grain orientations has been introduced in Section 3.3.2.

As shown in Fig. 5.7 (a), the sector-cylinders were constructed with a height and radius of 2 mm during the CEL modelling stage. The grain-size-dependent variations in modelling stage were predicted on the material settings. The material properties, including material density, Poisson's ratio, Young's modulus, flow stress, and fracture strain, were derived from the uniaxial tensile tests in Section 5.2.1, and were applied in both CEL and FEM simulations. In the numerical simulation employing CEL, the Eulerian material distribution across the mesh is followed by the Eulerian Volume

Fraction (EVF) [176, 177]. Whin this context, the EVF is a dimensionless number that indicates how much of the volume of the implemented Eulerian element is filled with material, ranging from 0 (where no material is present) up to 1 (where the Eulerian element is fully packed with material). This metric is crucial for depicting material flow and establishing accurate values for the numerical analysis using the CEL framework. That is, the reference volume represents the undeformed material and the Eulerian mesh part is created to cover the whole region the material may deform into.

For the meshing part in conventional FEM simulation, the minimum mesh size must be reduced to a certain degree (0.002 mm), and arbitrary Lagrangian-Eulerian remeshing (ALE) must be utilized to ensure that the distortion issue does not appear [178, 179]. However, according to Qiu et al. [180], the mesh effects on computational cost and simulation results in the CEL method are not significant. Therefore, a larger mesh size of 0.4 mm and the EC3D8R mesh type were applied to all CEL simulations in this study. The general contact algorithm, which utilises the penalty contact approach, enables CEL to effectively manage the interaction between two distinct domains, namely Eulerian and Lagrangian domains. This is a rather relaxed alternative to the kinematic contact method but it is a practical method to handle contact issue. The seeding starts from the edges of the Lagrangian particles and anchor points are placed on the Eulerian surface. It achieves hard pressure closure via the penalty method by permitting a slight overlap between Eulerian and Lagrangian materials, thereby facilitating contact and interaction between the two domains in the simulation [181, 182].

5.4 Results and discussion

5.4.1 Efficiency of computation considering size effect

The CPU consumption of various simulation methods is evaluated to compare computational efficiency, as shown in Fig. 5.8. In this study, all simulations were performed on the same workstation. The computational time statistics only include the effective forming times of the first and second steps, with the time consumed by tooling movement subtracted from the total time. It is revealed that the CEL simulations for meso-scaled gear shaft in this study took approximately 1x107 s CPU time for different initial grain sizes. In the modelling process for the CEL simulation, the material property is the only input variable, while the mesh size, load conditions, and boundary conditions are kept constant. The increment time in ABAQUS/Explicit is influenced by meshing and material properties [89]. As the mesh size, Young's modulus, Poisson's ratio, and material density remain identical in the CEL simulations—despite variations in grain size—this explains the nearly identical computation times observed. For CPFEM, however, the corresponding cost is three times that of FG, and twice that of MG and CG samples for CEL, respectively. Firstly, the computational costs are higher because CPFEM is intrinsically more complex, which necessitates calculating activation and slip on each of the slip system in every grain at each increment. Secondly, this SE is caused by the variation in meshing. Whilst the models were assigned the same 0.01 mm mesh size, the practical lower limit is 0.005 mm due to the intricate grain boundary complexities in finer-grained materials. Within the framework of the novel tessellation-mesh methodology, numerous grain boundaries—either excessively short or characterised by minimal pinch angles—result in reduced mesh dimensions. This leads to smaller mesh sizes and an increased total number of meshes.

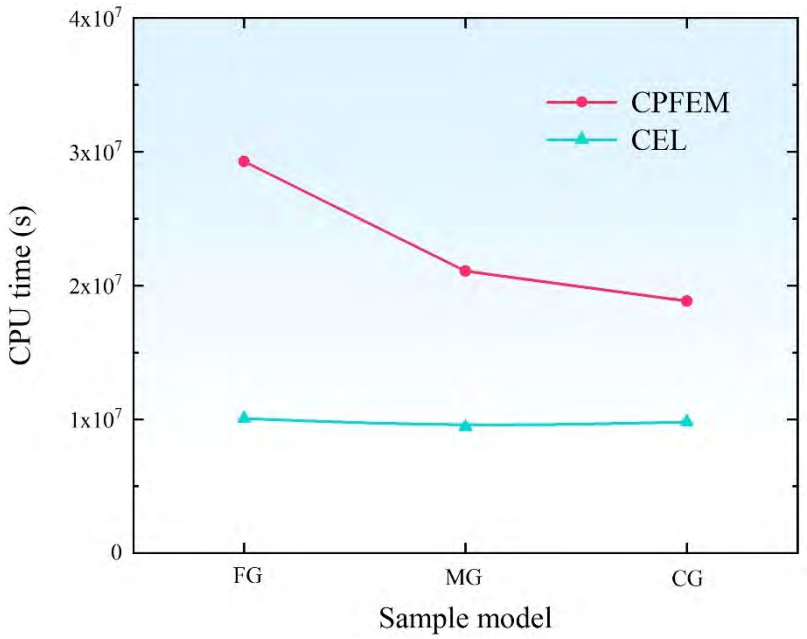

Fig. 5.8 Comparison of computational consumption of CEL and CPFEM for various grain-sized samples. CPFEM is twice more expensive than CEL and is more time-consuming to model in simulation of the fine-grained sample.

5.4.2 Load-stroke relations affected by size effect

In progressive forming, the load-stroke control not only affects the entire tooling and feeding systems but also contributes to imbalance and reduced service life of punches [183, 184]. Fig. 5.9 presents a comparative analysis of the experimentally obtained and simulated load-stroke curves. To ensure reliability, the average data from three repeat experiments were utilized for reference. Given that the simulations only modelled a portion of the material, the simulated load data were scaled up to match the full experimental conditions, facilitating a direct comparison between the experimental and simulated results. In Step I, the load tends to increase essentially linearly with the stroke, based on the experimental results. At a stroke of 0.1 mm, material fracture first occurs and the rate of load increase accelerates and continues to

the final designated termination stroke of 1.2 mm. The point at which this material fracture initiates varies from simulation to simulation: the FEM at 0.5 mm (Fig. 5.9 (a)), the CEL at 0.15 mm (Fig. 5.9 (c)), and the CPFEM at around 0.6 mm (Fig. 5.9 (e)). The maximum loads predicted by FEM and CEL are lower, while in CPFEM they are similar to the experimental results at about 8200-8400 N. It can be concluded that the load increases with a finer-grained material in both steps, aligning with the grain SE in the flow stress curve shown in Fig. 5.3. This grain SE can also be observed in the FEM simulations, but is not as pronounced in the other two methods.

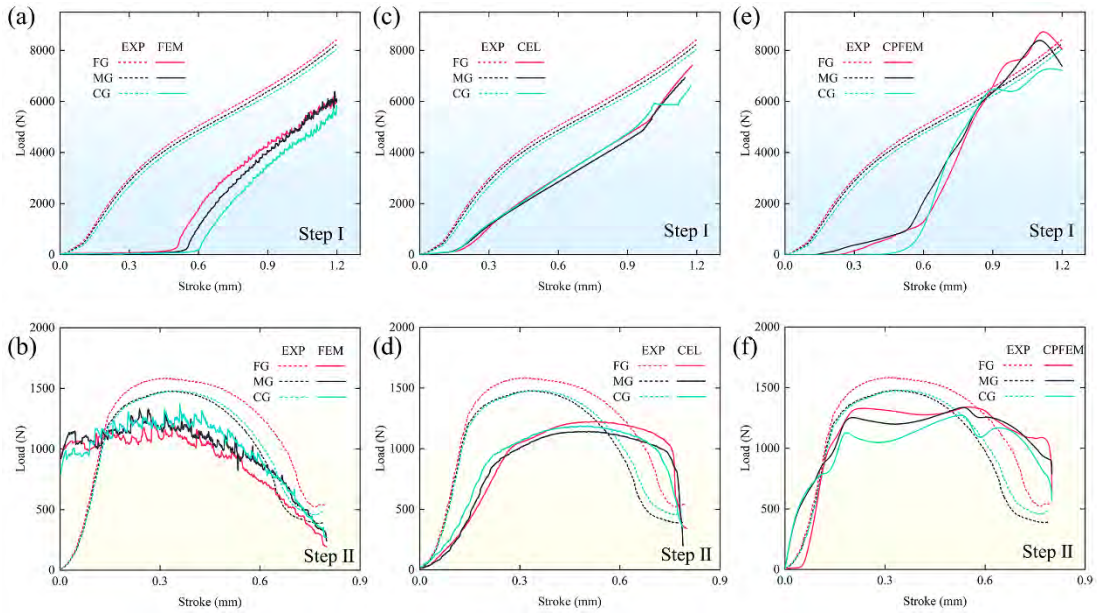

Fig. 5.9 Deformation load-stroke curves for experimental and simulated results with various grain-sized sample and simulation methods: (a) Step I-FEM, (b) Step II-FEM, (c) Step I-CEL, (d) Step II-CEL, (e) Step I-CPFEM, and (f) Step II-CPFEM. CEL can predict the trend of the load variation, but it is numerically smaller; the maximum value of the CPFEM is close to the experimental results; and the FEM deviates more from the actual load-stroke curves.

Step II represents a quintessential shearing/blanking operation, during which the load curves are characterized by three stages: rapid rise, stabilization, and gradual decline,

as illustrated in Fig. 5.9 (b, d, and f). The loads predicted by all three simulation methods are less than the actual forming loads, with CPFEM exhibiting the closest approximation. The grain SE in Step II is the same as it is in Step I, and it can be observed in CPFEM but not in FEM and CEL this time. Collectively, the three simulations are capable of forecasting the general trends, with CPFEM achieving the maximum load values that are in closest alignment with the experimental data, whereas the other two methods show greater divergence from the experimental outcomes. Furthermore, the grain SE is also partially reflected in the simulation results

5.4.3 Flow behaviour and microstructure evolution affected by size effect

In the forming processes of complex parts, comprehending the flow behaviour and microstructural evolution of the material is essential for enhancing product quality and controlling the production process [185, 186]. As a quintessential component for connection and transmission, the gear shaft is depicted in Fig. 5.10. From the main view (Fig. 5.10 (a)), the gear shaft can be divided into the head and shaft, with the outermost part of the head and the lowest part between the teeth designated as the tip and root, respectively. The heights of the tip, head, and shaft as shown in the main view, and the diameters of the tip, root, and shaft as indicated in the top view, constitute critical dimensions for assembly and validation purposes. This subsection is dedicated to discussing the microscopic experimental characterization and analysis of cross-sections of these important features.

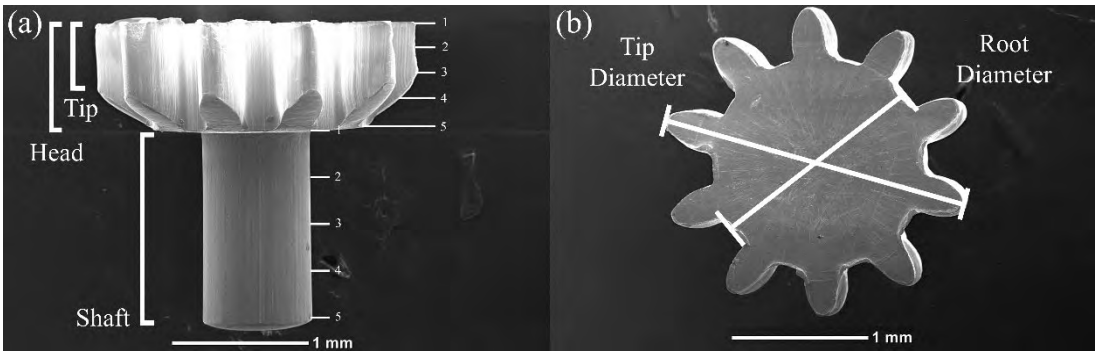

Fig. 5.10 SEM observations of the final formed gear shaft: (a) main view and (b) top view. The gear shaft can be divided into head and shaft parts. The outermost part of the head is tip, and the lowest part between the teeth is root. The heights of the tip, head, and shaft shown in the main view, the diameters of the tip, root, and shaft shown in the top view are important assembly or validity dimensions. The measuring points for tip and shaft diameters are illustrated in (a).

In processes involving large deformations, the work hardening effect often characterises the direction of material flow and the degree of strain accumulation [187, 188]. This strengthening arises from dislocation motion and generation within the material's crystal structure. In this study, micro-scale Vickers hardness tests were conducted on the tip and root cross-sections of the gear shaft to assess the distribution of shear bands and dead metal zones. The initial hardness values and experimental results for various regions are presented in Fig. 5.11. Fig. 5.11 (b) details the locations of hardness tests and their corresponding measured values. Compared with the initial values, there is a marked increase in hardness across all areas as a result of the large deformation. The highest hardness areas are 121-128 HV, primarily situated on the lower side of the head and in the corner between the head and the shaft, where the streamlines are most concentrated. The second most hardened area is found in the tip, indicating another shear band. The area on the upper head has no significant material flow, but it is in contact with the punch in both forming steps, resulting in a hardness

value of around 90 HV. The shaft, located at the bottom of the part, is engaged only in the first step and exhibits the lowest hardness. The hardness along the central axis of the shaft decreases from 100 to 68 HV from top to bottom. In contrast, the shaft surface exhibits significantly higher hardness than the intermediate material, attributable to the severe deformation and material fracture during the first step. Furthermore, the overall hardness value decreases with increasing grain size, as shown from Fig. 5.11 (b1) to Fig. 5.11 (b3).

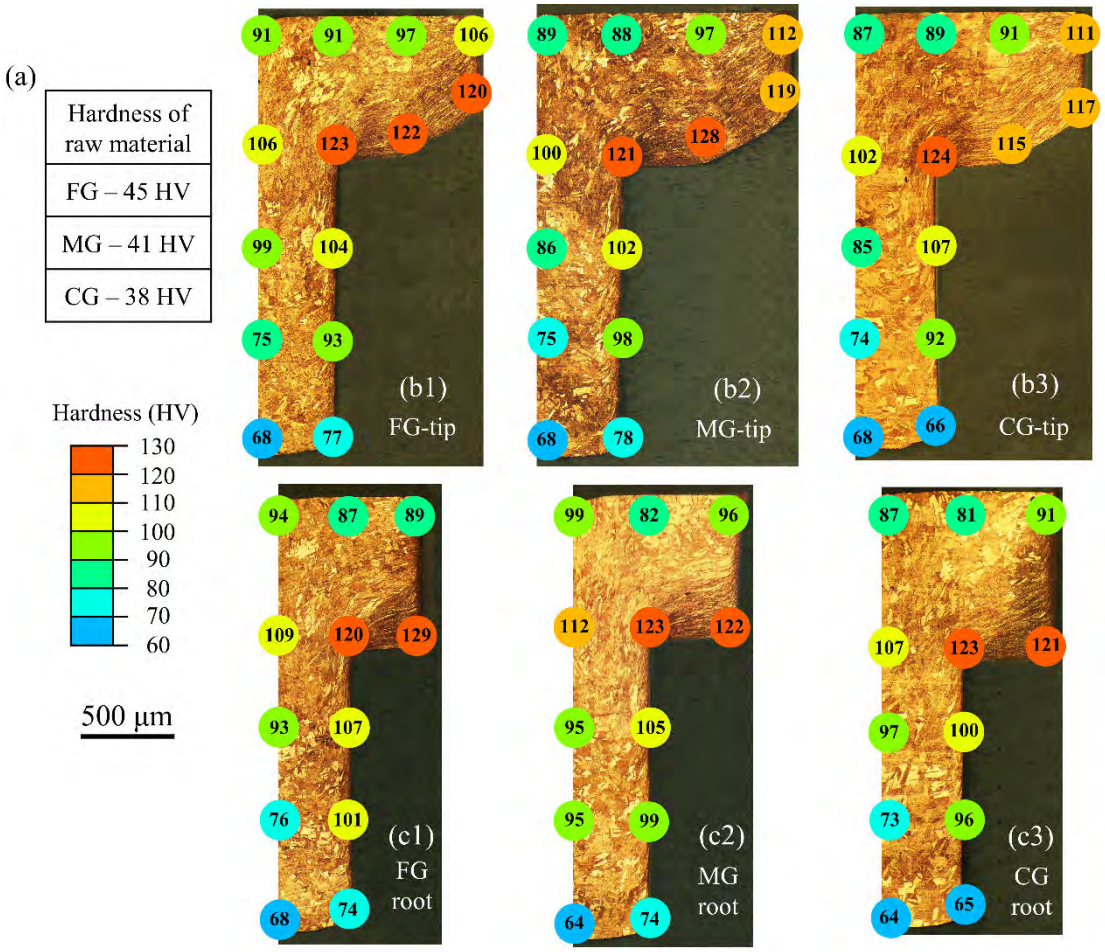

Fig. 5.11 (a) The hardness of undeformed annealed material, and the hardness distribution on various zones of (b) tip and (c) root. The highest hardness areas are mainly found on the lower side of the head and in the corner between the head and the shaft, where the material deformed the most. The lower and middle part of the

shaft has the lowest hardness.

Fig. 5.11 (c) displays the metallographic images of root cross-sections and hardness distribution for samples with differing grain sizes. Compared to the tip cross-sections, the shaft demonstrates similar characteristics irrespective of grain size, while the head exhibits marked variations. The lower side of the head in the root is oriented perpendicular to the loading direction, whereas at the tip, a substantial angular shift occurs, leading to a notably smaller shear band at the root. Beyond these distinctions, hardness remains largely uniform across all other regions. A consistent grain SE is evident, stemming from variations in work hardening caused by differences in grain boundary density. These boundaries hinder dislocation movement and are responsible for the pile-up effect.

Based on the hardness test results, insights into material flow behaviour and deformation zoning within the component have been established, which will now be analysed in conjunction with simulation outcomes. Fig. 5.12 provides a comparative visualisation of effective strain distributions and microstructural compactness within the tip cross-sections of gear shafts for varying grain sizes, derived from experimental measurements and simulations (FEM, CEL, and CPFEM). The effective strain maps explicitly illustrate material deformation and strain localisation, offering critical insights into the material's response under applied loads. These maps highlight stress gradients and concentration zones, which are pivotal for evaluating mechanical performance and potential failure modes in the gear shafts. As illustrated in Fig. 5.12 (d), the shear band contains the densest flow lines, indicating that the material flow and cumulative strain are greatest in this region. This can be inferred from the strain maps, as shown in Fig. 5.12 (a-c). In this case, the red part (high strain values) in both FEM and CPFEM covers only a part of the region in shear band I, while CEL gives

results that do not differ much from the experiments. The dead metal zone, which means the material involved does not deform very much, covers other areas, including the upper and middle of the head and almost the entire shaft except for the surface.

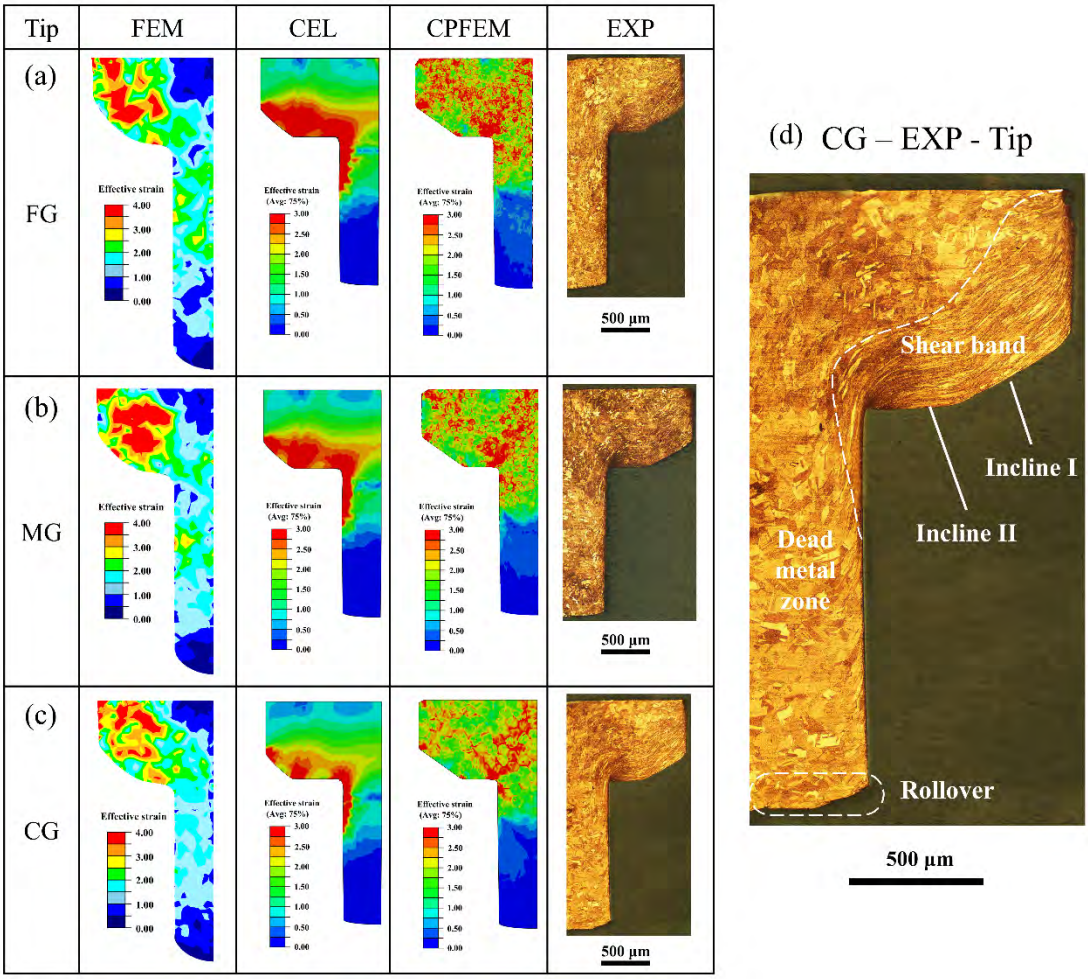

Fig. 5.12 The analysis compares the effective strain distributions and microstructural alterations observed at the tip cross-sections of gear shafts for (a) FG, (b) MG, and (c) CG samples, as derived from experimental data and simulations using conventional FEM, CEL, and CPFEM methods. (d) Specifically, the metallographic examination of the CG sample reveals the presence of dead metal zones and shear bands, which are indicative of the material flow patterns and potential sources of geometric irregularities.

From CG to MG to FG samples, the flow lines in shear band become denser, and the area expands. This is because, firstly, finer grain sizes involve more grains in large deformations, and secondly, friction between surface grains and tooling in FG materials constrains rapid material flow, creating a stark contrast between surface and inner grain behaviour. The widening shear bands reflect a narrowing dead metal zone, observable in strain maps. Despite variations in strain thresholds and distributions across simulations, high-strain regions consistently shrink as grain size increases. Both CEL and CPFEM simulations align more closely with experimental strain gradients in non-high-strain zones compared to hardness distributions. CPFEM uniquely reveals strain variations between grain interiors and boundaries due to explicit grain delineation, highlighting how grain boundaries influence strain partitioning (e.g., dislocation pile-ups). These insights emphasise the critical role of grain boundaries in strain heterogeneity and the necessity of grain-scale modelling (CPFEM) for capturing microstructure-driven deformation mechanisms. The red area is spider-webbed from the corner where the head and shaft meet, which highlights the advantage of CPFEM in representing material heterogeneity. The shaft can be divided into three zones according to CPFEM simulations: green, light blue, and blue ones, which are validated by the hardness tests.

Fig. 5.13 collects the simulated and experimental results of root cross-sections. Compared with the tip cross-sections, the dead metal zones are getting bigger, and the shear bands become much smaller. It can be inferred that the size of the region of shear band induced by the first step is shown in Fig. 5.13 (d), and the other region of this shear band was caused by the second step. The high strain regions in CEL and CPFEM are shrinking with the increasing grain size, but this effect is not as pronounced in the experiments. It is noteworthy that some high strain regions (red ones) in CPFEM are located inside the dead metal zone, for instance, the upper part of the head. This is

mainly caused by the heterogeneity of the polycrystalline material and the enhancement of the grain boundaries mentioned previously. In this study, the method of randomly assigning crystal orientations does reduce the cost of material characterization on the one hand, but on the other hand, it affects the misorientation distributions of the whole material. Excessive misorientation angles inevitably lead to more difficult dislocation transfer at the grain boundaries of neighbouring grains, resulting in higher stresses and strains. However, the heterogeneity it reflects is more realistic and informative compared to FEM and CEL.

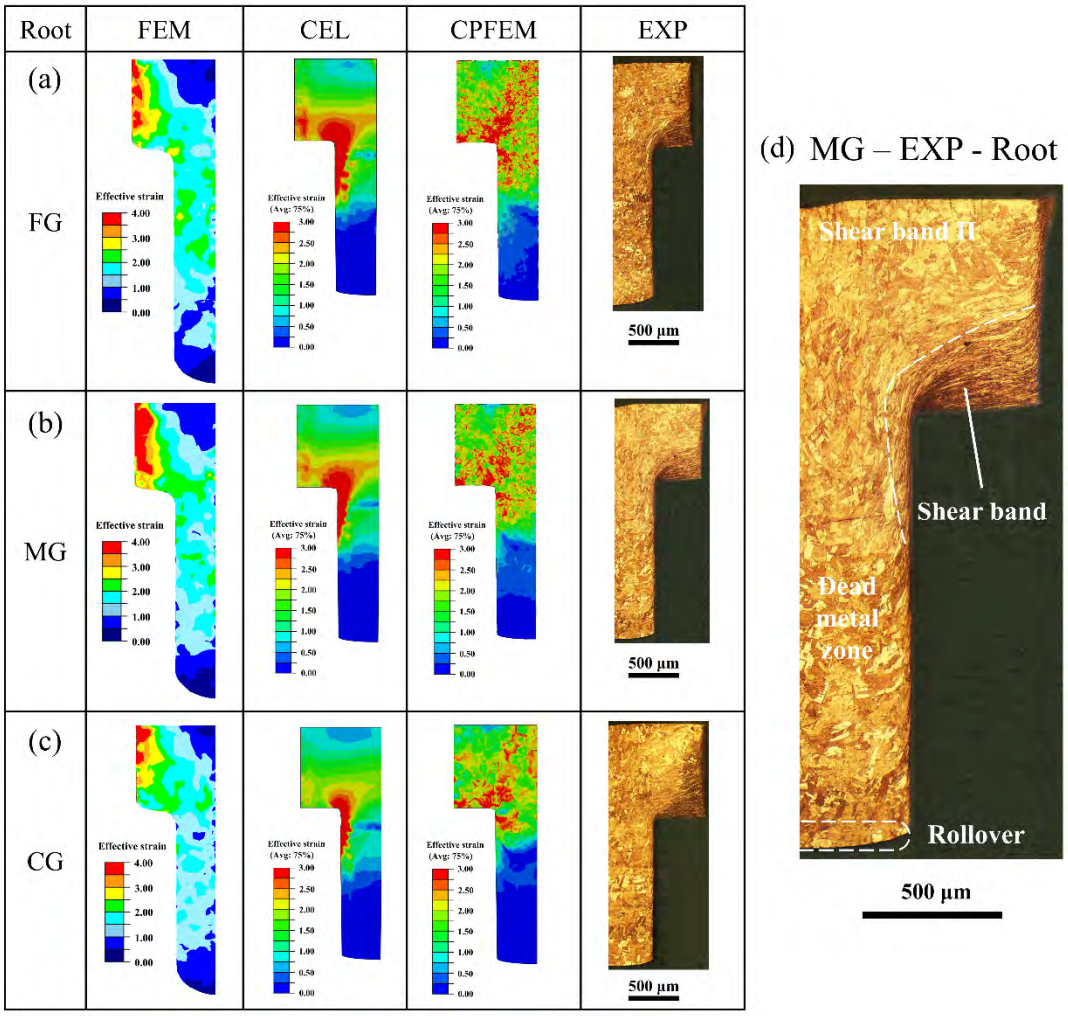

Fig. 5.13 The analysis compares the effective strain and microstructures in the root cross-sections of gear shafts for (a) FG, (b) MG, and (c) CG samples with

experimental data and simulated results of FEM, CEL, and CPFEM methods. respectively. (d) The MG sample's metallographic image reveals dead metal zones and shear bands, which are critical indicators of material flow and potential sources of undesirable geometries.

5.4.4 Dimensional precision affected by size effect

The tip and shaft heights are critical dimensions for the gear shaft's functionality in transmission. The measurement locations for tip, head, shaft, and total heights are shown in Fig. 5.10 (a), with experimental and simulated results compiled in Fig. 5.14. The designed dimensions are 0.5 mm (tip height), 0.8 mm (head height), 1.5 mm (shaft height), and 2.3 mm (total height). Two distinct grain SEs are evident in the experimental results. First, all heights decrease as grain size increases, except for the tip height. Second, variations in dimensions remain within 30 μm but exhibit a tendency to increase with larger grain sizes. These findings align broadly with prior research [33], due to the narrower range of grain sizes investigated in this study. Fig. 5.14 (b) illustrates the measured tip heights in experiments and simulations. It is revealed that the CEL-FG, CPFEM-MG, and CPFEM-CG models predict the tip heights well for the corresponding grain size, respectively. The FEM simulations not only give measurements that differ significantly from the experimental results but also show a grain SE that should not be present. For the head heights (Fig. 5.14 (c)), all three simulation methods overestimated the values, while CEL and CPFEM gave closer results to the design dimension of 0.8 mm than the experiments. For the total height of the gear shaft (Fig. 5.14 (e)), the grain SEs reflected in the three simulation methods are the same as those in the experiments, but FEM still gives higher values, which can be observed in Figs. 5.12-5.13.

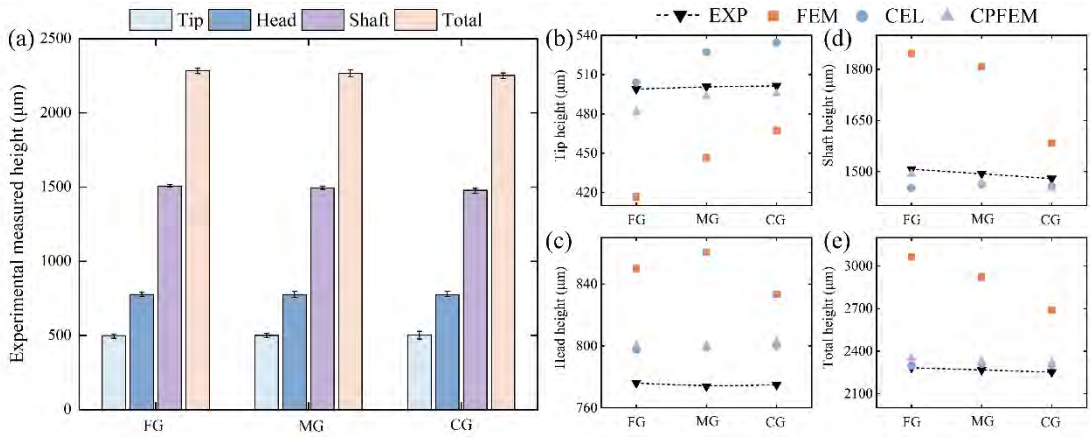

Fig. 5.14 (a) The experimental measured heights of tip, head, shaft, and comparisons of FEM, CEL, and CPFEM simulation results of (b) tip height, (c) head height, (d) shaft height, and (e) total height. The results of FEM are very different from the actual situation. The simulation results of CEL are close to the experimental results, but cannot reflect the grain SEs; whereas CPFEM can predict both successfully.

The variation in shaft height (extrudate length) has been a difficulty in similar studies over the years. One reason is that the materials and extrusion ratios are different; another is that opposite conclusions have been reached, in which even the scatters vary a lot; the third is that the physical principles have not been analysed. The extrudate length is strongly influenced by grain size, cavity width, and their ratio. In this study, the extrudate length increases with finer grain size. To analyse this grain SE, a physical polycrystalline model was developed, as illustrated in Fig. 5.15. On the one hand, Wang et al. [189] observed that in micro-coining processes, for a specific cavity width, extrudate height decreases with increasing grain size when the ratio of grain size to cavity width is below 0.25. In this study, the ratios for FG, MG, and CG samples are 0.0285, 0.0433, and 0.0743, respectively—all below 0.25. Consequently, material filling into the cavity diminishes as grain size increases. Conversely, surface grains undergo significant friction during extrusion. The meso/microforming approach yields a higher grain-to-feature size ratio compared to macro-forming, amplifying disparities

in both grain size and frictional effects. As shown in Fig. 5.15, inner grain movement is heavily constrained by surface grains. For CG samples, larger grain sizes result in greater surface grain coverage, elevating overall material resistance. These surface grains, having already undergone great deformation, primarily rely on spatial displacement, rotation, and minimal compressive deformations to accommodate the overall deformation during subsequent compression. When the movement of surface grains is constrained on both sides, it becomes more challenging for inner grains to move, which reduces the overall extrudate length. In summary, a longer effective extrudate length implies less material loss, making FG materials more advantageous for enhanced material utilization.

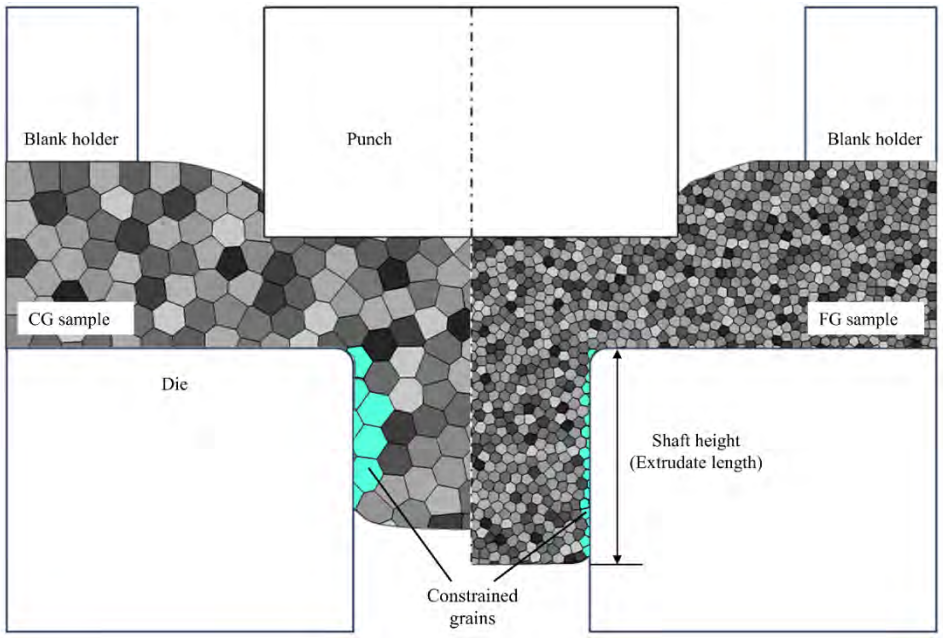

Fig. 5.15 Schematic illustration of the shaft height (extrudate length) difference between CG and FG materials.

The tip diameter (outside diameter), defined as the diameter of the circle connecting tooth tips, and the shaft diameter—critical for interfacing with hollow components or

fasteners—were experimentally measured as shown in Fig. 5.16 (a-c). Five measurement points were established: three on the tip surface and two on incline I (marked in Fig. 5.10 (a)). The tip diameter exhibits a gradual decrease, with a more pronounced linear reduction observed along incline I. The first measurement point (uppermost tip region) shows larger values than the second (0.25 mm below), attributed to burr formation during the punching/blanking process. This burr generation primarily results from punch-die clearance effects in the forming operation. The formation of incline I is because the material fracture first occurs on the root circle in the blanking step. The designed tip diameter is 2.4 mm, and only the FG case gave the closest results. Fig. 5.16 (d-f) lists the experimental measured shaft diameters from top to bottom. The five measurement points are also equidistant, and the fifth measurement point is located at the junction of the body and rollover. Though the designed value of the shaft diameter is identical to 0.8 mm, it still shows a gradual decrease from top to bottom. Furthermore, a clear grain SE can be found that the finer-grained specimens have a larger shaft diameter.

In contrast to the pronounced grain SE observed experimentally, simulated tip diameter measurements show greater consistency across methods (FEM, CEL, CPFEM), as seen in Fig. 5.16 (a-c). While FEM simulations accurately replicate burr formation (evident in Fig. 5.12), the other two methods exhibit shape variations. FEM and CEL provide reliable predictions for tip diameter, whereas FEM and CPFEM better capture sensitivity to incline I geometry. However, CEL significantly overestimates the incline section diameter. For shaft diameter (Fig. 5.16 (d-f)), simulation results diverge markedly: CPFEM simulations align with the expected gradual downward trend, while FEM and CEL exhibit unphysical fluctuations (e.g., FEM-CG, CEL-FG/MG), contradicting extrusion principles. During extrusion, grains subjected to sequential extrusion and shear undergo refinement from top to bottom due

to die squeeze and friction—a trend absent in all simulations. Furthermore, none of the simulations replicate the grain SE evident in experimental data, highlighting limitations in capturing microstructure-driven dimensional variations.

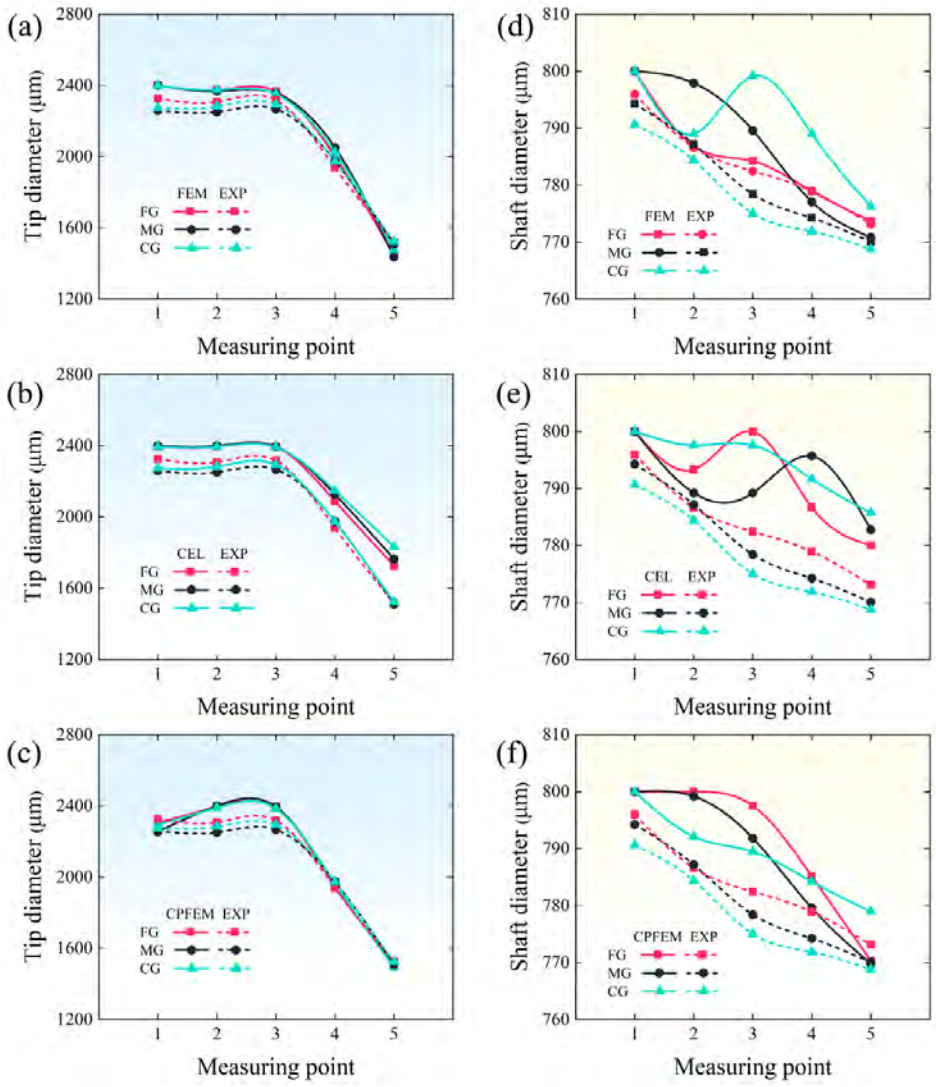

Fig. 5.16 The comparison of experimental and simulated measured tip diameter and shaft diameter: (a) (d) FEM, (b) (d) CEL, and (c) (f) CPFEM.

5.4.5 Surface quality affected by size effect

The surface roughness is an essential property for gears which are running under

different conditions [190, 191], and the grain SEs on surface quality cannot be ignored [192]. It basically controls the friction, contact temperatures, and consequently the different failure modes of the coating. In this work, the SEs in surface roughness, which is a crucial for the functioning of the gear coupling, and shaft joint, were investigated by investigating two important surfaces related to connections and transmissions: the tooth surface and the shaft surface, respectively. The 3D laser scanning microscope provides precise surface topography analysis, enabling direct correlation between grain size and surface roughness of critical components. As shown in Fig. 5.17, experimental measurements of curved surfaces were aligned using a three-point line configuration post-measurement. The results demonstrate a direct relationship between grain size and surface roughness, with larger grain sizes corresponding to higher roughness values. Significant scatter in the data indicates substantial variability in tooth surface roughness.

The calculation results were compared in Fig. 5.17. For both surfaces, the CPFEM gives almost twice the value of experimental results. On the one hand, it is because CPFEM is able to bring up the heterogeneity of polycrystalline materials. On the other hand, it is a result of the calculation method. The experimental measurements are based on the principle of hitting parallel lasers on a curved surface and counting the height difference. Although corrected by curve levelling, it is still essentially a parallel laser. However, according to Eqn. 3.8, the height of the distance from the centre axis to the node of that cylindrical surface is calculated for the shaft surface roughness. The latter essentially relies on straight lines with different angles, which inevitably leads to increased bias in the results. The calculated roughness of FEM and CEL is less than the actual situation because of the lack of material heterogeneity. In addition, CPFEM can reflect the grain SE and is in general agreement with the experimental results for the shaft surface.

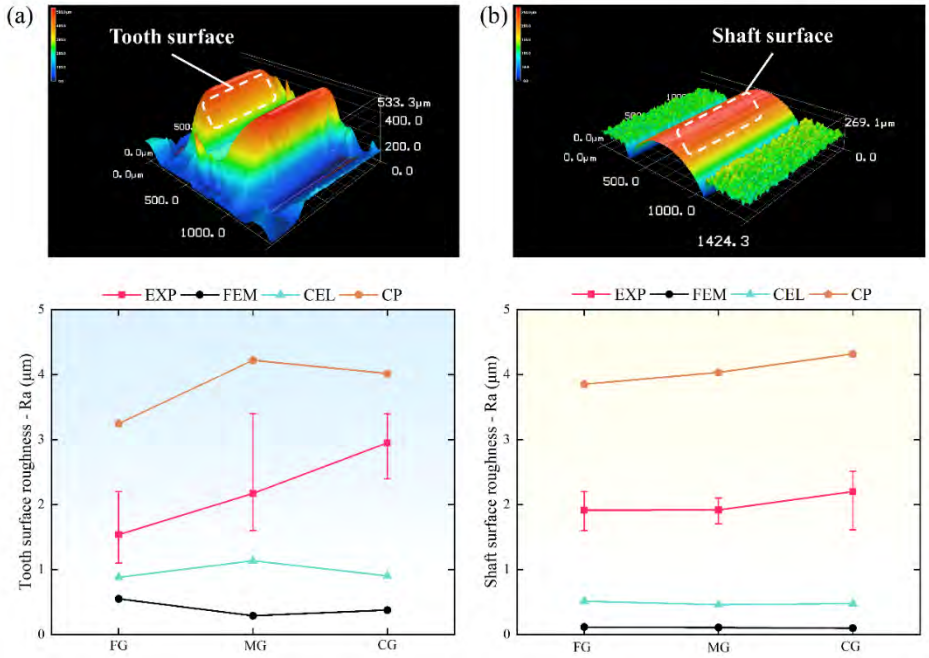

Fig. 5.17 The measured surface roughness of (a) tooth surface and (b) shaft surface based on experimental and simulated results. Both surfaces are critical working surfaces of the gear shaft as connections and transmissions.

5.5 Summary

This chapter presented a comprehensive evaluation of the CPFEM framework for simulating the progressive meso-forming of a pure copper gear shaft, with comparative analyses against Conventional FEM and CEL methodologies. A novel meso-forming system—integrating advanced control schemes, pressure apparatus, and tooling devices—was designed and manufactured to validate the computational predictions. The assessment encompassed deformation behavior, failure mechanisms, part quality under size effects (SEs), computational efficiency, and predictive accuracy, with key findings summarized as follows:

1) Both CPFEM and CEL demonstrated exceptional accuracy in predicting strain distribution, material flow, and microstructural evolution, outperforming

Conventional FEM in capturing shear bands, dead metal zones, and grain-level SEs. While CEL offered an optimal balance between computational cost and accuracy, CPFEM provided unparalleled precision in modelling grain-scale deformation and size effects, despite its higher computational demand. However, CPFEM exhibits notable limitations: (a) extreme computational expense due to explicit grain-resolved modelling, restricting its use to small-scale or localized simulations; (b) sensitivity to crystal plasticity parameters (e.g., hardening laws, slip systems), requiring extensive calibration; and (c) challenges in modelling grain boundary effects (e.g., void nucleation, intergranular fracture) without additional constitutive frameworks. These constraints currently limit CPFEM's industrial applicability for large-scale forming simulations.

2) The study elucidated the mechanistic role of grain size in extrusion processes: Constrained surface grains hindered the downward displacement of inner grains, amplifying surface deformation and reducing extrudate height; Larger grain sizes reduced cavity-filling efficiency, directly influencing part dimensions. These findings underscore the microstructure-macroscopic deformation linkage, highlighting the necessity of grain-resolved modelling (e.g., CPFEM) for meso/micro-forming processes. Nevertheless, CPFEM's reliance on idealized grain morphologies and simplified boundary conditions may introduce deviations from real polycrystalline behavior, particularly in dynamic recrystallization or grain rotation-dominated regimes.

3) CPFEM excelled in predictive accuracy for microstructural evolution and SEs but required significant computational resources. Its prohibitive runtime and memory demands make it impractical for iterative process optimization or industrial-scale simulations without high-performance computing infrastructure. CEL emerged as a practical alternative for industrial applications, offering

robust predictions with moderate computational expense. Conventional FEM proved inadequate for grain-sensitive processes, failing to resolve SEs and localized deformation features.

This study advances the development of efficient, high-accuracy forming simulations for complex meso/micro-components. The CPFEM framework establishes a foundation for microstructure-aware process optimization, while the comparative analysis guides methodology selection based on accuracy-computational cost trade-offs. To mitigate CPFEM's limitations, future work should explore: (1) reduced-order CPFEM models or hybrid CPFEM-CEL approaches for scalable simulations; (2) machine learning-aided parameter calibration; and (3) integration of advanced grain boundary mechanics. These steps will be critical to bridging the gap between academic research and industrial adoption.

Chapter 6 Linking Microstructure, Size Effects, and Deformation Mechanisms in Micro-Extrusion: A CPFEM-EBSD Integrated Study

6.1 Introduction

In Chapters 3 to 5, a novel CPFEM-size effects-product quality framework has been developed and assessed through meso/micro-scaled simple and progressive forming methods. However, at this scale, the vast majority of forming processes are closed-die processes, meaning that the deformation behaviours cannot be continuously observed to understand the fundamental mechanisms linking microstructure, size effects, and deformation. Driven by this objective, this chapter will focus on one of the most common closed-die processes, namely micro-extrusion. By integrating CPFEM with EBSD technology, the results of CPFEM will be practically applied to the optimization process of the forming process. This will quantify the influence of initial grain structure (size, orientation) and deformation-induced heterogeneity on meso/micro forming behavior and final part performance.

This chapter investigates the microstructural evolution and deformation mechanisms of CuZn32 brass during micro-extrusion using a novel combination of quasi-in-situ EBSD and CPFEM simulations. The integration of these techniques provides detailed insights into the complex interplay between grain size, deformation behaviour, and microstructural changes under severe plastic deformation. The results show that FG materials exhibit more pronounced grain refinement and strain localization compared to MG and CG materials. The distribution of equivalent plastic strain and stress is highly heterogeneous, with significant strain localization in shear bands and dead

metal zones (DMZs). The size and distribution of these zones vary with grain size, with FG materials showing more pronounced strain localization and larger DMZs. The micro-stress and micro-strain evolution reveal significant heterogeneity in deformation, with high stress and strain concentrations observed at grain boundaries and regions in contact with the die. In summary, the innovative combination of quasi-in-situ EBSD and CPFEM simulations provides a powerful tool for understanding the complex mechanisms governing microstructural evolution. These findings offer valuable insights for optimizing micro-extrusion processes to enhance material properties and performance.

6.2 Materials and experiment

6.2.1 Materials

In this study, CuZn32 brass was selected for micro-extrusion and compression testing due to its extensive industrial applications and well-characterised mechanical properties. The material was prepared in two geometries: semi-cylindrical specimens for micro-extrusion (Fig. 6.1 (a)) and cylindrical specimens for compression tests (Fig. 6.1 (b)). The compression specimens were designed to calibrate the CPFEM model by providing experimental deformation data under controlled conditions. To evaluate grain SEs on deformation mechanisms and mechanical properties, recrystallization annealing treatments were applied: 500°C for 1 hour, 600°C for 1 hour, and 700°C for 2 hours. Each annealing condition resulted in a distinct grain size and initial texture, as illustrated in Fig. 6.1 (c-e). The average grain sizes obtained from these treatments were 29.7 µm, 63.6 µm, and 154.4 µm, respectively. The initial textures and grain size distributions were characterized using EBSD analysis, providing a detailed understanding of the microstructural features of each sample.

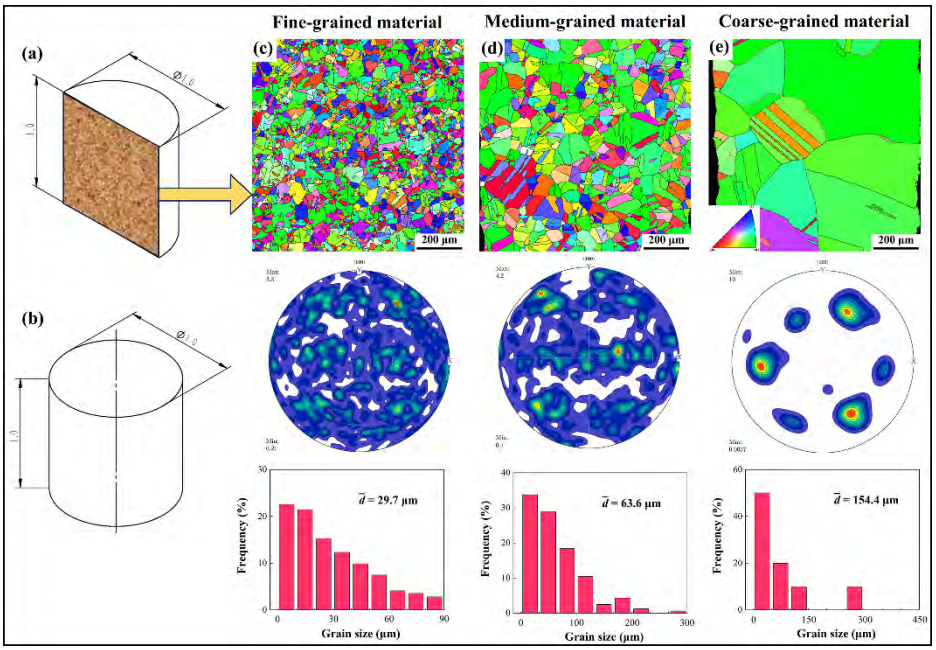

Fig. 6.1 Schematic illustrations and microstructural characteristics of CuZn32 brass samples used in this study. (a) Semi-cylindrical specimen for micro-extrusion testing; (b) Cylindrical specimen for compression testing; (c) EBSD micrograph showing initial texture and grain size of 29.7 μm after annealing at 500°C for 1 hour; (d) EBSD micrograph showing initial texture and grain size of 63.6 μm after annealing at 600°C for 1 hour; (e) EBSD micrograph showing initial texture and grain size of 154.4 μm after annealing at 700°C for 2 hours.

6.2.2 Micro-extrusion and quasi-in-situ EBSD tests

To facilitate quasi-in-situ EBSD analysis during the micro-extrusion process, a specially designed die assembly was developed, as shown in Fig. 6.2 (a). The die consists of two nearly identical halves separated by a central cross-sectional plane. During micro-extrusion, the two components are tightly assembled and secured using two locating pins, while the outer sections are clamped by additional tooling assemblies to prevent separation under the high extrusion forces. Unlike conventional cylindrical extrusion channels, this die features a semi-cylindrical structure. This

design not only ensures the mechanical equivalence to standard extrusion processes but also maintains the integrity of the cross-sectional surface for EBSD analysis throughout the experiment. In the micro-extrusion process, a semi-cylindrical CuZn32 brass specimen (1 mm height, 1 mm diameter) is positioned within the 1 mm diameter initial channel of die #1. A punch then extrudes the material at a quasi-static deformation rate of 0.005 mm/s, traveling a total distance of 1 mm. This gradually forces the material into the downstream channel of die #1, which features a reduced diameter of 0.5 mm, as depicted in Fig. 6.2 (b). All surfaces in the tooling assembly that may come into contact with the material were controlled to a roughness of Ra 0.8.

The specific experimental procedure is as follows:

1) The initial microstructure of the heat-treated material is characterized using EBSD to obtain a baseline of the grain size and texture.
2) The material is placed into the tooling assembly, and micro-extrusion is performed to achieve a 50% reduction.
3) The die is disassembled, and the partially extruded material is removed for EBSD analysis to capture the microstructural changes at this intermediate stage.
4) The material is then reinserted into the tooling, and the extrusion process is completed to the final deformation state.
5) The fully extruded material is retrieved and subjected to EBSD analysis once more to document the final microstructural evolution.

This experimental methodology enables precise monitoring of microstructural evolution across progressive stages of the micro-extrusion process, yielding critical insights into the underlying deformation mechanisms and grain SEs.

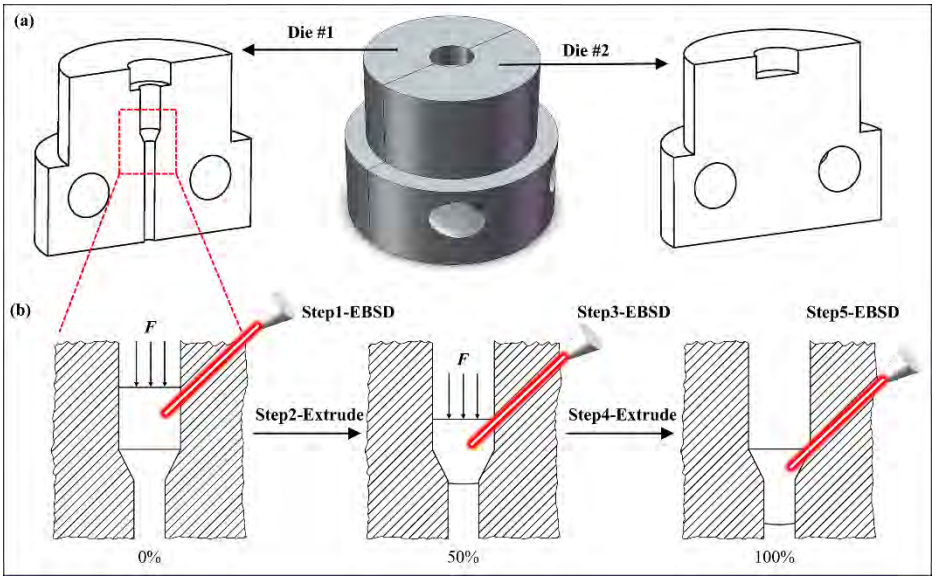

Fig. 6.2 Schematic illustration of the specially designed die assembly and experimental procedure for quasi-in-situ EBSD analysis. (a) Assembly of the die components showing the semi-cylindrical structure and the central cross-sectional plane for EBSD observation. (b) Detailed experimental procedure: (1) Initial EBSD characterization of the heat-treated material; (2) Placement of the material into the die and extrusion to 50% reduction; (3) Disassembly of the die and intermediate EBSD analysis of the partially extruded material; (4) Reassembly and completion of the extrusion process; (5) Final EBSD analysis of the fully extruded material.

6.3 Crystal plasticity modelling methods

The constitutive models within the CPFEM framework, consistent with Section 4.3.1, were implemented via a user-defined material (UMAT) subroutine in Fortran and integrated into ABAQUS/Standard for crystal plasticity simulations. The calibration process began with compression test modelling. A cylindrical RVE, matching the experimental sample dimensions (1 mm height, 1 mm diameter) and grain size distributions, was generated using Voronoi tessellation to replicate polycrystalline

microstructures (Fig. 6.3 (a)). To optimize computational efficiency, RVEs for FG, MG, and CG materials were discretized into 300, 150, and 17 grains, respectively, with element sizes of 0.01 mm (FG/MG) and 0.02 mm (CG). Initial grain orientations, defined by Euler angles extracted from experimental EBSD data (Fig. 6.3 (c)), ensured alignment between simulated and actual microstructures. Three independent RVE models per grain size category were simulated under identical compression conditions, with averaged results ensuring robust parameter calibration.

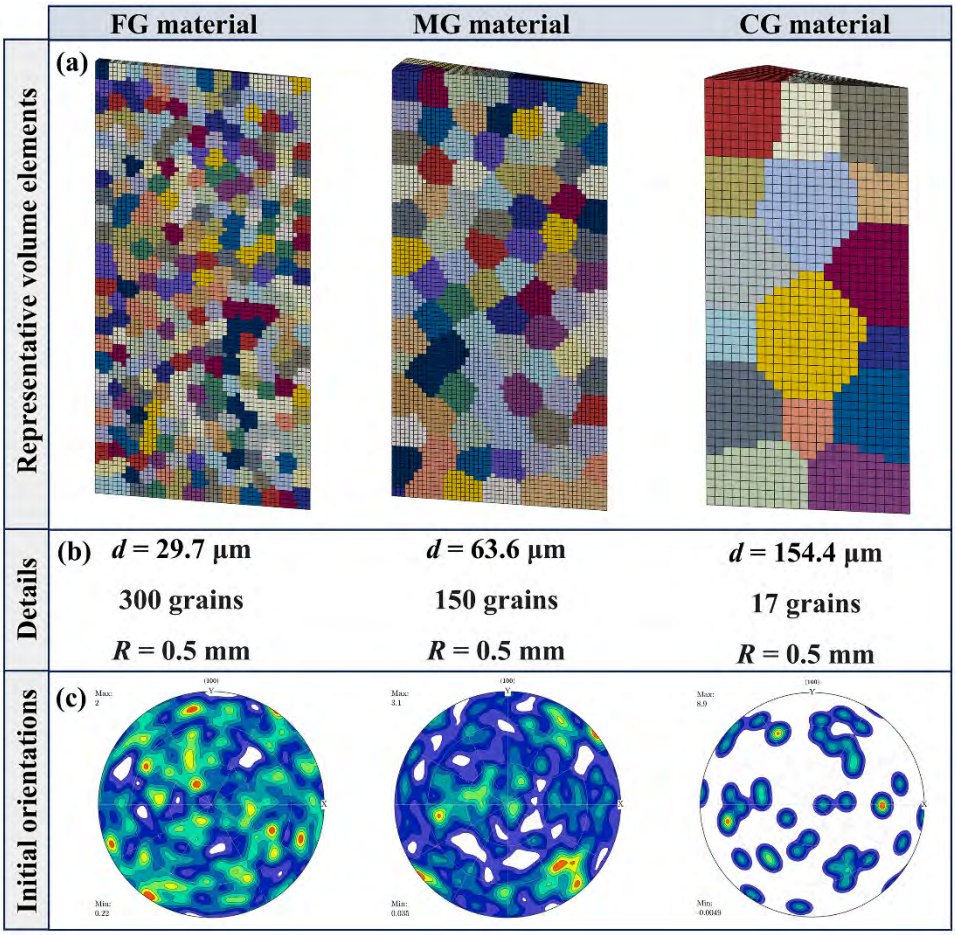

Fig. 6.3 (a-b) Schematic illustration of the cylindrical RVEs with Voronoi tessellation: FG RVE with 300 grains; MG RVE with 150 grains; CG RVE with 17 grains. (c) The initial grain orientations of RVEs were extracted from EBSD analysis.

In the constitutive models for CuZn32, the elastic parameters, $\dot{\gamma}_0^{\alpha}$, $\dot{\gamma}_0^{\beta}$, g_0^{β} (initial twinning resistance), *a*, and *b* are from our prior work [33]. g_0^{α} was offered by Li et al. [137]:

$$g_0^{\alpha} = \frac{1}{M}(\sigma_y + \frac{K}{\sqrt{d}}). \tag{11}$$

Here, yield stress σ_y is 107 MPa, 85 MPa, and 67 MPa for average grain sizes of 29.7, 63.6, and 154.4 μm, respectively. The Taylor factor $M = 3.06$. The Hall-Petch coefficient $K = 304\ \text{MPa} \cdot \mu\text{m}^{1/2}$. Moreover, the remaining parameters were calibrated by minimizing the differences between the simulated and the experimental results from the compression tests. All parameters used in the CPFEM simulations for this study are summarized in Table 6.1.

Table 6.1 Material parameters for CuZn32 used in the CPFEM constitutive models.

C_{11} (GPa)	C_{12} (GPa)	C_{44} (GPa)	$\dot{\gamma}_0^{\alpha}$ (s^{-1})	$\dot{\gamma}_0^{\beta}$ (s^{-1})	m
145	110	70	0.001	0.001	0.02
g_0^{β} (MPa)	g_{pr} (MPa)	a	b	η	
60	350	5	10	1.25	
d (μm)	g_0^{α} (MPa)	g_0 (MPa)	h_s (MPa)		
29.7	53	390	195		
63.6	39	375	190		
154.4	29	360	175		

The micro-extrusion simulation assembly and boundary conditions are depicted in Fig. 6.4 (a). A 2.5D modelling approach—extending the 2D EBSD data uniformly along the z-axis with layer thickness matching grain size—was adopted to balance computational efficiency with microstructural fidelity. As shown in Fig. 6.4 (b-d),

RVEs for FG, MG, and CG materials were reconstructed at 1:1 scale from EBSD data, preserving exact grain morphology, position, and orientation distributions. Each z-axis layer replicated the surface layer structure. The RVEs were meshed with C3D8 elements: FG (38,751 elements, 0.01 mm size), MG (30,384 elements, 0.015 mm), and CG (57,260 elements, 0.015 mm). Symmetry constraints were applied to the frontmost layer along the z-axis. Punch motion was simulated by imposing downward displacement on the top layer, while all RVE elements interacted with the die via a friction coefficient of 0.12.

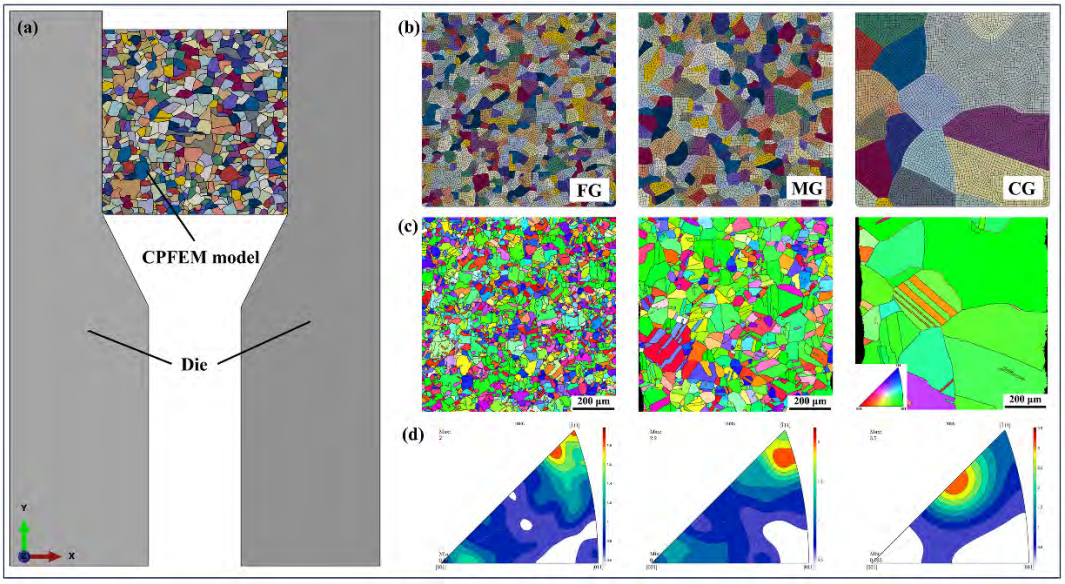

Fig. 6.4 Simulation setup for micro-extrusion using a 2.5D modelling approach. (a) Assembly and boundary conditions for the micro-extrusion simulation. (b-c) RVE for fine-grained material with 1:1 grain morphology based on EBSD data. (d) Inverse pole figure (IPF) color map representing the grain orientation distribution consistent with EBSD results.

6.4 Results and discussion

6.4.1 Compressive stress-strain curves

The crystal plasticity model effectively simulated the mechanical response of materials with varying grain sizes under compression, with simulated stress-strain curves (Fig. 6.5) aligning closely with experimental results. Yield stress was found to correlate directly with initial slip resistance, increasing as this parameter rose, while post-yield strain hardening behaviour depended on both the initial hardening rate and saturated slip resistance across slip systems. Notably, true strain increased as grain size decreased, consistent with the grain SE observed in micro/meso-scale materials. This phenomenon stems from finer grains accumulating higher densities of GNDs at boundaries, which impede dislocation motion and amplify strain hardening, thereby elevating flow stress. The results validate the model's capability to capture microstructure-property relationships, particularly the role of GNDs in mediating grain size-dependent deformation, and underscore the critical influence of grain boundaries on mechanical behaviour—essential for designing microformed components with tailored performance. This effect is further supported by studies on copper [94], steel [193], and titanium alloys [194], where finer grains demonstrate enhanced strength and strain hardening capabilities, primarily attributed to the elevated resistance encountered by dislocations during deformation. The results also highlight the importance of accurately capturing the initial grain orientation and morphology using EBSD data. This ensures that the simulated microstructure closely matches the experimental conditions, thereby improving the reliability of the simulation results.

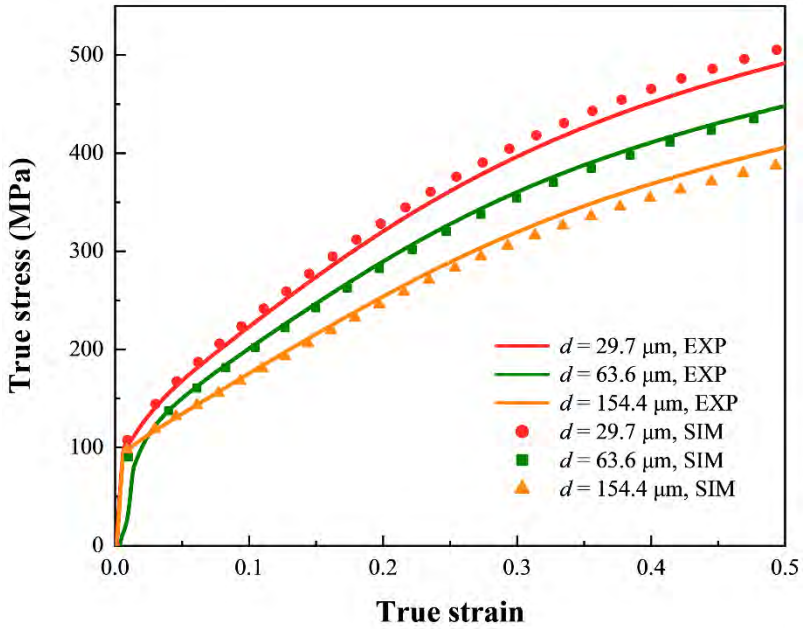

Fig. 6.5 Stress-strain curves obtained from compression tests and simulations for materials with different grain sizes. The curves demonstrate a high degree of consistency between experimental and simulated results, highlighting the accuracy of the calibrated crystal plasticity model.

Fig. 6.6 presents the stress and strain distribution maps obtained from CPFEM simulations of compression tests. These maps provide valuable insights into the deformation mechanisms at the microscale. Fig. 6.6 (a) shows the Mises stress distribution map, which highlights regions of stress concentration. At the microscale, stress concentration typically indicates areas where plastic deformation is likely to initiate first. In this study, high stress is observed at grain boundaries, particularly at the four corners and the central region of the material interface. This pattern can be attributed to the geometric discontinuities and the complex interaction between grains during compression. Grain boundaries, especially triple junctions and corners, act as stress concentrators due to their inherent structural complexity and the mismatch in deformation mechanisms between adjacent grains. Fig. 6.6 (b) illustrates the equivalent strain distribution map, revealing that strain concentration regions differ

slightly from high-stress areas. This discrepancy arises because strain accumulation depends not only on stress but also on the material's resistance to deformation, which varies across slip systems. Additionally, the strain distribution is affected by the initial grain orientation and morphology, as captured by the EBSD data used in the simulation. Under the same colormap legend, the low-strain area decreases with larger grain size, attributed to grain SE: reduced grain boundary influence in coarser grains promotes more uniform deformation. Low-strain regions are predominantly located near the surface layers, such as the top, bottom, and sides of the material. This results in a central region with higher strain, forming an "X" pattern. This pattern suggests that the material experiences higher compressive forces and more complex interactions between grains in this region. The findings from the CPFEM simulations are consistent with previous studies on the deformation behaviour of polycrystalline materials, highlighting the importance of grain size and grain boundary interactions in determining the mechanical response. The calibrated crystal plasticity model thus provides a robust framework for predicting deformation mechanisms and identifying microstructure evolution in materials with varying grain sizes under micro-extrusion.

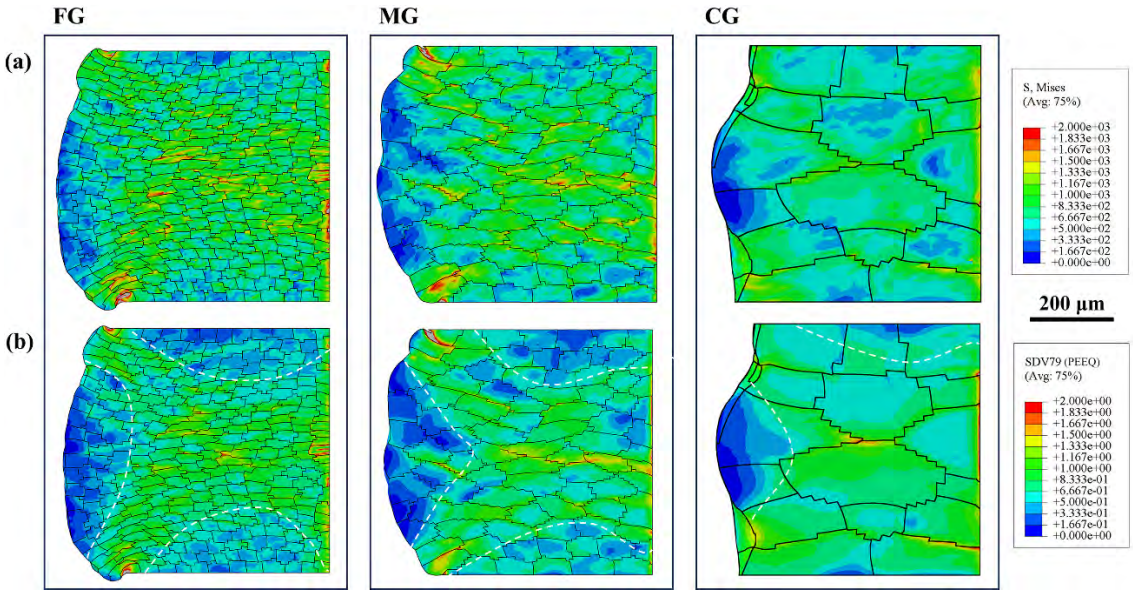

Fig. 6.6 Stress and strain distribution maps obtained from CPFEM simulations of

compression tests. (a) Stress distribution highlighting regions of stress concentration. High stress is observed at grain boundaries due to geometric discontinuities and the mismatch in deformation mechanisms between adjacent grains. (b) Equivalent strain distribution map. Low-strain regions decrease with increasing grain size, concentrating near the surface layers and forming an "X" pattern in the central region, indicative of deformation localization.

6.4.2 Analysis of quasi-in-situ EBSD results in micro-extrusion

6.4.2.1 Grain morphology evolution

In the micro-extrusion process, significant material deformation leads to substantial evolution in the microstructure, particularly in grain morphology. Figs. 6.7-6.9 illustrate the grain morphology and grain size changes observed by EBSD for materials with different initial grain sizes at 0%, 50%, and 100% extrusion stages.

Fig. 6.7 (a) shows the grain morphology evolution of the FG material during micro-extrusion. Initially, the material has a relatively uniform grain structure with an average grain size of 29.7 μm. As extrusion progresses to 50%, the lower half of the material forms a trapezoidal shape due to the transition zone connecting the initial and extrusion channels in the die design. By the end of the extrusion process (100%), the material below the transition zone is fully extruded into a 0.5 mm diameter channel, forming the extrudate. Fig. 6.7 (b) presents the grain size distribution changes during extrusion. The EBSD analysis reveals significant grain refinement, with an increase in grain count and a decrease in average grain size. Initially, grains smaller than 20 μm account for only 43.8% of the total grains. As extrusion progresses, this fraction increases to 73.0% at 50% extrusion and 87.7% at 100% extrusion. This trend is attributed to the dynamic recrystallization and sub-grain formation during deformation.

Larger grains, initially present in the range of 40-80 μm, are significantly fragmented, with virtually merely no grains larger than 40 μm remaining after full extrusion. The average grain size decreases from 29.7 to 17.5 μm at 50% extrusion and further to 12.5 μm at 100% extrusion. The observed grain refinement is consistent with the Hall-Petch effect, which suggests that smaller grains enhance material strength by increasing dislocation density and impeding dislocation movement. However, the grain size reduction does not continue indefinitely, as further refinement would require multiple deformation passes, such as in the Equal Channel Angular Pressing (ECAP) process. The substantial increase in grain count (by a factor of 5) after extrusion indicates significant sub-grain formation. However, this does not necessarily imply the presence of numerous fine grains, as EBSD may interpret sub-grains or fine twins as separate grains. The grain morphology changes observed by EBSD highlight the localized deformation behaviour during micro-extrusion. The fragmented grains and the formation of sub-grains indicate that deformation is concentrated in specific regions, particularly near grain boundaries and within larger grains. This localized deformation leads to strain hardening and grain refinement, which are essential for understanding the mechanical behaviour of materials under severe plastic deformation.

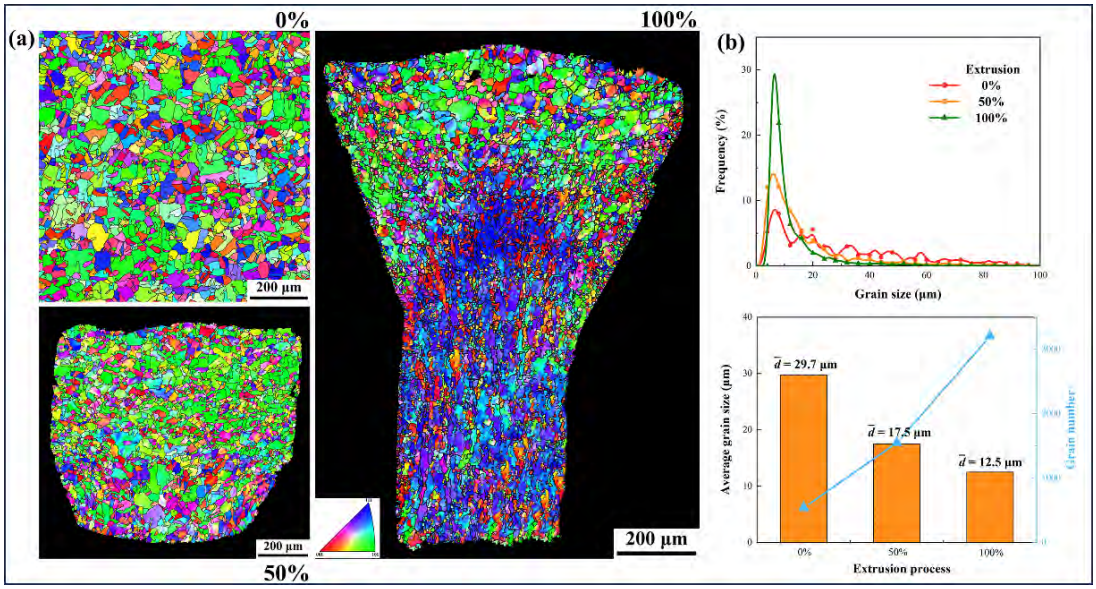

Fig. 6.7 Grain morphology evolution and grain size distribution of fine-grained (FG) material during micro-extrusion observed by EBSD. (a) Grain morphology at 0%, 50%, and 100% extrusion stages, showing significant deformation and grain refinement. (b) Grain size distribution changes during extrusion, highlighting the increase in small grains (<20 μm) and the fragmentation of larger grains. The average grain size decreases from 29.7 μm to 12.5 μm.

By comparing the materials with different initial grain sizes in Figs. 6.7-6.9, several notable grain SEs are observed during the micro-extrusion process. These effects provide valuable insights into the deformation behaviour and microstructural evolution of materials under severe plastic deformation. The extrudate length of FG material is slightly longer than that of MG material. This difference can be attributed to two main factors. First, the FG material exhibits more extensive grain fragmentation in the extrudate region, while many grains in the MG material are elongated axially without significant fragmentation. This suggests that larger grains act as barriers to whole deformation, limiting the material's ability to flow uniformly. Second, the surface layer grains in the FG material have a smaller area of grains in contact with

the die compared to those in the MG material. Despite the use of lubricating oil, friction still affects the material flow. The larger area of grains in contact with the die in the MG material generates more upward frictional forces, restricting the downward flow of material.

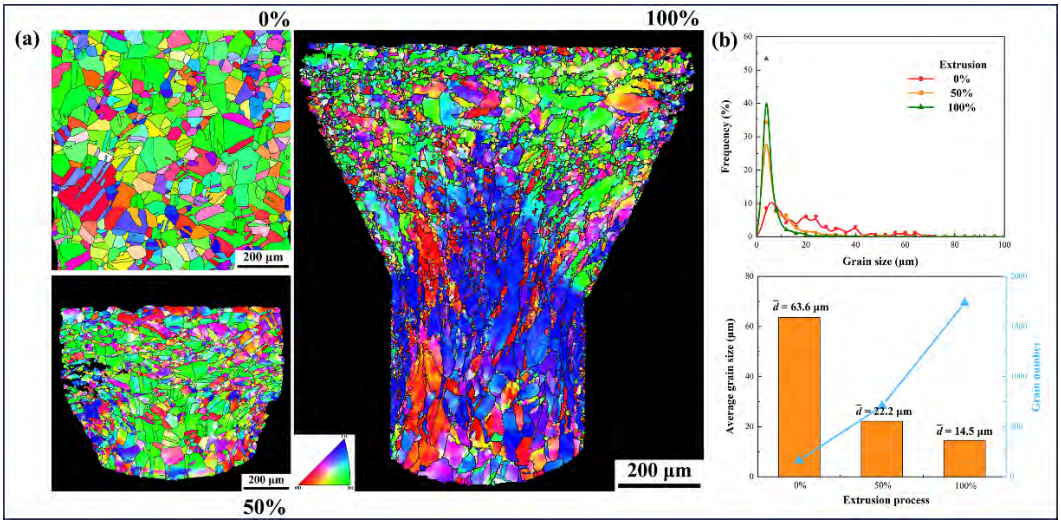

Fig. 6.8 Grain morphology evolution and grain size distribution of medium-grained (MG) material during micro-extrusion observed by EBSD. (a) Grain morphology at 0%, 50%, and 100% extrusion stages. (b) Grain size distribution changes during extrusion.

As shown in Figs. 6.7-6.9 (b), the fraction of grains in the smallest size range (0-10% of max grain size) increases with grain size during deformation, indicating that larger grains are more prone to fragmentation, with newly formed grain sizes largely independent of the original size. This fragmentation is driven by high strain gradients and dislocation density, leading to sub-grain formation and dynamic recrystallization, consistent with prior studies where larger grains fragment under severe plastic deformation. The FG material's average grain size decreases to 42.1% of its initial value, compared to 22.8% (MG) and 19.1% (CG), showing CG materials undergo

more effective microstructure refinement. While final grain size still correlates with initial size, the narrowing difference highlights CG's superior refinement efficiency due to higher strain accumulation capacity. This aligns with the Hall-Petch effect, where smaller grains enhance strength via dislocation density and motion resistance. The observed grain SEs highlight the importance of initial grain size in determining the deformation behaviour and microstructural evolution during micro-extrusion. These findings provide a foundation for optimizing micro-extrusion processes to achieve the desired mechanical properties and microstructures in materials with varying initial grain sizes.

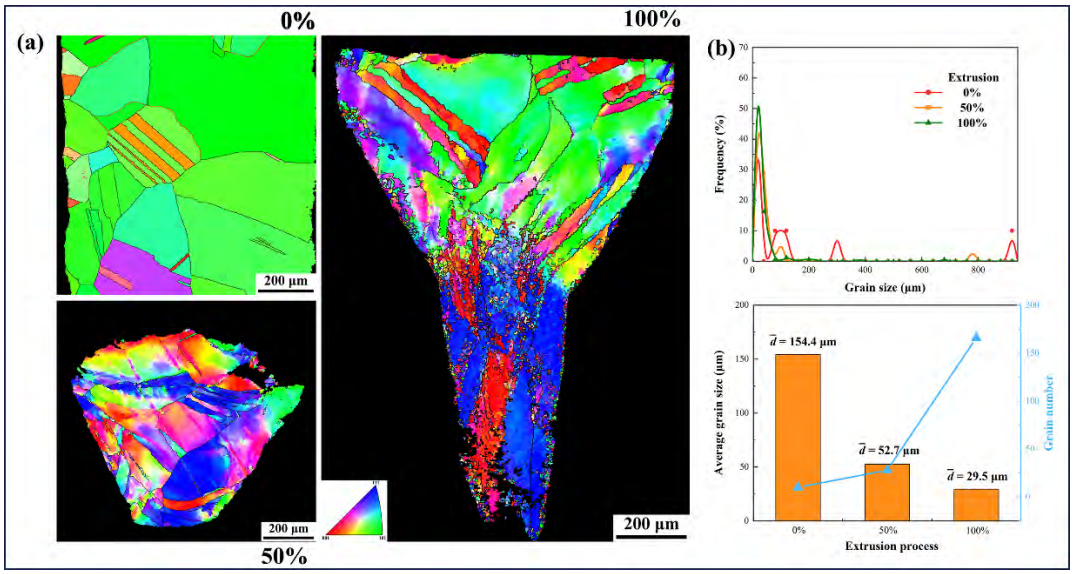

Fig. 6.9 Grain morphology evolution and grain size distribution of coarse-grained (CG) material during micro-extrusion observed by EBSD. (a) Grain morphology at 0%, 50%, and 100% extrusion stages. (b) Grain size distribution changes during extrusion.

6.4.2.2 Grain orientations evolution

The phenomenon of grains aligning and arranging along specific directions, leading

to non-uniform statistical distribution, is known as preferred orientation or texture. Plastic deformation can significantly alter grain orientations and, consequently, the texture of the material. The evolution of crystalline orientation during micro-extrusion is illustrated in Figs. 6.10-6.12. Fig. 6.10 shows the PFs of the FG material at 0%, 50%, and 100% extrusion stages. Initially, the grain orientations are relatively uniformly distributed. However, as extrusion progresses to 50%, the orientations begin to concentrate, with a notable pole forming near the centre of the {111} PF. Additionally, two other regions of orientation concentration emerge. This trend is more intuitively observed in Fig. 6.7 (a), where the blue regions (indicating specific orientations) become increasingly prominent in the transition zone and extrudate. As a result, the {111} planes of most grains become parallel to the sample surface. The maximum texture intensity of the {111} pole reaches approximately 2.6 times that of a random orientation distribution. Upon completion of extrusion, a single pole is observed at the north pole of the {111} PF, with the maximum texture intensity increasing to 4.2 times that of the random orientation distribution. This indicates a significant convergence in grain orientation as the material is extruded. The observed texture development is consistent with previous studies on severe plastic deformation processes, where grain orientations tend to align with the deformation direction to accommodate strain [195].

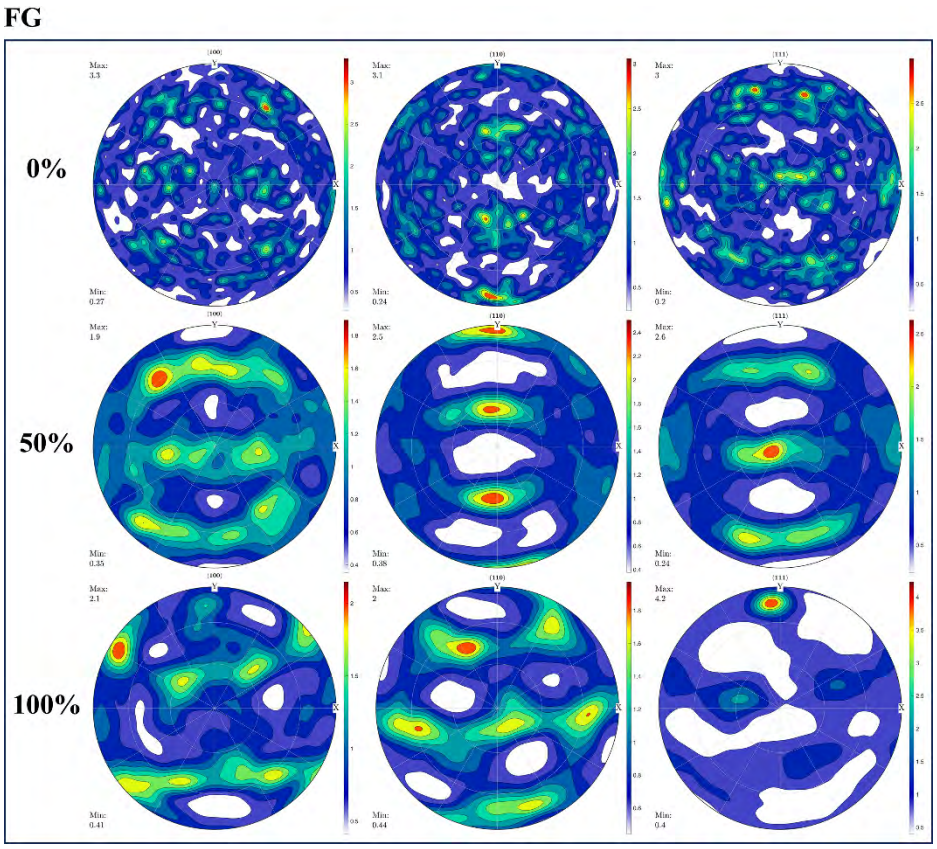

Fig. 6.10 Evolution of grain orientation distribution in FG material during micro-extrusion, as observed by EBSD. PFs show the grain orientation changes at 0%, 50%, and 100% extrusion stages. Initially, grain orientations are relatively uniform, but as deformation progresses, orientations begin to concentrate. At 50% extrusion, a distinct pole forms near the centre of the {111} pole figure, with additional regions of orientation concentration emerging. By 100% extrusion, the {111} pole converges towards the extrusion direction (ED), with a maximum texture intensity of 4.2 times that of a random orientation distribution.

The evolution of texture during micro-extrusion can be attributed to several mechanisms. First, the high strain gradients during deformation lead to lattice reorientation, where grains with orientations favourable for slip and deformation are more likely to deform plastically. This results in alignment of crystallographic planes

parallel to the deformation plane. Second, grain boundary migration driven by curvature and dislocation energy contributes to texture development. As grains fragment and new grains form via dynamic recrystallization, their orientations adapt to the deformation environment. Initial grain size plays a key role: FG materials exhibit sharper textures due to higher stored energy and boundary density, while CG materials show weaker textures from lower stored energy and fragmentation-driven recrystallization. This is because smaller grains have higher dislocation densities and are more susceptible to deformation-driven reorientation. In contrast, larger grains may undergo more localized deformation without significant orientation changes, resulting in weaker texture development.

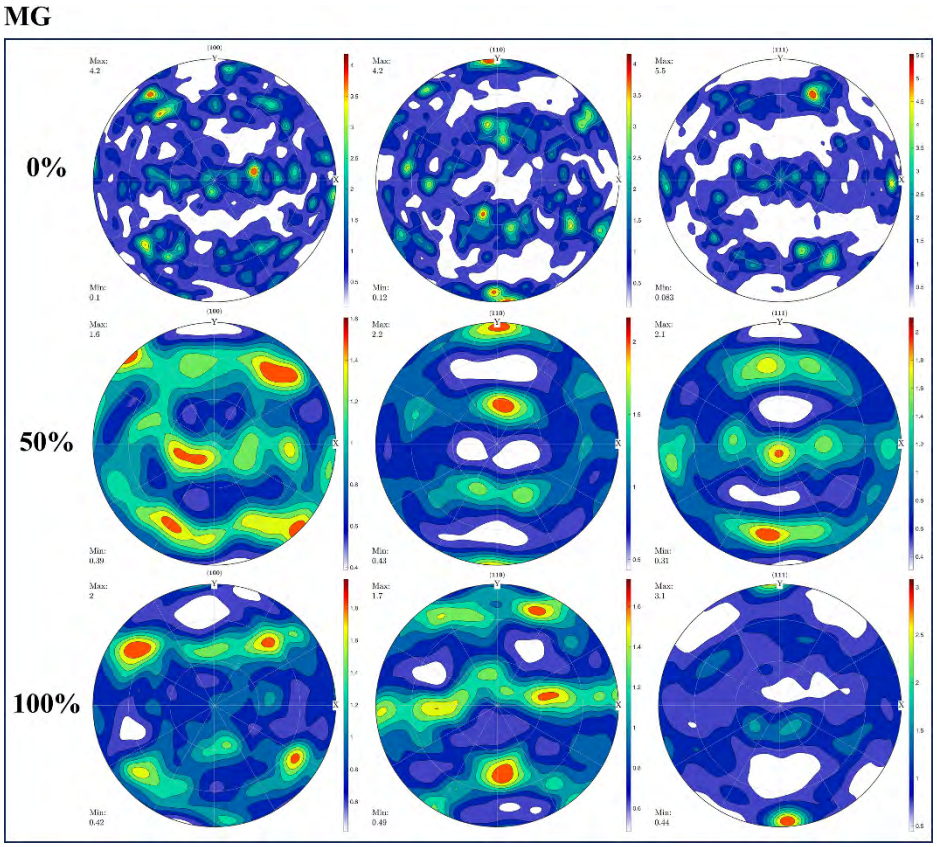

Fig. 6.11 Evolution of grain orientation distribution in MG material during micro-extrusion, as observed by EBSD. PFs show the grain orientation changes at 0%, 50%, and 100% extrusion stages.

By comparing the texture evolution in Figs. 6.10-6.12 for materials with different initial grain sizes, similar trends in grain orientation changes are observed. For example, in the {111} pole figure., three distinct orientation concentration regions emerge at 50% extrusion for all materials. By 100% extrusion, these orientations converge towards the poles (either the north or south pole), indicating a significant alignment of crystallographic planes parallel to the extrusion direction. However, differences arise in the CG material due to its fewer grain numbers compared to the other two. This scarcity of grains leads to more significant blank regions in the pole figure. and a higher degree of orientation concentration. Specifically, the maximum texture intensity in the CG material reaches 6.1, significantly higher than those observed in FG and MG materials. The higher texture intensity in the CG material can be attributed to several factors. First, fewer grains mean that each grain has a more significant volume fraction, making them more influential in the overall texture development. As these larger grains deform, they tend to align more uniformly along the extrusion direction, leading to a stronger texture. Second, the fewer grain boundaries in CG materials result in less complex interactions between grains, allowing for more pronounced orientation convergence. In contrast, FG and MG materials exhibit more uniform texture development due to their higher grain numbers and more complex grain boundary interactions. These interactions distribute the deformation more evenly, preventing the formation of extremely high texture intensities.

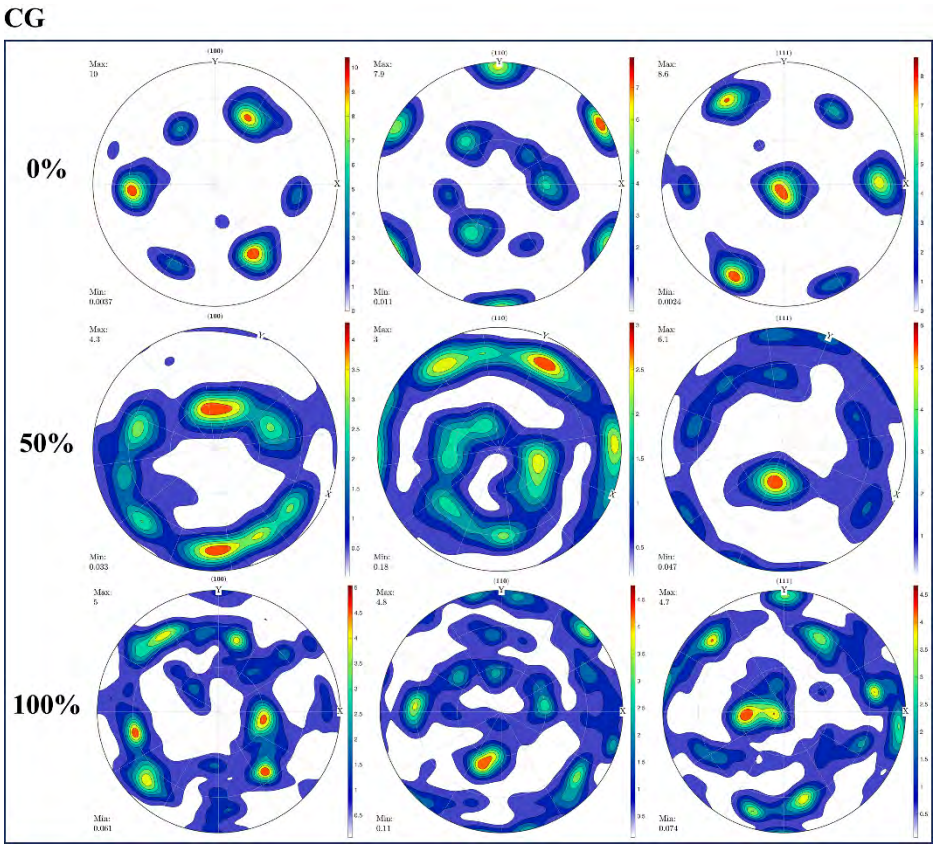

Fig. 6.12 Evolution of grain orientation distribution in CG material during micro-extrusion, as observed by EBSD. PFs show the grain orientation changes at 0%, 50%, and 100% extrusion stages.

6.4.2.3 KAM distribution evolution

Kernel Average Misorientation (KAM) is a measure of the local misorientation within grains, reflecting the distribution of GNDs in the material. KAM values are closely related to dislocation density, which in turn is influenced by deformation and strain distribution. Higher KAM values indicate greater internal strain and dislocation density, suggesting more significant deformation within the material. As shown in Fig. 6.13 (a-c), the KAM values increase with strain during micro-extrusion. This trend indicates that plastic deformation induces greater internal strain and dislocation density within each grain. For all grain sizes, the average KAM values rise as the

deformation progresses, highlighting the increasing complexity of deformation within the material. At 50% extrusion, a triangular region with low KAM values (<1°) appears in the central lower part of the material. This region corresponds to areas where deformation is less pronounced, due to the material's flow being constrained by the die geometry. This observation suggests that deformation is not uniformly distributed, with some regions experiencing more strain than others.

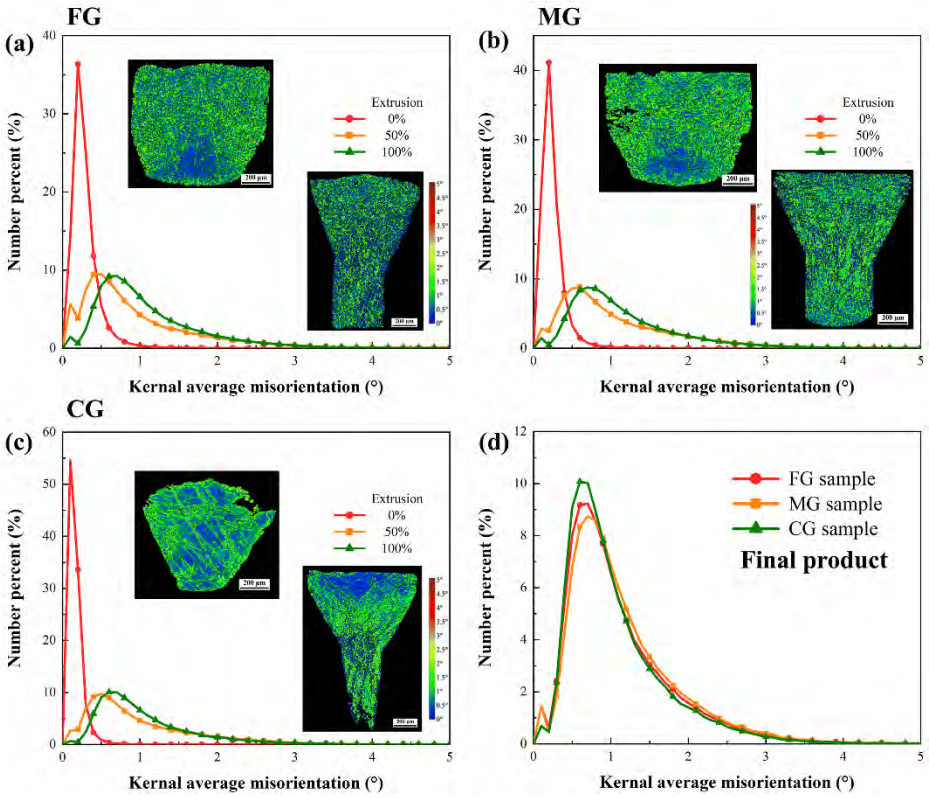

Fig. 6.13 Evolution of Kernel Average Misorientation (KAM) values during micro-extrusion. KAM distribution maps and values for (a) fine-grained, (b) medium-grained, and (c) coarse-grained material in micro-extrusion processes. (d) Statistical analysis of KAM values in the final extruded products. The average KAM values and their distribution are nearly identical across different grain sizes.

Initial undeformed materials exhibit lower KAM values, which decrease with larger grain sizes. This trend arises because larger grains possess fewer grain boundaries,

reducing barriers to dislocation motion. Consequently, larger grains tend to accumulate fewer dislocations under the same deformation conditions. In contrast, FG materials show a higher proportion of regions with very low KAM values (<0.2°). This phenomenon is particularly evident in FG materials, where smaller grains are "protected" by surrounding grains during deformation, resulting in minimal internal strain. The KAM maps reveal that FG materials have a more heterogeneous deformation distribution, with some grains experiencing significant deformation while others remain relatively undeformed. The final KAM values in the extruded products are summarized in Fig. 6.13 (d). The average KAM values and their distribution are nearly identical across different grain sizes, indicating that micro-extrusion effectively homogenizes the internal strain distribution. This result suggests that the micro-extrusion process can eliminate the initial differences in KAM values, leading to a more uniform deformation state in the final product.

6.4.3 Micro-stress and strain evolution and mechanism in micro-extrusion

The evolution of micro-stress and strain during micro-extrusion is shown in Fig. 6.14. Fig. 6.14 (b) (CPFEM-simulated micro-stress) reveals high-stress concentrations at grain boundaries in the extruded region at 50% extrusion, reflecting stress heterogeneity caused by grain boundaries impeding dislocation motion. Fig. 6.14 (a) (equivalent plastic strain) demonstrates strain nucleation at grain boundaries, with strain heterogeneity intensifying as deformation progresses, indicating pronounced strain localization. For the extrudate, strain decreases from the sides in contact with the die towards the centre. This trend is observable from the grain morphology in the simulation results, where grains narrow from the centre to the sides, especially in FG and MG materials. This phenomenon suggests that grains closer to the die experience greater deformation due to higher compressive forces.

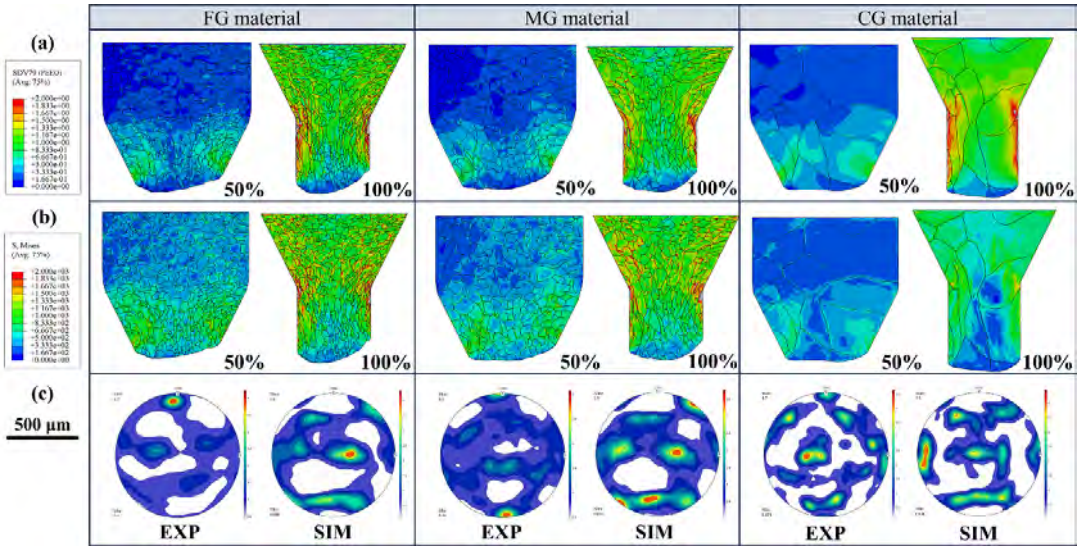

Fig. 6.14 Evolution of micro-stress and strain during micro-extrusion. (a) Equivalent plastic strain distribution at 50%, and 100% extrusion stages for various grain sizes. (b) Micro-stress distribution at 50%, and 100% extrusion stages for various grain sizes. (c) Comparison of the grain orientations distribution between EBSD and CPFEM simulations.

Since the length-to-diameter ratio of the extrudate in this study is not large, distinct trends are observed in the axial direction. To investigate this, three points along the transverse direction (P2, P4, P5) and three points along the axial direction (P1, P2, P3) were selected for FG material to track stress paths and explore the heterogeneity of material deformation during micro-extrusion, as shown in Fig. 6.15 (a). It should be noted that the stress data obtained at each point represent the average of three nearby points. Fig. 6.15 (b) shows the stress paths for axial points P1, P2, and P3. P3, located at the centre of the lower edge of the material, experiences stress activation earliest (10%) due to initial contact with the transition channel during extrusion. This region undergoes inward compression, and frictional forces restrict the downward movement of grains, leading to early lateral stress on P3. By 50% extrusion, P3 and its

neighbouring grains have entered the extrusion channel, and subsequent downward movement is less influenced by lateral compression, resulting in minimal stress increase. In contrast, P2 and P1 continue to experience axial and lateral compressive forces, leading to a steady rise in micro-stress. Notably, the micro-stress at P1 exceeds that at P2 at 60%, indicating that P2 is about to enter the extrusion channel, relieving lateral pressure. Fig. 6.15 (c) shows the stress paths for transverse points P2, P4, and P5. Stress generally increases from the centre outward, consistent with the mechanism that grains closer to the die experience greater deformation. Unlike the relatively stable stress path at P2, P4 and P5 exhibit significant stress fluctuations after entering the extrusion channel at different times. These fluctuations are attributed to changes in the direction and magnitude of compressive forces as these grains enter the channel.

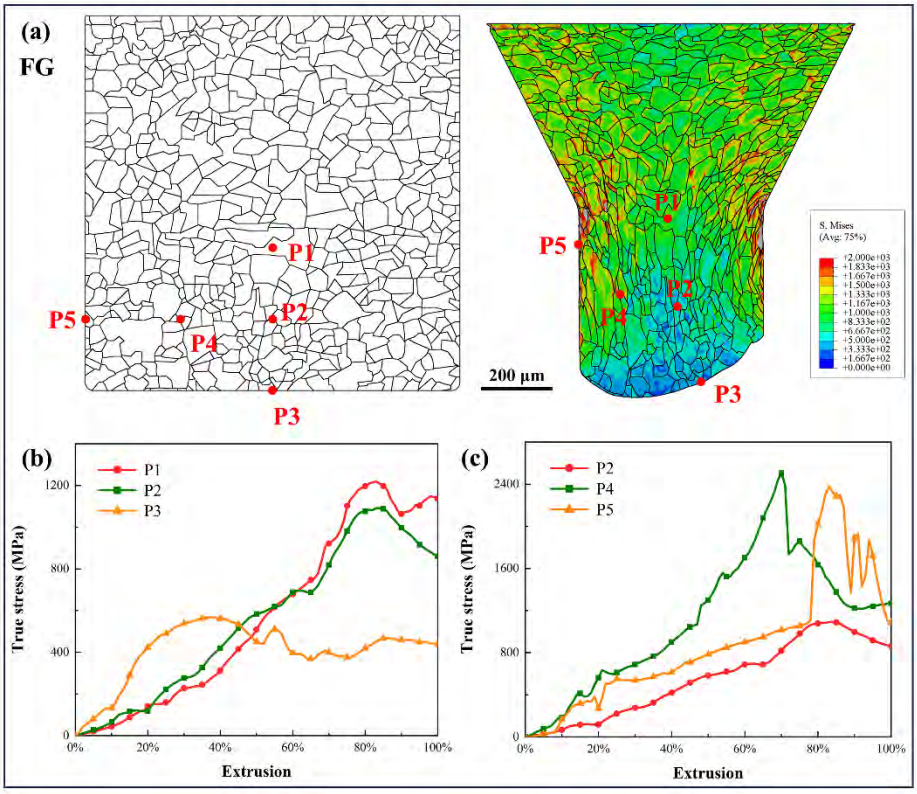

Fig. 6.15 Stress path analysis during micro-extrusion. (a) Schematic illustration of selected points for stress tracking: transverse points (P2, P4, P5) and axial points

(P1, P2, P3). (b) Stress paths for axial points P1, P2, and P3. P3, located at the centre of the lower edge, experiences early stress activation due to initial contact with the transition channel. Stress at P1 exceeds P2 at 60% extrusion, indicating relief of lateral pressure as P2 enters the extrusion channel. (c) Stress paths for transverse points P2, P4, and P5. Stress increases from the centre outward, with significant fluctuations at P4 and P5 as they enter the extrusion channel at different times.

6.4.4 Microstructure evolution in micro-extrusion

By integrating EBSD and CPFEM results (Fig. 6.16), the microstructural evolution of FG material during extrusion is systematically analysed. The CPFEM-derived equivalent plastic strain maps and grain boundary distributions, combined with EBSD orientation maps, reveal two shear bands along the extrudate sides—regions of intense plastic deformation, grain fragmentation, and material flow. These bands correlate with high-strain zones in simulations and EBSD-observed fragmented grains. Additionally, two dead metal zones (DMZs) are identified: the first in the extrudate centre, characterized by larger grains and lower strain due to minimal deformation, and the second at the extrudate base, where coarse grains and minimal strain reflect restricted material flow. CPFEM simulations align with EBSD data, demonstrating how grain boundaries (barriers to dislocation motion) drive strain localization and grain refinement in shear bands. The results highlight the interplay between grain size, strain heterogeneity, and deformation constraints, with FG materials exhibiting pronounced shear band refinement and DMZ formation due to higher grain boundary density and dislocation accumulation. Grains in this region exhibit two characteristics: (1) lateral deformation is less pronounced compared to the material on the sides, while longitudinal deformation is significant, and (2) strain accumulation is relatively low. The second DMZ is situated at the very bottom of the material, marked by the blue

regions in the strain map. This region undergoes minimal deformation, as evidenced by the minimal changes in grain structure and the lowest strain accumulation. Once this part of the material enters the extrusion channel, it experiences almost no further deformation.

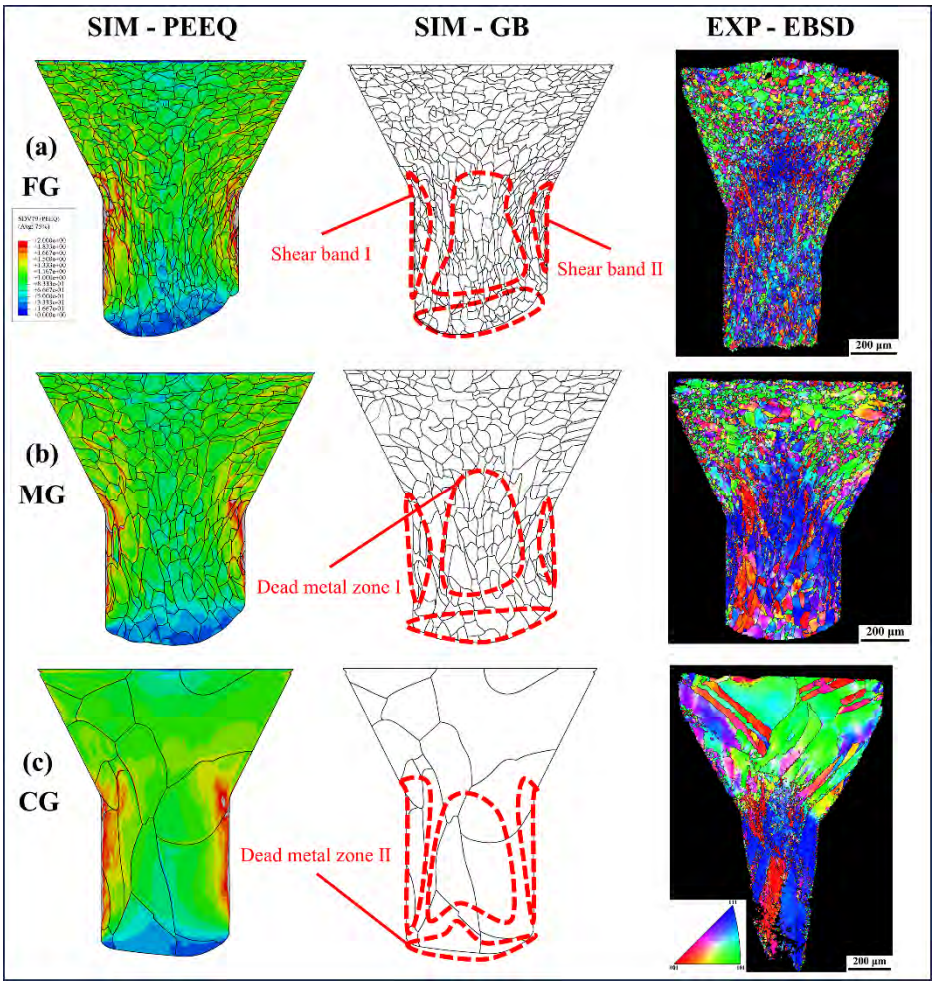

Fig. 6.16 EBSD and CPFEM results for (a) fine-grained, (b) medium-grained, and (c) coarse-grained material. An equivalent plastic strain map from CPFEM simulation shows two distinct shear bands on the sides of the extrudate, which are characterized by high strain accumulation and grain refinement. Grain boundary distribution map highlights the smaller grain sizes within the shear bands due to intense deformation. (c) The orientation distribution map from EBSD showing fragmented grains within the shear bands. Two DMZs were found in the central and

lower regions of the extrudate, where deformation is minimal.

By comparing simulation and experimental results across grain sizes, several grain SEs on microstructural evolution are identified: FG materials exhibit higher stress due to increased grain boundary density impeding dislocation motion, yet equivalent plastic strain maps reveal that the two shear bands with high strain accumulation intensify with coarser grains (CG > MG > FG), as reduced grain boundary interactions in larger grains promote localized deformation. Concurrently, DMZ size decreases with increasing grain size, attributed to longer-range strain transmission in CG materials where fewer grains enable persistent interactions, distributing deformation more uniformly and shrinking DMZs—reflecting enhanced strain homogeneity in coarser-grained materials.

To further investigate the mechanisms of microstructural evolution in the extrudate, several points were selected for position tracking during micro-extrusion, as illustrated in Figs. 6.17 and 6.18. The selected points ultimately reside within the extrudate. Initially, 27 points were distributed along three equidistant horizontal lines (L1, L2, and L3), with nine points evenly spaced along each line, as shown in Fig. 6.17. The relative positions of each point with respect to its neighbours were tracked to determine the deformation behaviour and microstructural evolution within different regions of the material. For FG material, at 50% extrusion, the points on the sides of L3 lag behind the downward movement of other points due to friction and lateral compression. This results in a complex bending of L2, characterized by rapid downward movement of the central points and slower movement of the points near the sides. Upon completion of extrusion, the central point on L1 has just entered the extrusion channel, while the points towards the sides are progressively higher. L2 exhibits a similar trend, with the outermost points located at the interface between the

extrudate and the remaining material. L3 shows a more pronounced downward convex curvature, with the outer five points in contact with the die and the central points forming an arc.

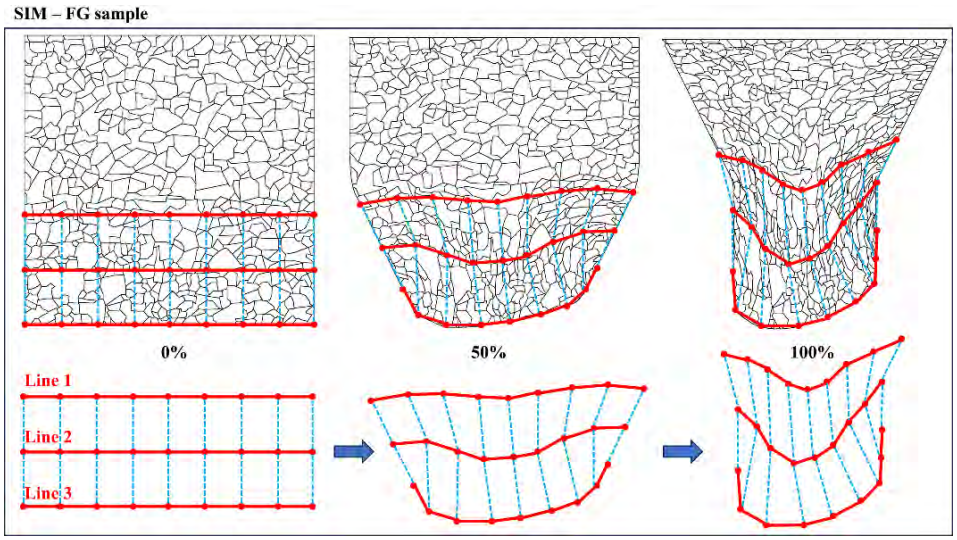

Fig. 6.17 Schematic illustration of the initial point distribution for tracking microstructural evolution during micro-extrusion. The initial configuration of 27 points distributed along three equidistant horizontal lines (L1, L2, and L3). The points are used to monitor deformation behaviour and microstructural changes in different regions of the extrudate. Evolution of point positions during micro-extrusion for FG material.

Fig. 6.18 presents the relative position changes of the 27 points in MG and CG materials. Comparing the position maps across different grain sizes reveals that the downward curvature of the lines increases with decreasing grain size, resulting in longer extrudate lengths. This trend is consistent with the observation that smaller grains experience more localized deformation and higher strain accumulation. The deformation behaviour can be categorized into three distinct zones: the interior zone (IZ), the transition zone (TZ), and the surface zone (SZ). In the IZ, material experiences significant longitudinal stretching but minimal lateral compression, which

is where the dead metal zone (DMZ) is primarily located. The TZ exhibits similar longitudinal stretching to the IZ but undergoes more severe lateral compression and some degree of rotation. The SZ, located at the outermost region, experiences the least longitudinal stretching, the most severe lateral compression, and the most significant rotation. These regional deformation characteristics are attributed to the interplay between grain size and deformation mechanisms. Smaller grains in FG material facilitate more localized deformation and higher strain gradients, leading to more pronounced bending and longer extrudate lengths. In contrast, larger grains in CG material result in more uniform deformation and reduced strain localization, leading to shorter extrudate lengths and smaller DMZs. This behaviour aligns with previous discussions on microstructural evolution during severe plastic deformation, highlighting the significant role of grain size in influencing deformation mechanisms and microstructural evolution

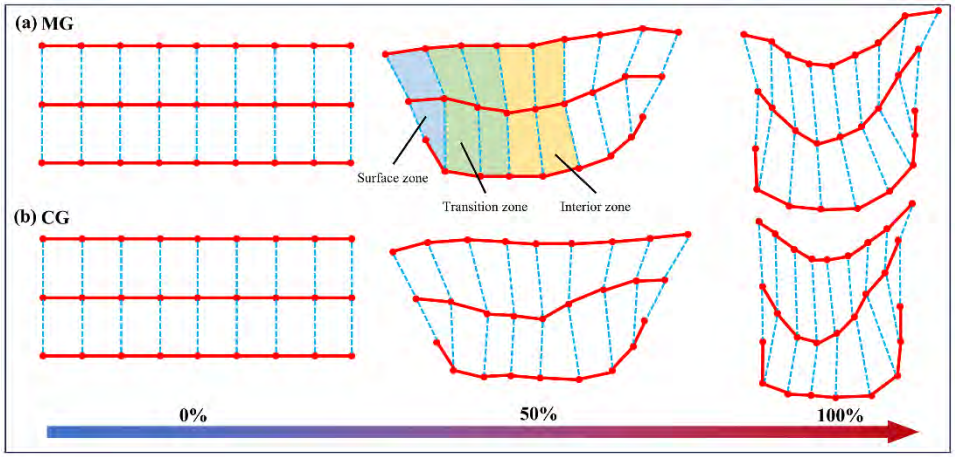

Fig. 6.18 Evolution of point positions during micro-extrusion for MG and CG materials.

6.5 Summary

This chapter innovatively integrates quasi-in-situ EBSD and CPFEM simulations to investigate microstructural evolution and deformation mechanisms during micro-

extrusion. The combined approach provides a comprehensive understanding of the relationship between grain size, deformation behaviour, and microstructural changes under severe plastic deformation. The key findings are summarized as follows:

1) The integration of quasi-in-situ EBSD and CPFEM offers a novel framework for analyzing microstructural evolution, enabling real-time tracking of grain orientation and deformation behaviour. However, CPFEM has inherent limitations, including computational cost at high mesh resolutions and challenges in accurately capturing dynamic recrystallization and grain boundary sliding mechanisms.
2) FG materials exhibit stronger strain localization and less grain refinement than MG and CG materials due to higher dislocation density and grain boundary interactions. While CPFEM effectively captures dislocation-based hardening, it may not fully account for size effects at extremely fine grain scales (<1 μm), where additional mechanisms become dominant.
3) FG materials show more pronounced texture evolution, indicating higher susceptibility to deformation-induced reorientation. The heterogeneous distribution of plastic strain and stress aligns with experimental observations, but CPFEM's reliance on crystal plasticity constitutive laws may oversimplify local stress states near grain boundaries, where experimental uncertainties (e.g., residual stresses) play a significant role.
4) High stress/strain concentrations at grain boundaries and die-contact regions are well-predicted, but CPFEM's assumption of idealized grain morphologies may not fully replicate real microstructural complexities, such as irregular grain shapes and non-uniform grain boundary properties.

This study highlights the critical role of grain size in micro-extrusion deformation behaviour while acknowledging CPFEM's limitations in capturing ultra-fine-grained

effects and complex grain boundary phenomena. Future work should incorporate advanced constitutive models (e.g., phase-field or discrete dislocation dynamics) to improve predictions at smaller length scales. Despite these limitations, the CPFEM-EBSD framework provides valuable insights for optimizing micro-extrusion processes, enhancing material performance, and guiding further research in meso/micro-forming.

Chapter 7 Conclusions and future research

7.1 Conclusions

This thesis establishes that size effects in meso/micro-forming arise not merely from geometric scaling but from fundamental competitions between constrained surface grains and interior grains, slip versus twinning deformation modes, and variations in initial crystallographic textures. Through integrated CPFEM-EBSD analysis of progressive forming processes, we demonstrate that surface grains impose mechanical constraints on interior grain displacement, amplifying strain heterogeneity and directly governing cavity-filling efficiency and dimensional accuracy. These multi-axial interactions explain why conventional scaling laws fail to predict anomalies like thickness reduction scatter or load-grain size inversion observed in micro-deep drawing and extrusion.

The developed CPFEM-CZM framework successfully normalizes these size effects across diverse geometries—from micro-embossed features to hexagonal sockets and gear shafts—by embedding crystal plasticity theory into its constitutive foundation. This approach eliminates the need for empirical re-verification of size effects for geometrically similar components, as simulations intrinsically capture texture-driven anisotropy and grain-boundary interactions. Validated against tensile tests and in-situ EBSD data, the framework predicts grain-size-dependent forming loads within 8% error and thickness distribution trends with 90% accuracy, establishing a universal computational basis for microstructure-sensitive process design.

Quantitative comparisons reveal CPFEM’s supremacy over conventional FEM in predicting size-effect phenomena. Where conventional FEM ignores grain-level

heterogeneity, CPFEM resolves dead metal zones, shear band formation, and texture evolution correlated with EBSD observations. However, this fidelity incurs extreme computational costs—simulations require 100× more resources than coupled Eulerian-Lagrangian (CEL) methods—limiting industrial deployment. Crucially, CEL emerges as a viable alternative for bulk deformation prediction, but only CPFEM captures the slip-twinning competitions and surface-interior grain interactions that define meso/micro-forming quality.

Limitations persist in modelling ultra-fine grains (<1 μm) where dynamic recrystallization and non-ideal grain boundaries dominate. Our quasi-in-situ EBSD studies confirm CPFEM's underestimation of residual stresses near grain boundaries in fine-grained materials, reflecting oversimplified boundary conditions. Future work must integrate phase-field dislocation dynamics and machine learning-calibrated hardening laws to address these gaps. Nevertheless, the demonstrated normalization of size effects through crystal plasticity theory provides a transformative pathway toward generalized predictive models.

This thesis redefines size-effect management in precision manufacturing: rather than treating each component as unique, engineers can leverage this CPFEM framework to derive microstructure-informed forming guidelines for entire geometric families. This thesis shifts meso/micro-forming theory from phenomenological scaling to microstructure-driven predictability. By unifying texture, grain constraints, and deformation competitions into a scalable simulation paradigm, we enable targeted optimization of die design, grain size selection, and process parameters—accelerating the industrial adoption of meso/micro-forming technologies for high-value applications.

7.2 Suggestions for future research

1) Computational efficiency enhancement

To broaden CPFEM's applicability in industrial settings, future research should prioritize enhancing its computational efficiency. This can be achieved through the development of more efficient algorithms that leverage parallel computing architectures, enabling the distribution of computational tasks across multiple processors or clusters. Additionally, exploring simplified models or surrogate models that approximate CPFEM's accuracy with reduced computational overhead could be beneficial. These efforts would make CPFEM more accessible for real-time simulations and iterative design processes, facilitating its adoption in manufacturing industries where rapid prototyping and quick turnaround times are essential.

2) Integration with multi-physics models

The forming processes studied can be further enriched by integrating CPFEM with multi-physics models. For example, incorporating thermal models would allow the simulation of temperature-induced phase transformations and their impact on material behaviour during forming. Electrical and magnetic models could be relevant for electroplating or magnetic forming processes, where external fields influence material deformation. This multi-physics integration would expand CPFEM's scope to multi-functional material systems, enabling the simulation of coupled phenomena and opening avenues for innovative manufacturing techniques that combine forming with other physical processes.

3) Advanced fracture modelling

While the CPFE-CZM method has shown promise, further refinement of fracture

models within the CPFEM framework is necessary. This includes exploring more sophisticated damage mechanics and fracture criteria that can accurately predict material failure under diverse loading conditions and microstructural configurations. Incorporating microstructure-sensitive fracture models that consider grain boundary effects, precipitate distributions, and phase transformations would enhance the method's predictive capabilities. Such advancements are crucial for applications involving high-stress environments or brittle materials, where precise fracture prediction is vital for ensuring component reliability and safety.

4) Material database development

The successful application of CPFEM relies heavily on comprehensive material data. Future efforts should be directed towards building extensive databases of material properties, including crystallographic information, constitutive parameters, and texture data for various materials. Collaborative initiatives between academia and industry could facilitate data sharing and standardization, ensuring that the material databases are robust, reliable, and widely applicable. This resource would significantly enhance the accuracy and reliability of CPFEM simulations across different material systems, reducing the need for extensive experimental calibration for each new material.

5) Process optimization and control

The insights gained from CPFEM simulations can be leveraged for optimizing forming processes. Future research could involve developing automated optimization frameworks that utilize CPFEM predictions to determine optimal process parameters, tool geometries, and sequences. Machine learning techniques could be integrated to analyse simulation data and identify patterns that guide the optimization process. This

would enhance the quality and efficiency of micro and meso forming operations, minimizing material waste, reducing production costs, and improving overall manufacturing sustainability.

6) In-situ and real-time monitoring

Extending the quasi-in-situ EBSD approach to real-time monitoring during forming processes would provide continuous feedback for process control. This integration of experimental techniques with CPFEM simulations could enable dynamic adjustments based on real-time microstructural and deformation data, improving forming outcomes. Developing high-speed imaging and data processing techniques would be essential to achieve this, allowing for immediate analysis and response during the forming process. This capability would be particularly valuable in industries where material properties and part quality are highly sensitive to forming conditions.

References

[1] A.R. Razali, Y. Qin, A Review on Micro-manufacturing, Micro-forming and their Key Issues, Procedia Eng. 53 (2013) 665-672.

[2] F. Vollertsen, H. Schulze Niehoff, Z. Hu, State of the art in micro forming, Int. J. Mach. Tools Manuf. 46(11) (2006) 1172-1179.

[3] M. Geiger, M. Kleiner, R. Eckstein, N. Tiesler, U. Engel, Microforming, CIRP Ann. 50(2) (2001) 445-462.

[4] M.W. Fu, W.L. Chan, A review on the state-of-the-art microforming technologies, Int. J. Adv. Manuf. 67(9-12) (2012) 2411-2437.

[5] B. Venkatesh, S.K. Sahoo, S.K. Panigrahi, Micro-extrusion: A potential approach to micro-manufacture miniaturize magnesium metal matrix composite components, J. Manuf. Processes 131 (2024) 2473-2490.

[6] J.G. Liu, M.W. Fu, J. Lu, W.L. Chan, Influence of size effect on the springback of sheet metal foils in micro-bending, Comput. Mater. Sci 50(9) (2011) 2604-2614.

[7] Y. Saotome, K. Yasuda, H. Kaga, Microdeep drawability of very thin sheet steels, J. Mater. Process. Technol. 113(1-3) (2001) 641-647.

[8] B.Y. Joo, S.I. Oh, Y.K. Son, Forming of Micro Channels with Ultra Thin Metal Foils, CIRP Ann. 53(1) (2004) 243-246.

[9] I. Irthiea, G. Green, S. Hashim, A. Kriama, Experimental and numerical investigation on micro deep drawing process of stainless steel 304 foil using flexible tools, Int. J. Mach. Tools Manuf. 76 (2014) 21-33.

[10] X.M. Lai, M.W. Fu, L.F. Peng, Sheet Metal Meso-and Microforming and Their Industrial Applications, CRC Press2018.

[11] F. Vollertsen, Categories of size effects, Prod. Eng. 2(4) (2008) 377-383.

[12] F. Vollertsen, D. Biermann, H.N. Hansen, I.S. Jawahir, K. Kuzman, Size effects

in manufacturing of metallic components, CIRP Ann. 58(2) (2009) 566-587.

[13] P. Lorenzino, A. Navarro, Influence of the ratio between specimen thickness and grain size on the fatigue and tensile properties of plain and notched aluminium plate specimens, Int. J. Fatigue 164 (2022) 107149.

[14] S. Lei, Z. Xu, L. Peng, X. Lai, Effect of grain size on the ductile-brittle fracture behavior of commercially pure titanium sheet metals, Mater. Sci. Eng., A 822 (2021) 141630.

[15] B.B. Wang, G.M. Xie, L.H. Wu, P. Xue, D.R. Ni, B.L. Xiao, Y.D. Liu, Z.Y. Ma, Grain size effect on tensile deformation behaviors of pure aluminum, Mater. Sci. Eng., A 820 (2021) 141504.

[16] B. Meng, W.H. Wang, Y.Y. Zhang, M. Wan, Size effect on plastic anisotropy in microscale deformation of metal foil, J. Mater. Process. Technol. 271 (2019) 46-61.

[17] C. Wang, S. Xue, G. Chen, L. Cui, P. Zhang, Investigation on formability of bipolar plates during flexible micro forming of Cu/Ni clad foils, J. Manuf. Processes 53 (2020) 293-303.

[18] W.L. Chan, M.W. Fu, Meso-scaled progressive forming of bulk cylindrical and flanged parts using sheet metal, Mater. Des. 43 (2013) 249-257.

[19] M.W. Fu, W.L. Chan, Micro-scaled progressive forming of bulk micropart via directly using sheet metals, Mater. Des. 49 (2013) 774-783.

[20] B. Meng, M.W. Fu, C.M. Fu, K.S. Chen, Ductile fracture and deformation behavior in progressive microforming, Mater. Des. 83 (2015) 14-25.

[21] J.Y. Zheng, H.P. Yang, M.W. Fu, C. Ng, Study on size effect affected progressive microforming of conical flanged parts directly using sheet metals, J. Mater. Process. Technol. 272 (2019) 72-86.

[22] J.Y. Zheng, S.Q. Shi, M.W. Fu, Progressive microforming of pin-shaped plunger parts and the grain size effect on its forming quality, Mater. Des. 187 (2020).

[23] X.F. Tang, S.Q. Shi, M.W. Fu, Interactive effect of grain size and crystal structure on deformation behavior in progressive micro-scaled deformation of metallic

materials, Int. J. Mach. Tools Manuf. 148 (2020).

[24] E. Ghassemali, A.E.W. Jarfors, M.-J. Tan, S.C.V. Lim, On the microstructure of micro-pins manufactured by a novel progressive microforming process, Int. J. Mater. Form. 6(1) (2013) 65-74.

[25] R. Zhang, S. Lan, Z. Xu, D. Qiu, L. Peng, Investigation and optimization of the ultra-thin metallic bipolar plate multi-stage forming for proton exchange membrane fuel cell, J. Power Sources 484 (2021) 229298.

[26] X. Zhang, X. Lu, J. Zhao, Q. Kan, Z. Li, G. Kang, Temperature effect on tensile behavior of an interstitial high entropy alloy: Crystal plasticity modeling, Int. J. Plast. 150 (2022) 103201.

[27] A. Lakshmanan, J. Luo, I. Javaheri, V. Sundararaghavan, Three-dimensional crystal plasticity simulations using peridynamics theory and experimental comparison, Int. J. Plast. 142 (2021) 102991.

[28] X. Long, K. Chong, Y. Su, C. Chang, L. Zhao, Meso-scale low-cycle fatigue damage of polycrystalline nickel-based alloy by crystal plasticity finite element method, Int. J. Fatigue 175 (2023) 107778.

[29] N. Guo, J. Wang, C.Y. Sun, Y.F. Zhang, M.W. Fu, Analysis of size dependent earing evolution in micro deep drawing of TWIP steel by using crystal plasticity modeling, Int. J. Mech. Sci. 165 (2020) 105200.

[30] M. Kardan-Halvaei, M. Morovvati, B. Mollaei-Dariani, Crystal plasticity finite element simulation and experimental investigation of the micro-upsetting process of OFHC copper, J. Micromech. Microeng. 30(7) (2020) 075005.

[31] J.Y. Zheng, J.L. Wang, M.W. Fu, Experimental and numerical study of the size effect on compound Meso/ Microforming behaviors and performances for making bulk parts by directly using sheet metals, J. Manuf. Processes 66 (2021) 506-520.

[32] X. Tong, J.-Y. Zheng, M.W. Fu, Numerical and experimental study of the size effect on deformation behavior and quality of microembossed multi-channel structures, J. Manuf. Processes 78 (2022) 363-375.

[33] X. Tong, Y. Li, M.W. Fu, Modelling of grain size effects in progressive

microforming using CPFEM, Int. J. Mech. Sci. 267 (2024) 108971.

[34] U. Engel, R. Eckstein, Microforming—from basic research to its realization, J. Mater. Process. Technol. 125-126 (2002) 35-44.

[35] M. Elyasi, F.A. Khatir, M. Hosseinzadeh, Manufacturing metallic bipolar plate fuel cells through rubber pad forming process, Int. J. Adv. Manuf. 89(9) (2017) 3257-3269.

[36] H. Talebi-Ghadikolaee, M. Elyasi, M.J. Mirnia, Investigation of failure during rubber pad forming of metallic bipolar plates, Thin-Walled Structures 150 (2020) 106671.

[37] J. Xu, X. Wang, C. Wang, L. Yuan, W. Chen, J. Bao, Q. Su, Z. Xu, C. Wang, Z. Wang, A review on micro/nanoforming to fabricate 3D metallic structures, Adv. Mater. 33(6) (2021) 2000893.

[38] V. Jain, U. Dixit, C. Paul, A. Kumar, Micromanufacturing: a review—part II, Proceedings of the Institution of Mechanical Engineers, Part B: Journal of Engineering Manufacture 228(9) (2014) 995-1014.

[39] J. Wang, M. Fu, J. Ran, Analysis and avoidance of flow-induced defects in meso-forming process: simulation and experiment, Int. J. Adv. Manuf. 68 (2013) 1551-1564.

[40] Z. Yao, G.-Y. Kim, L. Faidley, Q. Zou, D. Mei, Z. Chen, Acoustic softening and hardening of aluminum in high-frequency vibration-assisted micro/meso forming, Mater. Manuf. Processes 28(5) (2013) 584-588.

[41] Y. Qin, Y. Ma, C. Harrison, A. Brockett, M. Zhou, J. Zhao, F. Law, A. Razali, R. Smith, J. Eguia, Development of a new machine system for the forming of micro-sheet-products, Int. J. Mater. Form. 1 (2008) 475-478.

[42] T. Koerner, L. Brown, R. Xie, R.D. Oleschuk, Epoxy resins as stamps for hot embossing of microstructures and microfluidic channels, "Sens. Actuators, B" 107(2) (2005) 632-639.

[43] R. Hajare, V. Reddy, R. Srikanth, MEMS based sensors–A comprehensive review of commonly used fabrication techniques, Mater. Today:. Proc. 49 (2022) 720-730.

[44] C. Motz, D. Weygand, J. Senger, P. Gumbsch, Micro-bending tests: A comparison between three-dimensional discrete dislocation dynamics simulations and experiments, Acta Mater. 56(9) (2008) 1942-1955.

[45] M. Matsuo, K. Abe, S. Suda, T. Matsunaga, Y. Haga, Micro hydraulic bending actuator for minimally invasive medical device, 2013 Transducers & Eurosensors XXVII: The 17th International Conference on Solid-State Sensors, Actuators and Microsystems (TRANSDUCERS & EUROSENSORS XXVII), IEEE, 2013, pp. 1440-1443.

[46] H.-T. Lee, H.-J. Kim, C.-S. Kim, K. Gomi, M. Taya, S. Nomura, S.-H. Ahn, Site-specific characterization of beetle horn shell with micromechanical bending test in focused ion beam system, Acta Biomater. 57 (2017) 395-403.

[47] G. Behrens, F. Trier, H. Tetzel, F. Vollertsen, Influence of tool geometry variations on the limiting drawing ratio in micro deep drawing, Int. J. Mater. Form. 9 (2016) 253-258.

[48] F. Vollertsen, Z. Hu, H.S. Niehoff, C. Theiler, State of the art in micro forming and investigations into micro deep drawing, J. Mater. Process. Technol. 151(1-3) (2004) 70-79.

[49] J. Xu, B. Guo, C. Wang, D. Shan, Blanking clearance and grain size effects on micro deformation behavior and fracture in micro-blanking of brass foil, Int. J. Mach. Tools Manuf. 60 (2012) 27-34.

[50] M. Fu, B. Yang, W.L. Chan, Experimental and simulation studies of micro blanking and deep drawing compound process using copper sheet, J. Mater. Process. Technol. 213(1) (2013) 101-110.

[51] P. Zhang, M.P. Pereira, B.F. Rolfe, D.E. Wilkosz, P. Hodgson, M. Weiss, Investigation of material failure in micro-stamping of metallic bipolar plates, J. Manuf. Processes 73 (2022) 54-66.

[52] Ú. Arinbjarnar, P. Schumann, J. Moske, A. Breunig, P. Groche, C.V. Nielsen, A review of methods and effects for improving production robustness in industrial micro-deep drawing, Int. J. Mater. Form. 17(3) (2024) 31.

[53] J. Xu, Q. Su, D. Shan, B. Guo, Sustainable micro-manufacturing of

superhydrophobic surface on ultrafine-grained pure aluminum substrate combining micro-embossing and surface modification, J. Cleaner Prod. 232 (2019) 705-712.

[54] W. Presz, Contact phenomena in micro-blanking, Int. J. Mater. Form. 1(1) (2008) 471-474.

[55] M. Arenoft, R. Solmer Ericsen, H. Norgaard Hansen, Micro-bulk-forming, Micro-Manufacturing Engineering and Technology (2010) 114-129.

[56] X. Chen, Z. Wang, J. Xu, Y. Wang, J. Li, H. Liu, Sustainable production of micro gears combining micro reciprocated wire electrical discharge machining and precision forging, J. Cleaner Prod. 188 (2018) 1-11.

[57] J. Xu, X. Zhu, L. Shi, D. Shan, B. Guo, T.G. Langdon, Micro-Forming Using Ultrafine-Grained Aluminum Processed by Equal-Channel Angular Pressing, Adv. Eng. Mater. 17(7) (2015) 1022-1033.

[58] B. Zhang, M. Dodaran, S. Ahmed, S. Shao, W. Meng, K. Juul, K. Nielsen, Grain-size affected mechanical response and deformation behavior in microscale reverse extrusion, Materialia 6 (2019) 100272.

[59] J. Zhao, M. Huo, X. Ma, F. Jia, Z. Jiang, Study on edge cracking of copper foils in micro rolling, Mater. Sci. Eng., A 747 (2019) 53-62.

[60] J. Han, W. Zheng, G. Wang, M. Yu, Experimental study on size effect of dry friction in meso/micro-upsetting process, Int. J. Adv. Manuf. 95 (2018) 1127-1133.

[61] Z. Yin, M. Yang, Investigation on Deformation Behavior in the Surface of Metal Foil with Ultrasonic Vibration-Assisted Micro-Forging, Materials 15(5) (2022) 1907.

[62] M. Ren, F. Lin, F. Jia, H. Xie, M. Yang, Z. Jiang, Micro rolling fabrication of copper/SS304L micro composite channels, J. Manuf. Processes 90 (2023) 1-13.

[63] T. Zhang, X. Wang, Q. Gong, Z. Shen, X. Hou, H. Liu, Mechanism and formability of micro-heading of metal rod by laser dynamic loading, Opt. Laser Technol. 148 (2022) 107732.

[64] Z. Yao, G.-Y. Kim, L. Faidley, Q. Zou, D. Mei, Z. Chen, Effects of superimposed high-frequency vibration on deformation of aluminum in micro/meso-scale upsetting,

J. Mater. Process. Technol. 212(3) (2012) 640-646.

[65] C. Bunget, G. Ngaile, Influence of ultrasonic vibration on micro-extrusion, Ultrasonics 51(5) (2011) 606-616.

[66] B. Taleb Araghi, A. Göttmann, M. Bambach, G. Hirt, G. Bergweiler, J. Diettrich, M. Steiners, A. Saeed-Akbari, Review on the development of a hybrid incremental sheet forming system for small batch sizes and individualized production, Prod. Eng. 5(4) (2011) 393-404.

[67] Y. Li, F. Liu, H. Yuan, X. Li, J. Li, G. Zhao, A novel micro-rolling & incremental sheet forming hybrid process: Deformation behavior and microstructure evolution, Chin. J. Aeronaut. 37(5) (2024) 603-622.

[68] B. Meng, M.W. Fu, C.M. Fu, J.L. Wang, Multivariable analysis of micro shearing process customized for progressive forming of micro-parts, Int. J. Mech. Sci. 93 (2015) 191-203.

[69] X. Zhao, H. Ou, A new hybrid stretch forming and double-layer two-point incremental sheet forming process, J. Mater. Res. Technol. 30 (2024) 3485-3509.

[70] Y. Wang, Z. Zheng, F. Zeng, M. Fu, Geometrical and microstructural size effects in progressive forming using wires, Int. J. Mech. Sci. 251 (2023) 108332.

[71] R. Zhao, J. Han, B. Liu, M. Wan, Interaction of forming temperature and grain size effect in micro/meso-scale plastic deformation of nickel-base superalloy, Mater. Des. 94 (2016) 195-206.

[72] F. Vollertsen, Categories of size effects, Prod. Eng. 2 (2008) 377-383.

[73] J.R. Greer, J.T.M. De Hosson, Plasticity in small-sized metallic systems: Intrinsic versus extrinsic size effect, Prog. Mater Sci. 56(6) (2011) 654-724.

[74] X. Zhou, X. Li, K. Lu, Size dependence of grain boundary migration in metals under mechanical loading, Phys. Rev. Lett. 122(12) (2019) 126101.

[75] H. Wang, P. Zhang, C. Wang, Q. Zhu, G. Chen, Investigation of the size effect on flow stress and deformation mechanism in Cu-Zn thin sheets, Mater. Sci. Eng., A 922 (2025) 147622.

[76] A. Dhal, S.K. Panigrahi, M.S. Shunmugam, Achieving excellent microformability in aluminum by engineering a unique ultrafine-grained microstructure, Sci. Rep. 9(1) (2019) 10683.

[77] G.Z. Voyiadjis, M. Yaghoobi, Size effects in plasticity: from macro to nano, Academic Press2019.

[78] W. Gao, J. Lu, J. Zhou, L.e. Liu, J. Wang, Y. Zhang, Z. Zhang, Effect of grain size on deformation and fracture of Inconel718: An in-situ SEM-EBSD-DIC investigation, Mater. Sci. Eng., A 861 (2022) 144361.

[79] W. Li, H. Li, M. Fu, Interactive effect of stress state and grain size on fracture behaviours of copper in micro-scaled plastic deformation, Int. J. Plast. 114 (2019) 126-143.

[80] J. Miao, T.M. Pollock, J.W. Jones, Microstructural extremes and the transition from fatigue crack initiation to small crack growth in a polycrystalline nickel-base superalloy, Acta Mater. 60(6-7) (2012) 2840-2854.

[81] J.Q. Ran, M.W. Fu, A hybrid model for analysis of ductile fracture in micro-scaled plastic deformation of multiphase alloys, International Journal of Plasticity 61 (2014) 1-16.

[82] F. Roters, P. Eisenlohr, L. Hantcherli, D.D. Tjahjanto, T.R. Bieler, D. Raabe, Overview of constitutive laws, kinematics, homogenization and multiscale methods in crystal plasticity finite-element modeling: Theory, experiments, applications, Acta Mater. 58(4) (2010) 1152-1211.

[83] T. Al-Samman, X. Li, S.G. Chowdhury, Orientation dependent slip and twinning during compression and tension of strongly textured magnesium AZ31 alloy, Mater. Sci. Eng., A 527(15) (2010) 3450-3463.

[84] C. Zambaldi, C. Zehnder, D. Raabe, Orientation dependent deformation by slip and twinning in magnesium during single crystal indentation, Acta Mater. 91 (2015) 267-288.

[85] C.D. Breach, F.W. Wulff, A brief review of selected aspects of the materials science of ball bonding, Microelectron. Reliab. 50(1) (2010) 1-20.

[86] H. Li, X. Sun, H. Yang, A three-dimensional cellular automata-crystal plasticity finite element model for predicting the multiscale interaction among heterogeneous deformation, DRX microstructural evolution and mechanical responses in titanium alloys, Int. J. Plast. 87 (2016) 154-180.

[87] J.R. Rice, Inelastic constitutive relations for solids: An internal-variable theory and its application to metal plasticity, J. Mech. Phys. Solids 19(6) (1971) 433-455.

[88] R. Hill, J.R. Rice, Constitutive analysis of elastic-plastic crystals at arbitrary strain, J. Mech. Phys. Solids 20(6) (1972) 401-413.

[89] F.J. Harewood, P.E. McHugh, Comparison of the implicit and explicit finite element methods using crystal plasticity, Comput. Mater. Sci 39(2) (2007) 481-494.

[90] X. Ma, H. Zhai, L. Song, W. Zhang, Y. Hu, Q. Zhang, In situ study on plastic deformation mechanism of Al0.3CoCrFeNi high-entropy alloys with different microstructures, Mater. Sci. Eng., A 857 (2022) 144134.

[91] N. Bian, F. Li, H. Du, W. Niu, Z. Chen, Effect mechanism of texture orientation on mechanical properties and Hall-Petch relationship of CVCDE AZ31 magnesium alloy via crystal plastic finite element method (CPFEM), J. Alloys Compd. 923 (2022) 166248.

[92] W. Li, L. Wang, B. Zhou, C. Liu, X. Zeng, Grain-scale deformation in a Mg−0.8 wt% Y alloy using crystal plasticity finite element method, Journal of Materials Science & Technology 35(10) (2019) 2200-2206.

[93] A. Asgharzadeh, S.A. Nazari Tiji, T. Park, F. Pourboghrat, Prediction of softening kinetics and recrystallization texture in non-isothermally annealed bulged tubes using CPFEM and CA models, Mater. Sci. Eng., A 832 (2022) 142308.

[94] M. Jiang, Z. Fan, S. Kruch, B. Devincre, Grain size effect of FCC polycrystal: A new CPFEM approach based on surface geometrically necessary dislocations, Int. J. Plast. 150 (2022) 103181.

[95] U.B. Asim, M.A. Siddiq, M.E. Kartal, A CPFEM based study to understand the void growth in high strength dual-phase titanium alloy (Ti-10V-2Fe-3Al), Int. J. Plast. 122 (2019) 188-211.

[96] D. Zhang, H. Li, X. Guo, Y. Yang, X. Yang, Z. Feng, An insight into size effect on fracture behavior of Inconel 718 cross-scaled foils, Int. J. Plast. 153 (2022) 103274.

[97] J. Zhang, X. Li, D. Xu, C. Teng, H. Wang, L. Yang, H. Ju, H. Xu, Z. Meng, Y. Ma, Y. Wang, R. Yang, Phase field simulation of the stress-induced α microstructure in Ti–6Al–4 V alloy and its CPFEM properties evaluation, Journal of Materials Science & Technology 90 (2021) 168-182.

[98] C.M.A. Iftikhar, A. Brahme, K. Inal, A.S. Khan, An evolution of subsequent yield loci under proportional and non-proportional loading path of 'as-received' extruded AZ31 magnesium alloy: Experiments and CPFEM modeling, Int. J. Plast. 151 (2022) 103216.

[99] W. Muhammad, A.P. Brahme, U. Ali, J. Hirsch, O. Engler, H. Aretz, J. Kang, R.K. Mishra, K. Inal, Bendability enhancement of an age-hardenable aluminum alloy: Part II — multiscale numerical modeling of shear banding and fracture, Mater. Sci. Eng., A 754 (2019) 161-177.

[100] R. Zhang, Z. Xu, L. Peng, X. Lai, M.W. Fu, Modelling of ultra-thin steel sheet in two-stage tensile deformation considering strain path change and grain size effect and application in multi-stage microforming, Int. J. Mach. Tools Manuf. 164 (2021) 103713.

[101] F. Adzima, T. Balan, P.Y. Manach, Springback prediction for a mechanical micro connector using CPFEM based numerical simulations, Int. J. Mater. Form. 13(4) (2020) 649-659.

[102] J.A. Grogan, S.B. Leen, P.E. McHugh, Influence of statistical size effects on the plastic deformation of coronary stents, J. Mech. Behav. Biomed. Mater. 20 (2013) 61-76.

[103] S. Wang, W. Zhuang, J. Cao, J. Lin, An investigation of springback scatter in forming ultra-thin metal-sheet channel parts using crystal plasticity FE analysis, Int. J. Adv. Manuf. 47(9) (2010) 845-852.

[104] J. Singh, M.-S. Kim, S.-H. Choi, The effect of initial texture on micromechanical deformation behaviors in Mg alloys under a mini-V-bending test, Int. J. Plast. 117 (2019) 33-57.

[105] H. Zhang, X. Dong, Physically based crystal plasticity FEM including geometrically necessary dislocations: Numerical implementation and applications in micro-forming, Comput. Mater. Sci 110 (2015) 308-320.

[106] J. Zhao, Z. Jiang, Z. Wang, S. Sang, L.A. Dobrzański, M. Yang, X. Ma, Y. Wang, An analysis of micro deep drawing of ferritic stainless steel 430 using crystal plasticity finite element method, J. Mater. Res. Technol. 20 (2022) 2247-2261.

[107] W. Zhang, Y. Wang, X. Li, S. Hao, Y. Chi, X. Ma, L. Chen, M. Jin, The effect of phase distribution of constituent-fiber structure on the deformation heterogeneity of TRIP-assisted lean duplex stainless steel, Mater. Sci. Eng., A 878 (2023) 145216.

[108] H. Zhao, X. Ma, Z. Wang, Z. Jiang, C. Zhou, J. Zhao, Surface roughness evolution and heterogeneous plastic deformation of austenitic stainless steel during micro deep drawing: Modeling and experiment, Int. J. Plast. 176 (2024) 103964.

[109] Y. Yang, C. Xu, L. Fan, Inhomogeneous Deformation and Texture Evolution of 30SiMn2MoVA Steel Gun Barrel Processed by Radial Forging Based on Cross-scale Crystal Plasticity Finite Element Method, Mater. Res. 25 (2022) e20220115.

[110] Y. Shao, T. Tang, D. Li, W. Tang, Y. Peng, Crystal plasticity finite element modelling of the extrusion texture of a magnesium alloy, Modell. Simul. Mater. Sci. Eng. 23(5) (2015) 055011.

[111] J. Cao, W. Zhuang, S. Wang, J. Lin, Development of a VGRAIN system for CPFE analysis in micro-forming applications, Int. J. Adv. Manuf. 47(9) (2010) 981-991.

[112] Z.Y. Feng, H. Li, D. Zhang, X.X. Guo, Y.Q. Chen, M.W. Fu, Multi-aspect size effect transition from micro to macroscale: Modelling and experiment, Int. J. Plast. 156 (2022) 103364.

[113] C. Lu, G.Y. Deng, A.K. Tieu, L.H. Su, H.T. Zhu, X.H. Liu, Crystal plasticity modeling of texture evolution and heterogeneity in equal channel angular pressing of aluminum single crystal, Acta Mater. 59(9) (2011) 3581-3592.

[114] G.Y. Deng, C. Lu, L.H. Su, X.H. Liu, A.K. Tieu, Modeling texture evolution during ECAP of copper single crystal by crystal plasticity FEM, Mater. Sci. Eng., A 534 (2012) 68-74.

[115] M. Liu, N. Shoichi, K. Toshihiko, T.K. Anh, K. and Zhou, Three-dimensional quantification of texture heterogeneity in single-crystal aluminium subjected to equal channel angular pressing, Philos. Mag. 97(11) (2017) 799-819.

[116] S. Chen, X. Liu, L. Liu, Effects of grain size and heterogeneity on the mechanical behavior of foil rolling, Int. J. Mech. Sci. 100 (2015) 226-236.

[117] Y. Zhang, Z. Hu, L. Guo, Study on a New Forming Method—Thread Rolling by Crystal Plasticity Finite Element Simulation, Metals 11(3) (2021) 503.

[118] K.-H. Jung, D.-K. Kim, Y.-T. Im, Y.-S. Lee, Crystal plasticity finite element analysis of texture evolution during rolling of fcc polycrystalline metal, Materials Transactions 54(5) (2013) 769-775.

[119] J.-Y. Zheng, J. Wang, M.W. Fu, Experimental and numerical study of the size effect on compound Meso/Microforming behaviors and performances for making bulk parts by directly using sheet metals, J. Manuf. Processes 66 (2021) 506-520.

[120] İ. Özdemir, Grain statistics induced size effect in the expansion of metallic micro rings, Int. J. Mech. Sci. 87 (2014) 52-59.

[121] M.W. Fu, W.L. Chan, Micro-scaled Products Development via Microforming, Springer2014.

[122] W.T. Li, M.W. Fu, J.L. Wang, B. Meng, Grain Size Effect on Multi-Stage Micro Deep Drawing of Micro Cup with Domed Bottom, Int. J. Precis. Eng. Manuf. 17(6) (2016) 765-773.

[123] R.J. Asaro, A. Needleman, Overview no. 42 Texture development and strain hardening in rate dependent polycrystals, Acta Metall. 33(6) (1985) 923-953.

[124] D. Peirce, R.J. Asaro, A. Needleman, An analysis of nonuniform and localized deformation in ductile single crystals, Acta Metall. 30(6) (1982) 1087-1119.

[125] Y. Huang, A user-material subroutine incroporating single crystal plasticity in the ABAQUS finite element program, Harvard Univ. Cambridge1991.

[126] W.L. Chan, M.W. Fu, Experimental studies of plastic deformation behaviors in microheading process, J. Mater. Process. Technol. 212(7) (2012) 1501-1512.

[127] T. Bretheau, D. Caldemaison, Test of mechanical interaction models between polycrystal grains by means of local strain measurements, Deformation of Polycrystals: Mechanisms and Microstructures. 2 nd Riso Int. Symposium on Metallurgy and Materials Science, 1981, pp. 157-161.

[128] F. Vollertsen, Z. Hu, H.S. Niehoff, C. Theiler, State of the art in micro forming and investigations into micro deep drawing, J. Mater. Process. Technol. 151(1) (2004) 70-79.

[129] M. Elices, G.V. Guinea, J. Gómez, J. Planas, The cohesive zone model: advantages, limitations and challenges, Eng. Fract. Mech. 69(2) (2002) 137-163.

[130] S.R. Kalidindi, Incorporation of deformation twinning in crystal plasticity models, J. Mech. Phys. Solids 46(2) (1998) 267-290.

[131] W. Cai, C. Sun, C. Wang, L. Qian, Y. Li, M.W. Fu, Modelling of the intergranular fracture of TWIP steels working at high temperature by using CZM–CPFE method, Int. J. Plast. 156 (2022) 103366.

[132] A.A. Salem, S.R. Kalidindi, S.L. Semiatin, Strain hardening due to deformation twinning in α-titanium: Constitutive relations and crystal-plasticity modeling, Acta Mater. 53(12) (2005) 3495-3502.

[133] S. R. Kalidindi, Modeling anisotropic strain hardening and deformation textures in low stacking fault energy fcc metals, Int. J. Plast. 17(6) (2001) 837-860.

[134] M. Lu, F. Wang, X. Zeng, W. Chen, J. Zhang, Cohesive zone modeling for crack propagation in polycrystalline NiTi alloys using molecular dynamics, Theor. Appl. Fract. Mech. 105 (2020) 102402.

[135] N. Jia, F. Roters, P. Eisenlohr, C. Kords, D. Raabe, Non-crystallographic shear banding in crystal plasticity FEM simulations: Example of texture evolution in α-brass, Acta Mater. 60(3) (2012) 1099-1115.

[136] R. Chiarodo, I. Spain, P. Bolsaitis, Elastic constants and their pressure derivatives of α-brass single crystals, J. Phys. Chem. Solids 35(6) (1974) 762-764.

[137] K. Li, B. Yu, R.D.K. Misra, G. Han, Y.T. Tsai, C.W. Shao, C.J. Shang, J.R. Yang, Z.F. Zhang, Strain rate dependence on the evolution of microstructure and

deformation mechanism during nanoscale deformation in low carbon-high Mn TWIP steel, Mater. Sci. Eng., A 742 (2019) 116-123.

[138] Y.J. Wang, C.Q. Ru, Determination of two key parameters of a cohesive zone model for pipeline steels based on uniaxial stress-strain curve, Eng. Fract. Mech. 163 (2016) 55-65.

[139] W. Koster, W. Rauscher, Relations between the modulus of elasticity of binary alloys and their structure, 1951.

[140] R. Kumar, A. Misra, Some basic aspects of electromagnetic radiation emission during plastic deformation and crack propagation in Cu–Zn alloys, Mater. Sci. Eng., A 454-455 (2007) 203-210.

[141] H. Yan, X. Zhao, N. Jia, Y. Zheng, T. He, Influence of Shear Banding on the Formation of Brass-type Textures in Polycrystalline fcc Metals with Low Stacking Fault Energy, Journal of Materials Science & Technology 30(4) (2014) 408-416.

[142] L. Li, W. Liu, F. Qi, D. Wu, Z. Zhang, Effects of deformation twins on microstructure evolution, mechanical properties and corrosion behaviors in magnesium alloys - A review, J. Magnesium Alloys 10(9) (2022) 2334-2353.

[143] K.G. Praveen, S. Kurra, Analysis of deformation behavior in various incremental tube forming processes, Mater. Manuf. Processes 36(14) (2021) 1631-1641.

[144] B.-B. Jia, G. Chen, W.-W. Wang, Y. Shen, Y. Gu, Deformation characteristics and forming force limits of multi-point forming with individually controlled force–displacement, Int. J. Adv. Manuf. 123(5) (2022) 1565-1576.

[145] Z. Zhao, Y. Li, C. Liu, Z. Chen, J. Chen, L. Wang, A subsequent-machining-deformation prediction method based on the latent field estimation using deformation force, J. Manuf. Syst. 63 (2022) 224-237.

[146] W.L. Phillips, R.W. Armstrong, The strain dependence of the flow stress-grain size relation for 70:30 brass, Metallurgical Transactions 3(10) (1972) 2571-2577.

[147] D. Li, L. Wang, W. Li, Effects of grain size from micro scale to nanoscales on the yield strain of brass under compressive and tensile stresses using a Kelvin probing

technique, Mater. Sci. Eng., A 384(1-2) (2004) 355-360.

[148] J. Hönnige, C.E. Seow, S. Ganguly, X. Xu, S. Cabeza, H. Coules, S. Williams, Study of residual stress and microstructural evolution in as-deposited and inter-pass rolled wire plus arc additively manufactured Inconel 718 alloy after ageing treatment, Mater. Sci. Eng., A 801 (2021) 140368.

[149] W. Zhou, J. Yu, X. Lu, J. Lin, T.A. Dean, A comparative study on deformation mechanisms, microstructures and mechanical properties of wide thin-ribbed sections formed by sideways and forward extrusion, Int. J. Mach. Tools Manuf. 168 (2021) 103771.

[150] S.C. Shrivastava, J.J. Jonas, G. Canova, Equivalent strain in large deformation torsion testing : Theoretical and practical considerations, J. Mech. Phys. Solids 30(1) (1982) 75-90.

[151] H. Zhou, H. Cui, Q.H. Qin, Influence of ultrasonic vibration on the plasticity of metals during compression process, J. Mater. Process. Technol. 251 (2018) 146-159.

[152] K. Karami, A. Blok, L. Weber, S.M. Ahmadi, R. Petrov, K. Nikolic, E.V. Borisov, S. Leeflang, C. Ayas, A.A. Zadpoor, M. Mehdipour, E. Reinton, V.A. Popovich, Continuous and pulsed selective laser melting of Ti6Al4V lattice structures: Effect of post-processing on microstructural anisotropy and fatigue behaviour, Addit. Manuf. 36 (2020) 101433.

[153] J.H. Deng, M.W. Fu, W.L. Chan, Size effect on material surface deformation behavior in micro-forming process, Mater. Sci. Eng., A 528(13) (2011) 4799-4806.

[154] M.A. Ansari, A. Samanta, R.A. Behnagh, H. Ding, An efficient coupled Eulerian-Lagrangian finite element model for friction stir processing, Int. J. Adv. Manuf. 101(5) (2019) 1495-1508.

[155] P. Wang, C. Lian, C. Yue, X. Wu, J. Zhang, K. Zhang, Z. Yue, Experimental and numerical study of tire debris impact on fuel tank cover based on coupled Eulerian-Lagrangian method, Int. J. Impact Eng. 157 (2021) 103968.

[156] C. Liu, W. Xu, T. Niu, Y. Chen, Roughness evolution of constrained surface based on crystal plasticity finite element model and coupled Eulerian-Lagrangian method, Comput. Mater. Sci 201 (2022) 110900.

[157] H.W. Swift, Plastic instability under plane stress, J. Mech. Phys. Solids 1(1) (1952) 1-18.

[158] V. Kumar Reddy Sirigiri, V. Yadav Gudiga, U. Shankar Gattu, G. Suneesh, K. Mohan Buddaraju, A review on Johnson Cook material model, Mater. Today:. Proc. 62 (2022) 3450-3456.

[159] F. Al-Badour, N. Merah, A. Shuaib, A. Bazoune, Coupled Eulerian Lagrangian finite element modeling of friction stir welding processes, J. Mater. Process. Technol. 213(8) (2013) 1433-1439.

[160] M. Türkan, Ö. Karakaş, Numerical modeling of defect formation in friction stir welding, Mater. Today Commun. 31 (2022) 103539.

[161] F. Ducobu, E. Rivière-Lorphèvre, E. Filippi, Application of the Coupled Eulerian-Lagrangian (CEL) method to the modeling of orthogonal cutting, European Journal of Mechanics A-solids 59 (2016) 58-66.

[162] D. Ambrosio, A. Tongne, V. Wagner, G. Dessein, O. Cahuc, A new damage evolution criterion for the coupled Eulerian-Lagrangian approach: Application to three-dimensional numerical simulation of segmented chip formation mechanisms in orthogonal cutting, J. Manuf. Processes 73 (2022) 149-163.

[163] X. Song, K.L. Ng, J.M.-K. Chea, W. Sun, A.W.-Y. Tan, W. Zhai, F. Li, I. Marinescu, E. Liu, Coupled Eulerian-Lagrangian (CEL) simulation of multiple particle impact during Metal Cold Spray process for coating porosity prediction, Surf. Coat. Technol. 385 (2020) 125433.

[164] Y. Gao, J.H. Ko, H.P. Lee, 3D coupled Eulerian-Lagrangian finite element analysis of end milling, Int. J. Adv. Manuf. 98 (2018) 849-857.

[165] K.S. Al-Athel, M.S. Gadala, Eulerian volume of solid (VOS) approach in solid mechanics and metal forming, Computer Methods in Applied Mechanics and Engineering 200(25) (2011) 2145-2159.

[166] Z.-H. Hah, S.-K. Youn, Eulerian analysis of bulk metal forming processes based on spline-based meshfree method, Finite Elem. Anal. Des. 106 (2015) 1-15.

[167] K. Liu, L. Lang, W. Zhang, M. Marai, B. Liu, Coupled Eulerian–Lagrangian

simulation of granular medium sheet forming process and experimental ınvestigation at elevated temperature, Int. J. Adv. Manuf. 88(9) (2017) 2871-2882.

[168] P. Asadi, M. Akbari, Numerical modeling and experimental investigation of brass wire forming by friction stir back extrusion, Int. J. Adv. Manuf. 116(9) (2021) 3231-3245.

[169] A. Kumar, C.P. Gandhi, Y. Zhou, R. Kumar, J. Xiang, Latest developments in gear defect diagnosis and prognosis: A review, Measurement 158 (2020) 107735.

[170] K. Gupta, R.F. Laubscher, J.P. Davim, N.K. Jain, Recent developments in sustainable manufacturing of gears: a review, J. Cleaner Prod. 112 (2016) 3320-3330.

[171] S. Xiong, X. Zhang, D. Liang, Molecular dynamics simulation of friction coefficient of Fe-Al during lubrication, Comput. Mater. Sci 217 (2023) 111895.

[172] S.R. Kalidindi, C.A. Bronkhorst, L. Anand, Crystallographic texture evolution in bulk deformation processing of FCC metals, J. Mech. Phys. Solids 40(3) (1992) 537-569.

[173] L. Tabourot, M. Fivel, E. Rauch, Generalised constitutive laws for f.c.c. single crystals, Mater. Sci. Eng., A 234-236 (1997) 639-642.

[174] A. Gargallo-Peiró, X. Roca, J. Peraire, J. Sarrate, Distortion and quality measures for validating and generating high-order tetrahedral meshes, Engineering with Computers 31(3) (2015) 423-437.

[175] J. Cheng, A. Shahba, S. Ghosh, Stabilized tetrahedral elements for crystal plasticity finite element analysis overcoming volumetric locking, Comput. Mech. 57(5) (2016) 733-753.

[176] C.-H. Lin, C. Hung, T.-Y. Hsu, Investigations of granular material behaviors using coupled Eulerian-Lagrangian technique: From granular collapse to fluid-structure interaction, Comput. Geotech. 121 (2020) 103485.

[177] M.S. Zakaria, T.L. Ginta, A.I. Azmi, A Coupled Eulerian Lagrangian (CEL) Model in Prediction Tool Temperature, in: M.S. Bahari, A. Harun, Z. Zainal Abidin, R. Hamidon, S. Zakaria (Eds.) Intelligent Manufacturing and Mechatronics, Springer Singapore, Singapore, 2021, pp. 1237-1244.

[178] P. Sridhar, J.M. Rodríguez Prieto, K.M. de Payrebrune, Discretization approaches to model orthogonal cutting with Lagrangian, Arbitrary Lagrangian Eulerian, Particle Finite Element method and Smooth Particle Hydrodynamics formulations, Procedia CIRP 93 (2020) 1496-1501.

[179] D. Gomez-Marquez, E. Ledesma-Orozco, R. Hino, E. Aguilera-Gomez, G. Korpała, U. Prahl, Numerical study on the hot compression test for bulk metal forming application, SN Appl. Sci. 4(8) (2022) 220.

[180] G. Qiu, S. Henke, J. Grabe, Application of a Coupled Eulerian–Lagrangian approach on geomechanical problems involving large deformations, Comput. Geotech. 38(1) (2011) 30-39.

[181] S.M. Anas, M. Shariq, M. Alam, M. Umair, Evaluation of critical damage location of contact blast on conventionally reinforced one-way square concrete slab applying CEL-FEM blast modeling technique, International Journal of Protective Structures 13(4) (2022) 672-715.

[182] M. Wotzlaw, R. Daryaei, D. Aubram, F. Rackwitz, Ghost material in geotechnical applications of the CEL method, Comput. Geotech. 167 (2024) 106082.

[183] A. Awasthi, K.K. Saxena, V. Arun, Sustainable and smart metal forming manufacturing process, Mater. Today:. Proc. 44 (2021) 2069-2079.

[184] A.E. Tekkaya, P.O. Bouchard, S. Bruschi, C.C. Tasan, Damage in metal forming, CIRP Ann. 69(2) (2020) 600-623.

[185] D.-F. Li, C.-G. Bai, Z.-Q. Zhang, J. Zhao, Shear banding and serrated flow behaviors of high toughness Zr61Ti2Cu25Al12 bulk metallic glass under bending, Mater. Sci. Eng., A 844 (2022) 143172.

[186] C. Körner, M. Markl, J.A. Koepf, Modeling and Simulation of Microstructure Evolution for Additive Manufacturing of Metals: A Critical Review, Metallurgical and Materials Transactions A 51(10) (2020) 4970-4983.

[187] M. Merklein, J. Koch, S. Opel, T. Schneider, Fundamental investigations on the material flow at combined sheet and bulk metal forming processes, CIRP Ann. 60(1) (2011) 283-286.

[188] M. Löffler, R. Schulte, D. Freiburg, D. Biermann, D. Stangier, W. Tillmann, M. Merklein, Control of the material flow in sheet-bulk metal forming using modifications of the tool surface, Int. J. Mater. Form. 12(1) (2019) 17-26.

[189] G.C. Wang, W. Zheng, T. Wu, H. Jiang, G.Q. Zhao, D.B. Wei, Z.Y. Jiang, A multi-region model for numerical simulation of micro bulk forming, J. Mater. Process. Technol. 212(3) (2012) 678-684.

[190] H. Liu, H. Liu, C. Zhu, Z. Sun, H. Bai, Study on contact fatigue of a wind turbine gear pair considering surface roughness, Friction 8(3) (2020) 553-567.

[191] E. Bergstedt, J. Lin, U. Olofsson, Influence of gear surface roughness on the pitting and micropitting life, Proceedings of the Institution of Mechanical Engineers, Part C: Journal of Mechanical Engineering Science 234(24) (2020) 4953-4961.

[192] L. Peng, Z. Xu, Z. Gao, M.W. Fu, A constitutive model for metal plastic deformation at micro/meso scale with consideration of grain orientation and its evolution, Int. J. Mech. Sci. 138-139 (2018) 74-85.

[193] M. Zhao, H. Wu, J. Lu, G. Sun, L. Du, Effect of grain size on mechanical property and corrosion behavior of a metastable austenitic stainless steel, Mater. Charact. 194 (2022) 112360.

[194] Y. Liu, S.C.V. Lim, C. Ding, A. Huang, M. Weyland, Unravelling the competitive effect of microstructural features on the fracture toughness and tensile properties of near beta titanium alloys, Journal of Materials Science & Technology 97 (2022) 101-112.

[195] I.T. Tandogan, M. Budnitzki, S. Sandfeld, A multi-physics model for the evolution of grain microstructure, Int. J. Plast. 185 (2025) 104201.